5-6-2016

Evaluation of Soft Material Microstructure through High-frequency Ultrasound

Jeremy D. Stromer
stromerjd@gmail.com

Evaluation of Soft Material Microstructure through High-frequency Ultrasound

Jeremy David Stromer, Ph.D.

University of Connecticut, 2016

Ultrasonic measurement allows for nondestructive testing and inspection of the internal structure of tissues and materials. Ultrasound has a number of advantages over other commonly used nondestructive methods. It is safe, relatively inexpensive, and is the most commonly used health diagnostic imaging method. Nevertheless, traditional ultrasound does have disadvantages. Standard methods detect the presence of flaws and inclusions from amplitude and time-of-flight information. However, these techniques provide little insight into the actual material characteristics of the sample. Available techniques use a limited, low range of frequencies. The measurements also need to be interpreted by trained technicians and can vary among ultrasound systems. The field of Quantitative Ultrasound was developed to address these shortcomings by looking deeper into the characteristics of the received signals.

The objective of this dissertation is to understand the scattering behavior of high-frequency signals for relatively small specimens and relate that to the microstructure of materials. In particular, a recently developed quantitative parameter which was found to be responsive to tissue microstructure, peak density, is investigated. Due to the infancy of using peak density, the physical characteristics that affect it are not fully understood.

The procedures and algorithms developed for characterizing materials based upon peak density are discussed. The results of experimental studies using tissue-like phantom materials containing internal inclusions are presented. Two-dimensional images created using peak density measurements were found to locate the inclusions better than standard amplitude based images.

Jeremy David Stromer– University of Connecticut, 2016

It was found that peak density was highly reliant on the specific signal processing methods used. The process is then optimized and standardized to generate high quality measurements. The response to microstructure is investigated by studying tissue-mimicking phantoms containing glass scatters of various sizes and number densities. Finite element simulations of ultrasound waves traveling through tissue phantoms containing glass microspheres are developed, and the results are compared against experiment. From the simulations and experiments it was established that peak density is most responsive to larger numbers of scatterers present in the material and is more reliable for scatterers with diameters near the wavelength. The peak density was also found to be more sensitive than amplitude-based techniques.

Evaluation of Soft Material Microstructure through High-frequency Ultrasound

Jeremy David Stromer

B.S., University of Nebraska at Kearney, 2011
M.S., University of Connecticut, 2015

A Dissertation

Submitted in Partial Fulfillment of the
Requirements for the Degree of
Doctor of Philosophy
at the
University of Connecticut

2016

APPROVAL PAGE

Doctor of Philosophy Dissertation

Evaluation of Soft Material Microstructure Through High-frequency Ultrasound

Presented by

Jeremy Stromer

Major Advisor _____

Leila Ladani

Associate Advisor _____

Bi Zhang

Associate Advisor _____

Jiong Tang

Associate Advisor _____

Nejat Olgac

Associate Advisor _____

Quing Zhu

University of Connecticut
2016

Acknowledgements

I would like to express my gratitude to my adviser, Dr. Leila Ladani, for allowing me the opportunity to work on a project that allowed me to couple my interests of physics and engineering.

I would also thank to thank my committee members Dr. Nejat Olgac, Dr. Bi Zhang, Dr. Quing Zhu, and Dr. Jiong Tang.

I appreciate the opportunity to participate in the National Science Foundation's GK-12 Fellowship Program. Having fun with the high school students was always a welcome respite from research. Particularly, I would like to thank Aida Ghiaei for everything she did as part of this program.

My lab mates were awesome, and I am glad to have had the opportunity to work with each of them.

To my parents Arnold and Connie Stromer, thank you for the love and care you put into raising me.

Most of all, I would like to thank my wife, Bobbi. Everything is much better with you by my side.

List of frequently used symbols

a	Radius
c	Sound speed
f	Frequency
$h_l^{(2)}$	Spherical Hankel function of the second kind
j_l	Spherical Bessel function of the first kind
k	Wave number
λ	Wavelength
η_l	Associated phase shift due to boundary conditions
n_l	Spherical Bessel function of the second kind
σ_s	Scattering cross-section
P_l	Legendre polynomial
ρ	Density
p	Pressure
p_i	Incident pressure
p_s	Scattered pressure
t	Time
$\boldsymbol{u}$	Displacement field
ν	Poisson's ratio

Contents

List of Figures

List of Tables

Chapter 1.
Introduction

1.1 Motivation

In the United States in 2014, there were an estimated 235,000 new cases and approximately 40,000 deaths in the United States owing to breast cancer. Due to these continuingly large numbers of people affected, breast cancer remains a significant cause of concern in public health [1,2]. Although no considerable improvement has been found for breast-conserving therapy (BCT) compared to the more traditional mastectomy, the less destructive method of BCT has become the preferred treatment due to both the emotional and esthetic benefits of saving breast tissue. Contrary to a mastectomy, BCT is comprised of a lumpectomy and radiation treatments. During a lumpectomy the tumor is removed along with a small margin of surrounding healthy tissue. By minimizing the amount of excised tissue, the patient can suffer less breast disfigurement [3,4]. The excised tumor and margin is then sent to a pathologist for further microscopic analysis. Complications and local reoccurrence can arise if cancerous cells are found to be present in the margin, and in which case additional surgery is recommended. It is therefore advantageous to improve the ability to obtain a negative, or cancer-free, margin at the time of the initial surgery [3-8].

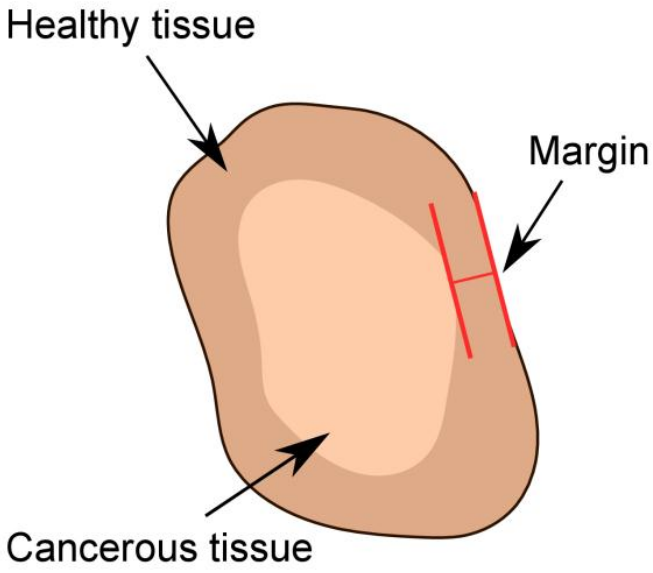

Figure 1. Illustration of excised tumor from BCT. The cancerous tissue is removed with a small portion of healthy tissue to ensure the entirety of the tumor is removed.

The methods presently used for margin detection include pre-operative and intraoperative techniques. Conventional imaging systems such as mammography, traditional B-scan ultrasound, and MRI have been used prior to surgery, but the size of tumors is often inaccurately assessed [9,10]. The most common intraoperative method used currently is frozen section analysis wherein the excised tissue is cut, cryostatically frozen and examined by a pathologist on site. While this method helps reduce the chance of re-excision it is labor intensive and requires a trained pathologist to be present [11,12]. Another common technique which also has the requirement of having a trained pathologist present is touch preparation cytology. In addition it is not capable of testing a large amount of the removed tissue [12].

Other intraoperative methods have been proposed to improve upon the quality of margin detection while alleviating the need of a trained pathologist. A wide range of research is being conducted in both the public and private sectors and spans multiple disciplines. A recent commercial attempt at a margin detection device called the MarginProbe^{TM}. This device manufactured by Dune Medical Devices evaluates the margin status by evaluating its electromagnetic properties [12]. A clinical study found that slightly fewer re-excisions were necessary when the MarginProbe^{TM} was used during surgery. It has been noted that the difference was not statistically significant and may have been caused by a larger initial amount of tissue being removed when the device was used [3,14].

A considerable amount of work has also been done investigating the use of optical imaging techniques including diffuse reflectance spectroscopy, optical coherence tomography, and Raman spectroscopy [8,15,16]. Optical methods require contrast agents for imaging and must contend with tissue-light interactions [12]. A popular method for materials characterization, X-ray diffraction has also been used to evaluate margins. This technique has been used to create images similarly to conventional CT scanners but has been downsized to a smaller scale using so-called micro-CT [17]. Micro-CT scans tend to be lengthy taking several minutes for each [12].

This need for improved methods for surgical margin detection prompted the work found in this dissertation. For the reasons outlined in the following section, ultrasound was chosen as a means for nondestructive evaluation of soft materials. It is the hope of the author that the work presented here can serve as a basis for further development of the ultrasonic methods given with the eventual goal of improved tissue characterization.

1.2 Ultrasonic methods

Ultrasonic measurement has become ubiquitous throughout the field of nondestructive evaluation and has found use in industrial, structural and medical settings. Ultrasound allows the user to study materials through individual analytical measurements and can even allow the user to actually visualize the internal structure. It is largely due to this functionality that ultrasound has seen such widespread use in flaw detection and diagnostic medicine. Ultrasound has a number of advantages over other measurement techniques. Ultrasound machines are relatively inexpensive. Conventional clinical systems cost <$50,000, while the price of MRI machines are >$1 million. The systems do not require a large amount of space and are easily portable. As opposed to most other nondestructive methods commonly used, ultrasound has one of the greatest penetration depths and may allow for detection well below the sample surface [18,19]. Even miniature transducers are available and allow for small-scale measurements; transducers have been attached to catheters for use in intravascular imaging and endoscopes for gastrointestinal [20,21]. Ultrasound has also shown to be relatively safe, and is absent of the ionizing radiation present in other imaging methods [18,22,23].

1.2.1 Standard methods

The most commonly performed ultrasound measurements rely on the amplitude and time of flight information of the propagated sound pulse [1,12,20,23,24]. Figure 2 demonstrates the most frequently used method in the pulse-echo configuration. This procedure is used in thickness gauging as well flaw detection. It also forms the basis for the majority of imaging applications. In this setup, the transducer is placed on the material and generates an ultrasonic pulse which

travels through the material. When the wave hits an obstruction, the wave is reflected back and is received by the transducer. This in turn may generate a signal on a display. In this example, the wave travels through the sample and hits two objects- a flaw and the bottom edge. With the foreknowledge of the materials sound velocity, often easily referenced or determined from other mechanical properties, it is possible to work backward using the arrival time of the pulse. In this case, our display registers two pulses with one arriving at 30 μs and the other at 40 μs. Using $v = d/t$, it is deduced that one reflection occurred 3 cm deep and the other at 4 cm. It is also useful to use the amplitude information as well to infer information about the reflectors. The first pulse was relatively weak denoting a small obstruction such as a flaw, and the second pulse suggested a strong reflector like the back edge of the sample. This procedure allows the operator to discover internal structure and their axial location. It also serves as the basis for conventional ultrasound imaging. A standard image, such as one conducted in hospitals, is essentially this type of measurement carried out at different lateral locations. By combining each individual scan an image can be formed.

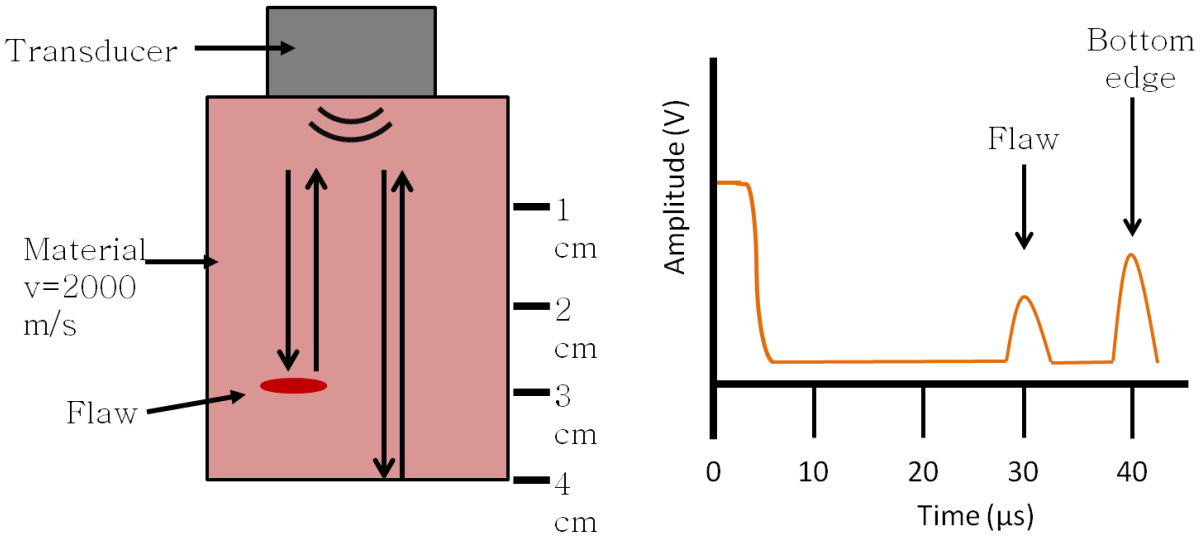

Figure 2. Diagram outlining the standard pulse-echo measurement procedure.

Another common method based off of the signal amplitude and time of flight is shown in Figure 3. This technique makes use of two transducers with one created the sound and the other receiving it. The transducers are passed laterally across the transducer, and the strength of the received pulse is measured. By locating points where little sound travels it is possible to detect flaws. In this example, measurements are being carried out on a multi-layer composite. When the signal strength is low, it may suggest that a delamination exists between the composite layers. This specific procedure is more widespread in industry. As a note, it is also possible to measure thickness in a manner similar to the previous example using this configuration.

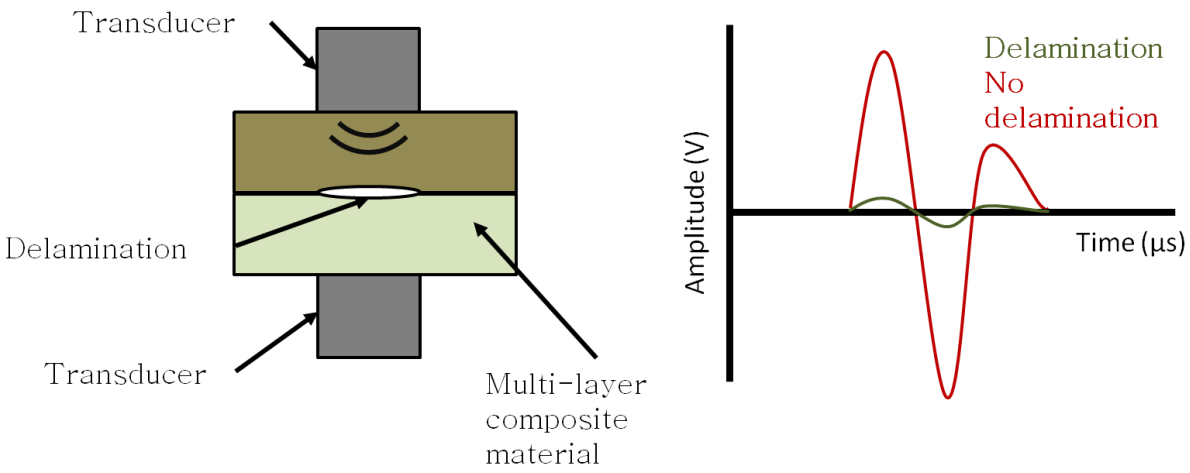

Figure 3. Illustration of standard through-transmission procedure.

1.2.2 Soft material methods and Quantitative Ultrasound (QUS)

However, these conventional ultrasound measurements do have several notable disadvantages. While the amplitude and time of flight information may prove adequate for detecting internal flaws and boundaries, this information provides little insight into the actual

structure of the material [1,23,24]. The resulting measurements and images may be open to interpretation and necessitate a skilled operator to correctly assess them [12]. Ultrasonic measurements which can relate directly to material properties and are not operator-dependent would therefore be valuable to health diagnostics and nondestructive testing. Much work has been done to solve this problem and has led to the field of Quantitative Ultrasound (QUS).

A number of quantifiable parameters have been studied in the literature. It has been shown that the sound speed is dependent upon the structure of tissue and has also been used to create images [25-31]. The speed of sound in is dependent on the material properties such as the density and stiffness. Tissue characterization based upon calculation of the attenuation coefficient has also been widely studied [26-33]. Attenuation is a measure of how much of the initial sound energy is lost to the material caused by either absorption because of viscous and thermal effects or by wave scattering due to the internal structure.

Quantitative ultrasound has not been restricted to only these types of measurements but has also included more complex parameters that combine both model and experiment. These measurements have extended beyond just the time domain and into the frequency domain. Spectral-based QUS was first studied by Lizzi and Feleppa in the 1980s [34-36]. By analyzing the characteristics of waveforms' power spectra they found that several physical parameters could be estimated. When a linear fit is performed on the frequency spectrum, the slope can be related to the size of the scatterers. The intercept correlates with the volume concentration of the scatterers as well as the acoustic impedance. It was also determined that spectral-based analysis is more robust to external influences introduced by the equipment. This allows for measurements to be more consistent across different laboratories. These methods are prevalent in literature and are still relevant today having been applied to rat models and human liver, renal, ocular and breast tissue [34-38].

By far the most popular spectral parameter is the backscatter coefficient [37-45]. This parameter is a measure of the sound intensity reflected back to the transducer in pulse-echo mode. This does differ from standard methods however. This measurement looks at the amplitude of the backscatter in the frequency domain, rather than just the maximum strength of time domain pulse. Several factors influence the frequency-dependent backscattered intensity. This value is reliant upon the size, shape, number, and material properties of the scatterers. The effects of these properties on the scattering of waves will be discussed more in depth in subsequent chapters. To properly calculate the backscatter coefficient the geometry and characteristics of the transducer must be taken into account. Several different formulations have been developed and consider unfocused and focused transducers, and even transducer arrays [38,40-45]. Methods to improve the measurement have also taken into account attenuation effects [46,47]. Once the backscatter coefficient is determined numerous models have been developed to relate the value to specific properties of the system such as size and concentration [38,47,48].

Other more advanced signal processing techniques are employed as well. One of these methods is the cepstrum [49]. This approach was originally developed for detecting echoes in earthquakes and in often used in speech processing. It is particularly useful for detecting periodicities in the frequency spectrum or the presence of higher order harmonics. It is defined as the inverse Fourier transform of the absolute value of the logarithm of the frequency spectrum. This method has been applied to tissues to determine the mean scatterer spacing [50,51]. Tissues, while not as organized as other materials, do possess some order of organization. This parameter attempts to quantify the overall characteristic spacing by considering the tissue to be composed of point scatterers with an average distance in between..This measurement has also been carried out using other methods such as autocorrelation functions or wavelets [52-54].

Wavelet transforms, or wavelets, are a relatively recent development. A wavelet transform is similar to the more traditional Fourier transform, but it has one key difference. Wavelets are interested in the frequency domain components of a signal as well as the time in which they occur. They are used on occasion for soft material ultrasound [55]. They have found used in standard pulse-echo methods through denoising or feature extraction [56-58]. However, they are far more commonly found in nondestructive fields using guided waves which we will touch on in a later section.

Over about the last 30 years another method of ultrasound imaging has been developed to visualize tissue based upon its mechanical properties. This field, known as elastography, creates images by detecting the local differences in the Young's modulus in the tissue. It has long been known that many tumors often feel to the touch like they have a different stiffness than the surrounding tissue. This technique of detecting tumors by squeezing them, called palpation, is hardly high-tech but is widely used [59]. Elastography performs essentially this process but uses the ultrasonic response to detect the difference in stiffness. This method works by measuring the local strains felt by the tissue during mechanical loading. The loading can be accomplished in several different ways. The tissue can be dynamically loaded, in which it is subject to a low frequency vibration, and an ultrasound signal can be conducted. Static loading is also possible. For this situation, a standard pulse-echo measurement is taken. The tissue is then compressed, typically < 1% strain, and the measurement is taken again. In this case, since there are two pulse-echo measurements, the relative time differences between the returned echoes can be calculated. The strain, and therefore the Young's modulus, can then be estimated which allows images based off of the tissue's stiffness to be created [23,60-63].

Standard medical ultrasound instruments typically operate from about 2-15 MHz While the resolution may improve with increasing frequency (Figure 4), unfortunately the attenuation increases as well which has led to high frequency ultrasound (>20 MHz) typically being used in only certain applications that do not require a large depth of penetration. Two fields in which high frequency ultrasound is used are ophthalmology and dermatology. Ophthalmological uses often include measuring cornea thickness and general imaging of the eye [64-65]. The increased resolution has made high frequency ultrasound useful for imaging skin since the penetration need not be large [66,67]. Intravascular imaging has also made use of high frequency ultrasound [68,69]. Ultrasonic endoscopes have also been developed for internal imaging [70]. Another specialized field which makes use of the increased resolution of high-frequency ultrasound is acoustic microscopy. Acoustic microscopes operate in a manner similar to optical and electron microscopes, but they use sound waves to probe the material. Typical setups use very high-frequency ultrasound of at least 50 MHz, but there do exist systems capable of using ultrasound in the GHz range [71]. First developed in the 1970s, acoustic microscopes have now even seen commercial development [72-74]. These microscopes have found use in industrial applications for small-scale flaw detection. This is particularly useful for testing the quality of electronic packaging and characterizing materials [75]. Acoustic biomicroscopes have also been developed to monitor cellular changes [76,77].

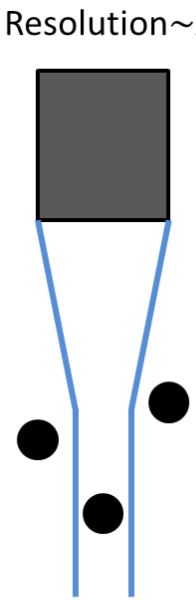

$$\lambda = c / f$$

Figure 4. Illustration of lateral resolution for pulse-echo methods.

A previous study by Doyle et al. evaluated various breast cancer pathologies using several Quantitative Ultrasound techniques at high frequency in an effort to correlate high frequency ultrasound with specific tissue microstructure [78]. They made use of conventional methods as well as new parameters comprising of the density of peaks within the frequency spectrum and the slope of the second Fourier transform of the power spectrum. The researchers found that the attenuation at 50 MHz, the peak density and the slope of the second power spectrum were the most susceptible to the different pathologies. In particular, peak density, or the number of extrema present in the frequency spectrum, was the parameter with the greatest sensitivity to tissue microstructure. This dissertation will largely be concerned with the measurement of the peak density measurement due to its novelty and response to material microstructure.

1.2.3 Hard material methods

While the ultrasonic methods we have discussed thus far have centered primarily on tissues and more generally soft materials, ultrasound is utilized for the structural mapping and characterization of other materials as well. We will next briefly touch on some of these methods here.

As with tissues, the standard methods described previously are most often used and while these techniques are more than adequate for many industrial needs, there are approaches better suited to certain applications as well as more quantitative methods. Several quantitative methods used for tissues are also used for hard materials. Attenuation and sound velocity measurements have proven fruitful for improved damage detection and the characterization of porosity [79-82]

The sound speed is also useful for determining the elastic properties of linear elastic materials nondestructively [19,83]. With the use of two transducers, one which creates longitudinal waves and one which creates shear waves, it is possible to determine the relevant moduli. For example, the Poisson's ratio ν can be calculated as

$$\nu = \frac{c_L^2 - 2c_s^2}{2c_L^2 - 2c_s^2}. \tag{1.1}$$

The Young's modulus E_Y can be found from the following equation

$$E_Y = \frac{c_L^2 \rho(1+\nu)(1-2\nu)}{1-\nu}. \tag{1.2}$$

In each equation, c_L is the longitudinal or compressions sound speed. The shear wave velocity is c_s, and the density is ρ. In addition to being a nondestructive method, this technique offers increased acquisition speed.

1.2.4 Bounded wave methods

In unbounded solids, sound can exist in two basic modes which can describe the wave propagation— compression and shear waves (this is discussed further in Chapter two). However, when considering real materials with real boundaries, these two wave modes can interact with the boundary, interfere and create more complicated wave patterns. For certain applications these new wave types can also be useful for ultrasonic testing.

At the interface of a fluid and a solid it is possible for waves to exist on the surface of the solid. While there are several types of surface waves, the most useful is the Rayleigh wave. This wave is capable of travelling long distances across the surface and is even able to traverse curves. Rayleigh waves are extremely sensitive to surface defects and sometimes too much so. They are able to detect flaws but do not reveal much additional information [18,19].

More useful for the study of hard materials the so-called guided waves. Also known as plate waves or Lamb waves, these waves only exist for the specific geometry of a thin plate. When the material properties, thickness, angle of incidence and ultrasound frequency are the appropriate values, the longitudinal and shear wave modes reflect from the exterior boundaries and interfere in a manner creating a new wave mode propagating parallel to the plate which is able to travel great distances. These properties make Lamb waves useful for large scale flaw detection for plates and composites since the waves propagate throughout the entirety of the plate. This allows for damage identification without the need for scanning the surface as with standard pulse-echo or through-transmission techniques. Instead, single sensors or sensor arrays are often used instead. These Lamb wave sensor arrays have seen significant use in structural health monitoring. Lamb waves are highly sensitive to internal flaws but they do typically require

further signal processing for accurate feature extraction. Similarly to tissue-based methods, guided waves make use of time of flight and frequency-based measurements. Wavelets are also widely used. Sensor array methods often make use of artificial intelligence algorithms including fuzzy logic, genetic algorithms and artificial neural networks [18,19,84-86].

These other ultrasonic propagation modes are of great interest to flaw detection and are certainly interesting in and of themselves. However, they are slightly outside the scope of this dissertation, and we will focus on the modes more commonly found in soft materials in the rest of the work.

1.3 Objectives

Originally motivated by the need for improved methods for surgical margin detection, this dissertation investigates ultrasonic techniques for improved material characterization and measurement. While ultrasonic evaluation may be a mature field, ample opportunity to contribute meaningful research still exists. Conventional ultrasound techniques are useful for probing internal structure and the detection of flaws, but these measurements may require skilled operators and do not detail the material characteristics. Extensive work has been done to obtain quantitative and more absolute results, and while useful, this work typically considers only a handful of parameters and has seen limited clinical use. High-frequency ultrasound, due to its increased attenuation, has also been relegated to select fields and is not widely used. In addition, peak density is a new parameter that has only seen use in one research group so far.

The objective of the work presented in this dissertation is the development of further methods for Quantitative Ultrasound analysis. Due to the relative lack of published results for high frequency ultrasound, this work aims to expand the knowledge of high frequency testing while assessing its potential for possible medical and industrial applications. Namely, this dissertation seeks to understand the relationship between high-frequency ultrasound and microstructure. As a relatively new measurement, peak density is as a means for micro-structural assessment, and the underlying physical mechanisms are studied through experimental and computational methods to gain insight into the measurement.

1.4 Outline of dissertation

Chapter two gives a brief outline of the relevant properties of acoustic scattering which make high-frequency ultrasound an interesting topic of study. Signal processing methods which are used throughout the work are also presented. This chapter also details the equipment used in this work and the process of developing an ultrasonic laboratory.

In Chapter 3 we discuss some of the initial ultrasonic measurements that were performed. To determine the feasibility of peak density measurements, peak density was used as a basis for image reconstruction of soft materials. This was investigated at different size and frequency scales and was compared with more standard amplitude techniques. Peak density based images were found to image these materials with a higher quality than the conventional method.

It was determined that peak density measurements were dependent on the specific signal processing technique used. Chapter four describes the optimization of peak density measurements by analyzing several different signal processing methods.

To understand the physics behind the peak density measurement, experiments using controlled scatterers in tissue-mimicking phantoms are conducted. Finite element analysis is used to model the acoustic scattering and is compared with experiment. The results of these studies are given in Chapter five.

Lastly, Chapter six concludes with an overall summary of the presented work and also outlines some recommendations for future studies of the peak density measurement.

Chapter 2.
Theory and experimental background

Much of the work presented in this dissertation is based on several central themes. This chapter gives a brief overview of the nature of sound and acoustic scattering. There also exist several core mathematical structures and experimental methods which will be used throughout the work, and this chapter serves to discuss these foundations.

2.1 Physics of sound

2.1.1 Sound waves

In the simplest terms, sound is the propagation of mechanical energy through a medium and is caused by the vibration of the particles. The particles are displaced due to changes in surrounding pressure. The vibration of the particles in turn creates additional pressure changes causing additional displacements. This sequence manifests its self as a wave. The wave travels with a speed c, has wavelength λ, and frequency f, which are governed by $c = \lambda f$. Figure 5 shows the two most common wave modes in a solid.

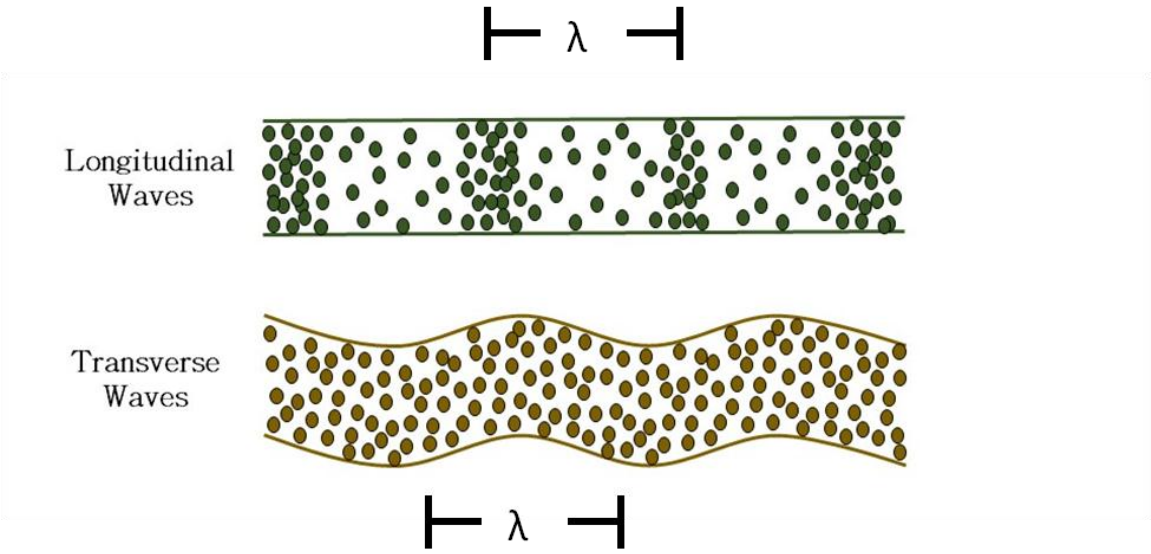

Figure 5. Diagram of the two basic wave propagation modes possible in a solid. Note that only longitudinal waves are possible in a liquid.

The propagation of sound can be much more easily represented in a fluid than solid, since fluids do not support the propagation of shears waves. The governing equation for acoustic waves in a fluid can be given by the wave equation for pressure [89]

$$\rho c^2 \nabla \cdot \left(\frac{1}{\rho}\nabla p\right) - \frac{\partial^2 p}{\partial t^2} = 0 \tag{2.1}$$

where t is time, c is the sound speed of the fluid, ρ is the density, and p is the pressure field..

Often times it is convenient to consider the steady-state solution to this equation or the results due to a pressure field which is time harmonic. This greatly reduces the complexity of the solutions as well as lets us investigate systems in regard to a fundamental part of waves— the frequency. Consider a pressure field stationary in time oscillating with a frequency f with wavenumber $k = 2\pi f/c$

$$p = p(f)e^{-2i\pi f t} \tag{2.2}$$

Then by substituting into equation (2.2) we obtain

$$\rho c^2 \nabla \left(\frac{1}{\rho} \nabla p(f) \right) + 4\pi^2 f^2 p(f) = 0, \tag{2.3}$$

$$\rho \nabla \left(\frac{1}{\rho} \nabla p(f) \right) + \left(\frac{2\pi f}{c} \right)^2 p(f) = 0, \tag{2.4}$$

If we instead consider the wavenumber rather than the frequency this becomes

$$\rho \nabla \left(\frac{1}{\rho} \nabla p(k) \right) + k^2 p(k) = 0. \tag{2.5}$$

Assuming a constant density in the medium this finally becomes the standard form of the Helmholtz equation

$$\nabla^2 p + k^2 p = 0 \tag{2.6}$$

This form of the wave equation will be important throughout this work.

In a solid, the sound wave propagation is governed by Navier's equation of motion

$$\rho_s \frac{\partial^2 \boldsymbol{u}}{\partial t^2} = (\lambda + \mu) \nabla (\nabla \cdot \boldsymbol{u}) + \mu \nabla^2 \boldsymbol{u}. \tag{2.7}$$

The material properties taken into account in this equation are time, t, the density of the solid, ρ_s, the displacement, $\boldsymbol{u}$, and Lamé's parameters μ and λ. There exist two plane wave solutions for the displacement field which correspond to compression, or longitudinal waves and also shear or transverse waves which propagate orthogonally to the compression waves.

Similarly to the fluid case we can consider the displacement field to being varying harmonically in time. Taking the displacement field to be of the form $\boldsymbol{u} = \boldsymbol{u}(k) e^{-2i\pi f t}$ and substituting into the time dependent Navier's equation we can arrive at the following equation

$$-\rho_s k^2 \boldsymbol{u} = (\lambda + \mu) \nabla (\nabla \cdot u) + \mu \nabla^2 \boldsymbol{u}. \tag{2.8}$$

2.1.2 Acoustic scattering

When a sound wave interacts with an object, a portion of the wave is deflected. The nature of the scattering is dependent on the impinging sound wave and the properties of the medium and scatterer. In general, there exist three main scattering regimes: specular, Rayleigh, and diffractive. Figure 6 summarizes these scattering types.

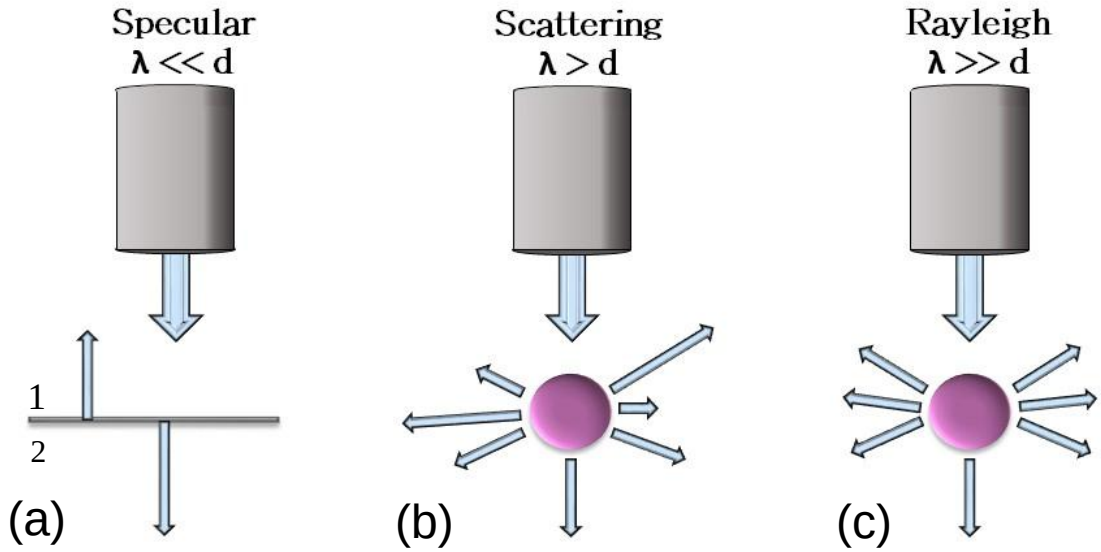

Figure 6. Illustration of the three main scattering regimes. We note that for the high-frequency ultrasound that is considered in this dissertation falls mainly in the second regime due to the small wavelength.

When the wavelength of the incident wave is much smaller than the scatterer, we are in the specular regime. For this type of scattering, the resulting waves can be thought of as largely geometrical in nature and can be described in a manner similar to geometric optics [18,87]. The amount of the wave reflected and transmitted by the object is dependent on the acoustic impedance, of the object and the surrounding medium. The acoustic impedance is the measure of a material's resistance to a driving acoustic pressure and is defined as

$$Z = \rho c, \tag{2.9}$$

where ρ is the density and c is the sound speed. The percentages of the reflected and transmitted waves are governed by the following relations where the subscripts 1 and 2 correspond to the configuration shown in Figure 6a: [18,19]

$$\%\, reflection\ R = \left(\frac{Z_2 - Z_1}{Z_2 + Z_1}\right)^2 \tag{2.10}$$

$$\%\, transmittance\ T = \frac{4Z_1Z_2}{Z_1 + Z_2}. \tag{2.11}$$

On the other side of the spectrum, we can discuss the scattering for the case of large wavelength and small scatterer, typically known as Rayleigh scattering. In this regime, the wave is scattered nearly equally in all directions. In important relation given in Lord Rayleigh's original 1871 paper is the amount of scattering in this region is proportional to f^4, where f is the frequency of the incident sound wave [88].

In the third regime, when the wavelength of the sound wave is on the same order as the size of the scatterer, the scattered wave can no longer be described with as simple of relations as for the previous cases. High-frequency ultrasound holds interest largely due to its existence in this scattering regime for typical soft materials. To better understand the scattering of high-frequency ultrasound, we briefly discuss a few general acoustic scattering models and their consequences.

This scattering regime has been of interest to many researchers over the years. Analytical solutions have been found for simple geometries as well as more complex and arbitrary shapes. Numerical methods have also been employed. However, to gain a fundamental understanding of the physics, we will discuss only some basic models commonly used for ultrasound. Mainly, we will consider the solutions for spheres immersed in a surrounding fluid and isonified by a plane wave.

The following is a generalization of the derivations found in part in [89-93] for various boundary conditions.

Consider a plane wave travelling in the positive x direction in a medium with wavenumber k, sound speed c, and at time t

$$p_i = P_0 e^{-ik(x-ct)} = P_0 e^{-ik(r\,cos\theta - ct)} \tag{2.12}$$

The variables of r and θ correspond to the usual polar coordinates. To simplify the problem, we consider a time harmonic pressure wave which allows us to ignore the time component. Since the scattered wave will be spherical in nature, it is useful to rewrite the incident pressure wave using the plane wave expansion:

$$p_i = P_0 \sum_{l=0}^{\infty} (2l+1) i^l j_l(kr) P_l(\cos\theta) \tag{2.13}$$

where j_l is the spherical Bessel function of the second kind and P_l are the Legendre polynomials. Next, we assume the scattered wave to be in the form of an outgoing spherical wave. This is given by

$$p_s = -P_0 \sum_{l=0}^{\infty} (2l+1)\,(-i)^{l+1} \sin\eta_l\, e^{i\eta_l} h_l^{(2)}(kr) P_l(\cos\theta) \tag{2.14}$$

where $h_l^{(2)}$ is the spherical Hankel function of the second kind and η_l is the associated phase shift of the l^{th} wave due to the properties of the scatterer. By applying the appropriate boundary conditions on the surface of the sphere, the phase shifts can be determined and a formula for the scattered wave obtained.

Let us now consider the case of a hard or rigid sphere of radius a. This implies that the displacement at the surface of the sphere is zero. For the pressure, this implies Neumann boundary

conditions, or $\frac{\partial p_i}{\partial r} - \frac{\partial p_s}{\partial r} = 0$. This problem has been solved by many authors, and the phase shift is given by

$$\sin \eta_l e^{i\eta_l} = \frac{j_l'(ka)}{h_l^{(2)'}(ka)}. \tag{2.15}$$

where the prime denotes the first derivative of each function.

In acoustics, it is often useful to look at the propagation at distances far from the sphere. In this case, we can take the asymptotic expansion for $h_l^{(2)}$ as $r \to \infty$:

$$\lim_{x\to\infty} h_l^{(2)}(x) = \frac{i^{l+1}e^{-ikx}}{x}. \tag{2.16}$$

This then gives the far field scattered pressure for the rigid sphere as

$$p_{s,far} = -P_0 \sum_{l=0}^{\infty} (2l+1)\,(-i)^{l+1} \frac{j_l'(ka)}{h_l^{(2)'}(ka)} i^{l+1} \frac{e^{-ikr}}{r}\, P_l(\cos\theta) \tag{2.17}$$

or

$$p_{s,far} = \frac{e^{-ikr}}{r}\Phi(\theta) \tag{2.18}$$

where

$$\Phi(\theta) = \sum_{l=0}^{\infty} -(2l+1)\frac{j_l'(ka)}{h_l^{(2)'}(ka)}\, P_l(\cos\theta). \tag{2.1}$$

Next, let us consider the other limiting case of a sound soft sphere. In this case, we have Dirichlet boundary conditions, and the total pressure is zero at the sphere's surface:

$$p_i + p_s = 0. \tag{2.20}$$

As before, we assume a scattered wave of the form of equation (2.14). When the boundary conditions are applied the resulting phase shift is

$$\sin\eta_l e^{i\eta_l} = \frac{j_l(ka)}{h_l^{(2)}(ka)} \tag{2.21}$$

which gives the scattered pressure

$$p_s = -P_0 \sum_{l=0}^{\infty} (2l+1)\,(-i)^{l+1} \frac{j_l(ka)}{h_l^{(2)}(ka)} h_l^{(2)}(kr) P_l(\cos\theta) \tag{2.22}$$

and the scattered far field

$$p_{s,far} = \frac{e^{-ikr}}{r}\Phi(\theta), \Phi(\theta) = \sum_{l=0}^{\infty} -(2l+1)\frac{j_l(ka)}{h_l^{(2)}(ka)}\, P_l(\cos\theta). \tag{2.23}$$

The previous cases do have use, but ultimately they are just simplifications of the scattering of an elastic sphere. The case of an elastic sphere was solved by both Faran and Hickling and considered the shear waves generated inside the sphere as well [92,93]. Next we show an overview of the derivation for this case.

Let there exist an elastic sphere of radius a with wavenumber k, sound velocity c, and density ρ be immersed in a fluid of wavenumber k_3, sound velocity c_3, and density ρ_3. We assume the same form for p_i and p_s as for the previous cases and where we need to solve for the phase shift η_l. Now, let us consider the boundary conditions which take into account the solid mechanics of the sphere which is governed by Navier's equation of motion in the absence of body forces:

$$\rho\frac{\partial^2 \boldsymbol{u}}{\partial t^2} = (\lambda+\mu)\nabla(\nabla\cdot\boldsymbol{u}) + \mu\nabla^2\boldsymbol{u}. \tag{2.24}$$

The boundary conditions at the boundary $r = a$, where T is the stress tensor of the solid

1. Fluid pressure is equal to normal stress component of solid: $p_i + p_s = -T_{rr}$.
2. Normal displacements are equal: $u_{i,r} + u_{s,r} = u_{solid,r}$.
3. Shear stress is zero: $T_{r\theta} = T_{r\phi} = 0$.

The authors went through the arduous task of matching these boundary conditions and obtained the following result for the phase shift:

$$\eta_l = \tan^{-1}\left(\frac{\tan\big(\delta_l(k_3 a)\big)\,[\tan\Phi_l + \tan\alpha_l(k_3 a)]}{\tan\Phi_l + \tan\beta_l(k_3 a)}\right) \tag{2.25}$$

where

$$\tan\alpha_l(x) = -\frac{x j_l'(x)}{j_l(x)}, \tag{2.2}$$

$$\tan\beta_l(x) = -\frac{n_l'(x)}{n_l(x)}, \tag{2.27}$$

$$\tan\delta_l(x) = -\frac{j_l(x)}{n_l(x)}, \tag{2.28}$$

$$\tan\Phi_l = -\frac{\rho_3}{\rho}\tan\zeta(ka,\sigma), \tag{2.3}$$

$$\tan\zeta(ka,\nu) = -\frac{x_2^2}{2}\left[\frac{\dfrac{\tan\alpha_l(ka)}{\tan\alpha_l(ka)+1} - \dfrac{l^2+l}{l^2+l-1-\frac{1}{2}x_2^2+\tan\alpha_l(x_2)}}{\dfrac{l^2+l-\frac{1}{2}x_2^2+2\tan\alpha_l(ka)}{\tan\alpha_l(ka)+1} - \dfrac{(l^2+l)(\tan\alpha_l(x_2)+1)}{l^2+l-1-\frac{1}{2}x_2^2+\tan\alpha_l(x_2)}}\right], \tag{2.30}$$

and

$$x_2 = ka\sqrt{\frac{2(\nu-1)}{2\nu}}. \tag{2.31}$$

The Poisson ratio for the sphere is given by ν and n_l is the spherical Bessel function of the second kind. In the far field, this goes as

$$p_{s,far} = \frac{e^{-ikr}}{r}\Phi(\theta), \Phi(\theta) = \frac{-1}{k}\sum_{l=0}^{\infty}(2l+1)(-i)^{l+1}\sin\eta_l\, e^{i\eta_l}\, P_l(\cos\theta). \tag{2.32}$$

As mentioned previously, the results for the hard and soft spheres are ultimately the limiting cases for this solution. The same results can be achieved for the hard sphere using this equation by letting $\rho_3 \to \infty$ and by letting $\rho_3 \to 0$ for the soft sphere.

To get a more intuitive understanding of the scattering, we next present the scattered far fields for different scatterers. We are mainly interested in the angular dependence $\Phi(\theta)$ of the scattered field, and to simplify the calculation we plot the magnitude of (2.32) at a distance of 1 meter. Figure 7 shows the resulting scattered fields for a sphere immersed in water with radius $a = 50\ \mu m$ and made out of different materials. For the water, $\rho = 1\ g/cm^3$ and $c = 1540\ m/s$. The various material properties are shown in Table 1.

Table 1. Properties used for polar plots in Figure 7. Values are taken from references [38,94]

Case	$\rho_3 \left(\frac{g}{cm^3}\right)$	$c_3 \left(\frac{m}{s}\right)$	σ
Hard	∞	-	-
Aluminum	2.7	6300	.33
Glass	2.5	5570	.22
Fat	.94	1460	.4993
Soft	0	-	-

Frequency (MHz)	0.1	15	30	63	100
Wavelength (um)	15400	101	50	25	15

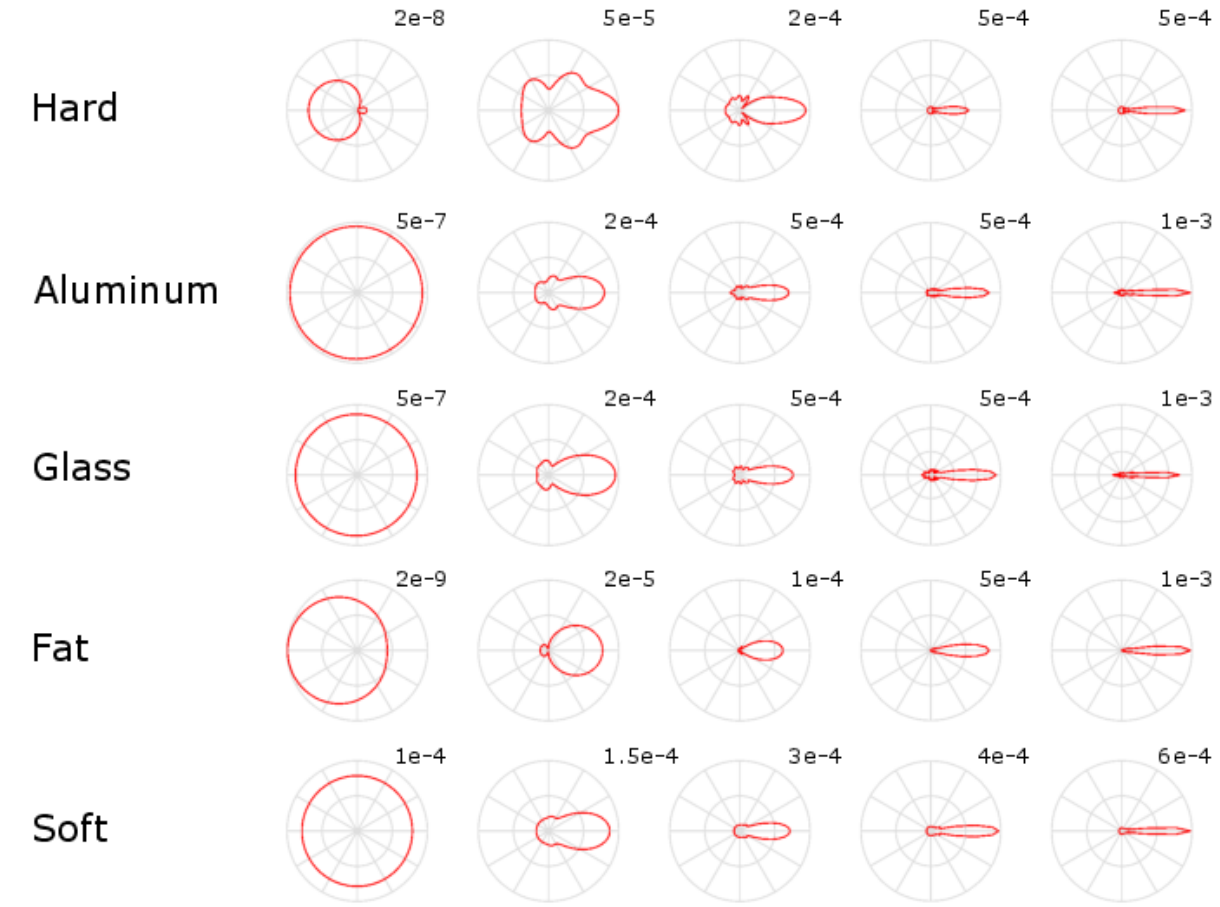

Figure 7. Polar plots showing the scattered sound field for a sphere with a radius of 50µm composed of varying materials isonified by high-frequency ultrasound. The hard sphere denotes a perfectly rigid sphere which scatters all of the sound. The soft sphere is essentially an infinitesimally dense sphere which has a zero pressure condition on the surface. The plots for the other spheres consider the elastic properties of the spheres to calculate the field.

2.2 Signal processing

2.2.1 Fourier transform

Many of the measurements carried out in this work rely on numerous signal processing techniques. Presented here is a brief overview of the various methods used. One of the most commonly utilized techniques is the Fourier transform. Defined as

$$f(x)=\int_{-\infty}^{\infty} F(k)e^{2\pi ikx}\,dk \qquad (2.33)$$

$$F(k)=\int_{-\infty}^{\infty} F(k)e^{-2\pi ikx}\,dx \qquad (2.34)$$

the Fourier transform allows for a function to be expressed in a different variable using an alternate set of basis functions- in this case the transformed function is expressed as a sum of sine and cosines [95,96]. When applied to time-domain signals, the application of the Fourier transform allows the original signal to be separated into its constitutive frequency components. This is particularly useful when the input signal is composed of several different frequencies and the value of the resonant frequencies of the system is desired.

However, it is known that real-world signals are not continuous but rather are discrete. This implies that when it is desired to transform a discrete signal the integral formulation is no longer applicable. In this instance a discrete Fourier transform (DFT) is used. The DFT is defined as follows: [95]

$$F_k = \sum_{n=0}^{N-1} f_n e^{\frac{2\pi ikn}{N}} \qquad (2.35)$$

$$f_n = \frac{1}{N}\sum_{n=0}^{N-1} F_k e^{\frac{2\pi i k n}{N}}. \quad (2.4)$$

For a large signal however, the DFT becomes computationally expensive. A computationally efficient method for calculating the DFT was first developed in 1965 by Cooley and Tukey [97]. Known as the fast Fourier transform (FFT), this algorithm allows for the Fourier transform to be viable as an investigative tool and is the reason for the wide use in all scientific disciplines. While several different FFT algorithms exist, the most regularly used is the original Cooley and Tukey formulation.

2.2.2 Hilbert transform

Another standard signal processing technique used here is the Hilbert transform [96]. The Hilbert transform allows for the analytic signal of the signal to be determined and in turn its envelope. The envelope of the signal shows the instantaneous features of the signal such as the amplitude. An illustration of the resulting envelope is shown in Figure 8.

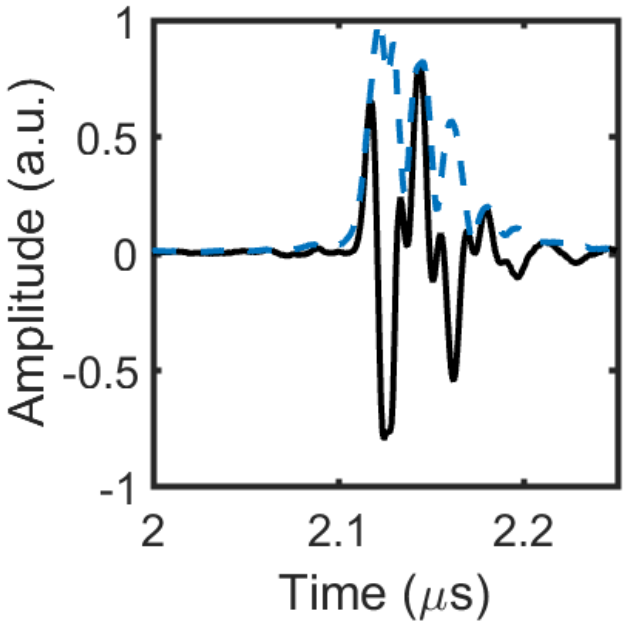

Figure 8. Example of pulse and envelope found from the Hilbert transform.

The Hilbert transform is defined as [95,96]

$$\mathcal{H}[f(x)] = \frac{1}{\pi} P.V. \int_{-\infty}^{\infty} \frac{f(x)dx}{x-y}, \tag{2.5}$$

where $P.V.$ is the Cauchy Principal Value. As with the Fourier transform, the discrete analog is needed for real-world signals. Fortunately there exists an efficient method for its calculation. A flowchart showing the details of the algorithm is shown below [101].

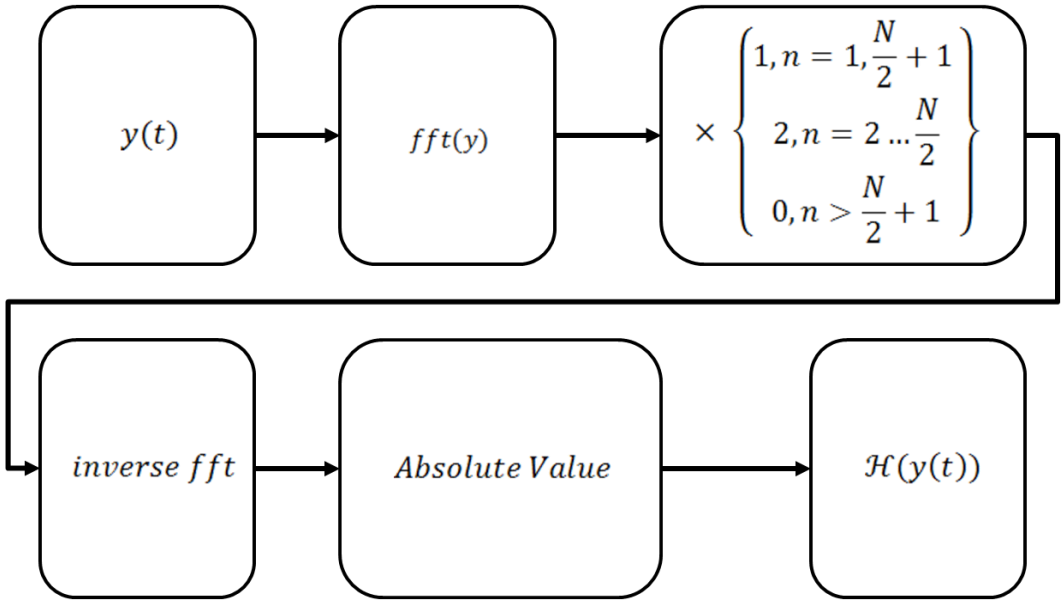

Figure 9. Flow chart of the calculation of the Hilbert transform.

2.2.3 Peak density

The last parameter that will be discussed is peak density. This parameter, coined by Doyle in 2011, was discovered to vary with different breast tissue pathologies [78]. This parameter is of great interest and is an integral part of this dissertation. It is defined as the number of peaks and valleys present in the frequency spectrum of the received ultrasonic pulse. To illustrate this, two example spectra are shown in Figure 10. Upon inspection, it is clear that Figure 10(a) has less peaks, and therefore a lower peak density, than (b). The left spectrum has a peak density of five, and the right spectrum has a peak density of eleven. This calculation can be done by visual examination, but this process can also be done automatically. Since the peaks and valleys are just the local extrema of the function, we can identify them by taking the numerical derivative of the spectrum. Counting the number of times the derivative crosses the x axis then gives us the

number of extrema, i.e., the peak density. We do note that this method will fail for very noisy spectra, and a method for determining peak density in this case is discussed in Chapter 3.

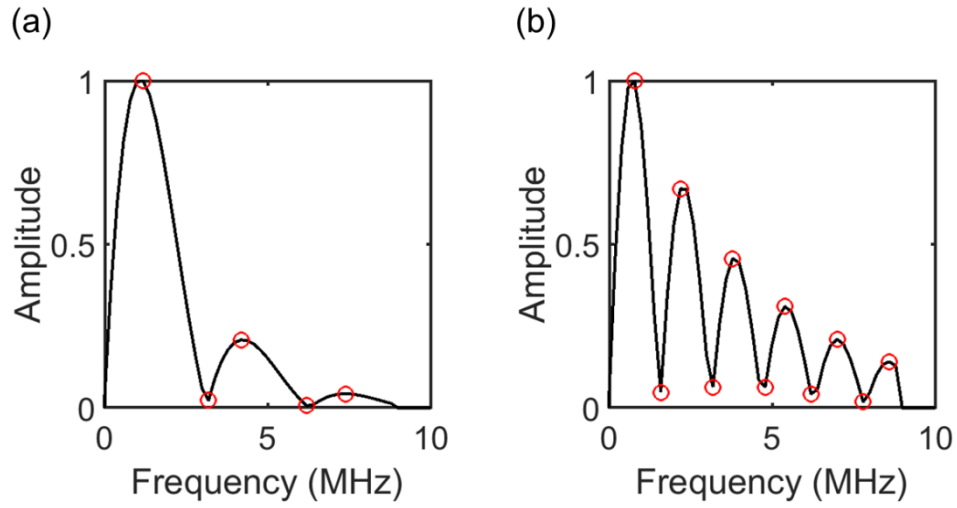

Figure 10. Example frequency spectra demonstrating the peak density measurement. Counted peaks and valleys are shown by the circles.

2.3 Ultrasound generation and acquisition

Due to the specific nature of this work, specialized instrumentation was necessary to obtain the desired measurements. A significant portion of this dissertation was devoted to the development and implementation of the experimental equipment. This section briefly describes this process and the underlying background.

In order to generate ultrasonic waves, piezoelectric materials are typically used [18,19,23,95]. Due to the physical properties of piezoelectrics, these materials undergo deformation when an electric field is applied. In turn, the piezoelectric material is also able to generate an electrical signal when placed under loading. These characteristics prove to be

particularly advantageous for many applications. Piezoelectrics serve as the critical component of ultrasound transducers. An illustration of an ultrasound transducer is shown in Figure 11.

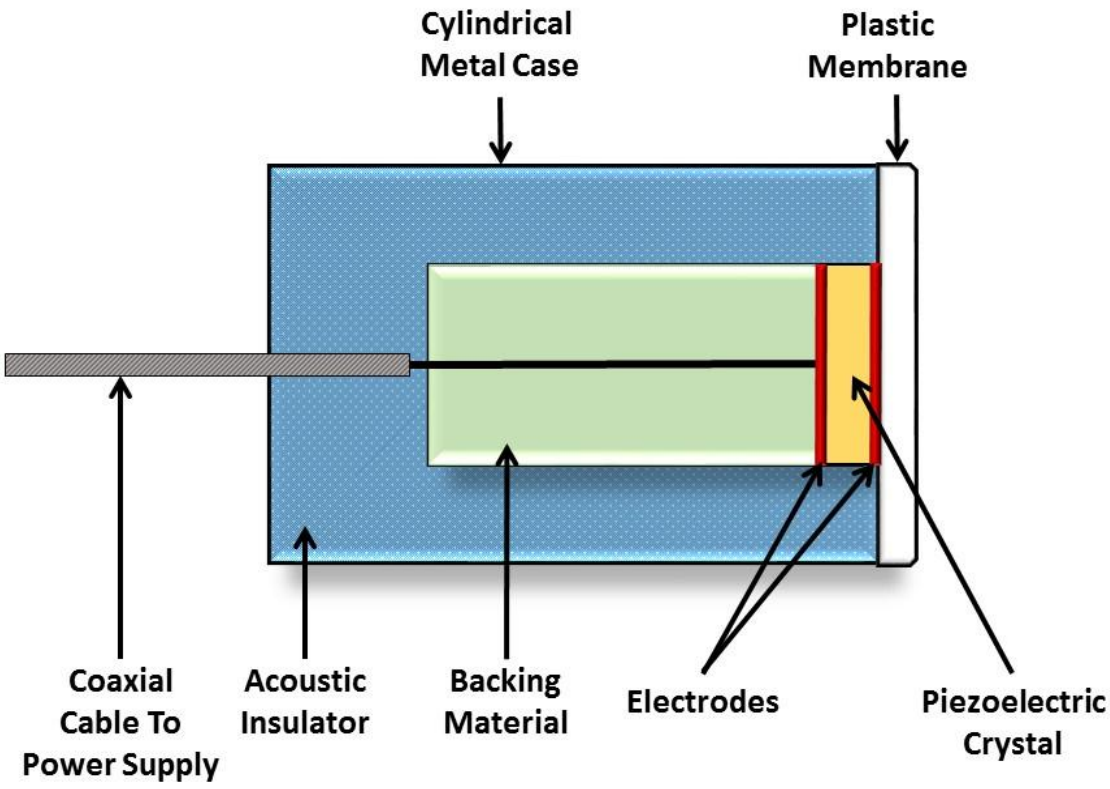

Figure 11. Diagram of standard ultrasound transducer.

The piezoelectric is typically a thin wafer and is housed in the transducer casing. By carefully selecting the constitutive material and thickness of the wafer the desired frequency response can be obtained. In addition to the piezoelectric wafer, an acoustically insulating backing material is placed behind the piezoelectric to dampen the oscillation and help fine tune the output pulse.

Different electrical signals can be used to drive the transducers and vary according to the application. For the high-frequency ultrasound we are concerned with here, the optimal driving waveform is a high voltage impulse or narrow square wave excitation. This voltage spike causes the piezoelectric to vibrate which creates a pulse of sound composed of several different frequencies. In the experimental work presented in this thesis a UTEX UT340 Pulser-Receiver (UTEX Scientific Instruments Inc., Mississauga, Ontario, Canada) was used to create the ultrasound waves. This instrument is capable of producing a narrow square wave pulse with width on the order of nanoseconds. The apparatus is also capable of receiving ultrasound pulses and amplifying the signals for later analysis. Low-noise amplification is necessary due to the relatively low signal strength of the ultrasound pulse. The received signal is then passed to an oscilloscope to be digitized in order to be analyzed later. A diagram demonstrating this process is shown below.

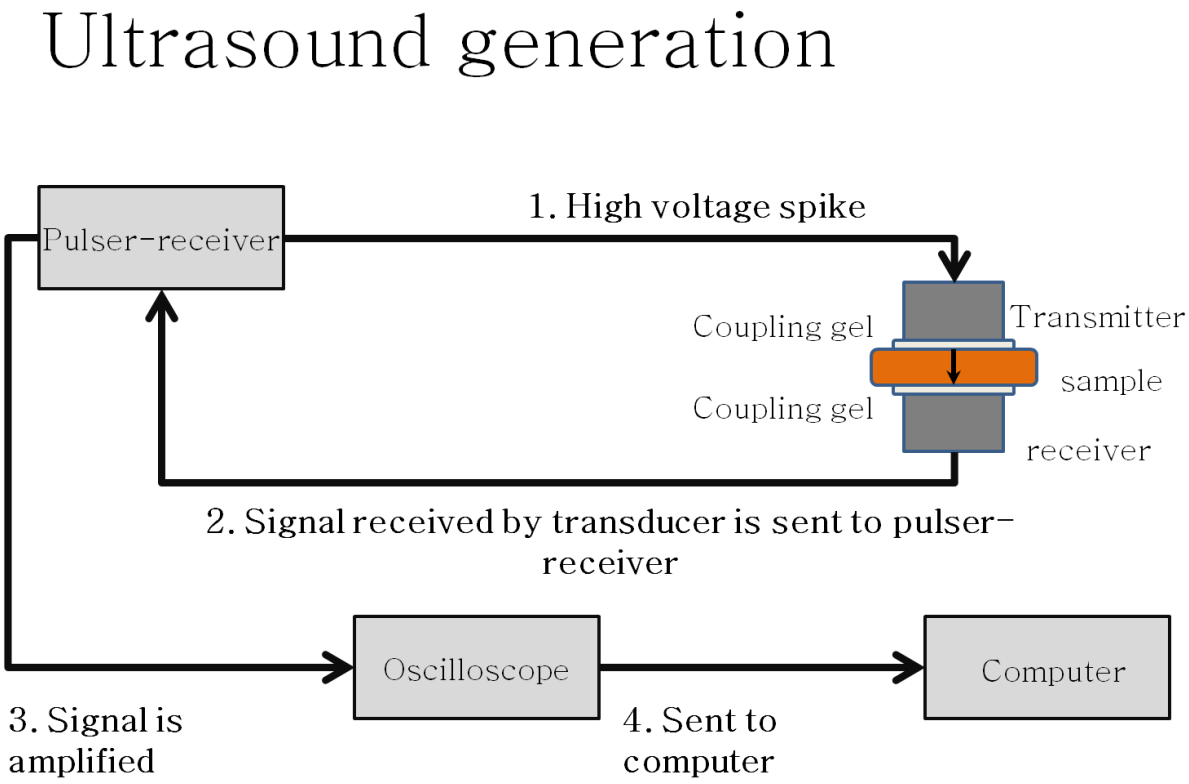

Figure 12. Schema for ultrasound generation and measurement.

In his work we used a Tektronix DPO 3052 Digital Phosphor Oscilloscope (Tektronix, Inc., Beaverton, OR). This oscilloscope has a bandwidth of 500 MHz and can take 2.5 billion samples every second. The bandwidth denotes the frequency range the device is able to measure and is recommended to be five times the highest required frequency. The sampling rate is selected in order to satisfy the Nyquist Criterion in which a signal must be sampled at least twice the rate of the highest desired frequency [102]. We wish to measure signals ranging from approximately 20-40 MHz and these settings were chosen to meet these requirements.

In order to expedite the measurement process the equipment was interfaced with LabView software (National Instruments, Austin, TX). Virtual instruments (VIs) were created which allow

the user to set parameters, control the equipment, and record received data. This process was ultimately compiled into a single VI for full experimental automation.

There exist two basic transducer configurations for conducting actual ultrasound measurements: pulse-echo and through-transmission. Pulse-echo measurements make use of a single transducer which both sends the pulse and receives the echo. Through-transmission, also commonly referred to as pitch-catch, uses a setup consisting of two separate transducers; one transducer which creates the signal and one which is the receiver. The following figure is a diagram of both setups.

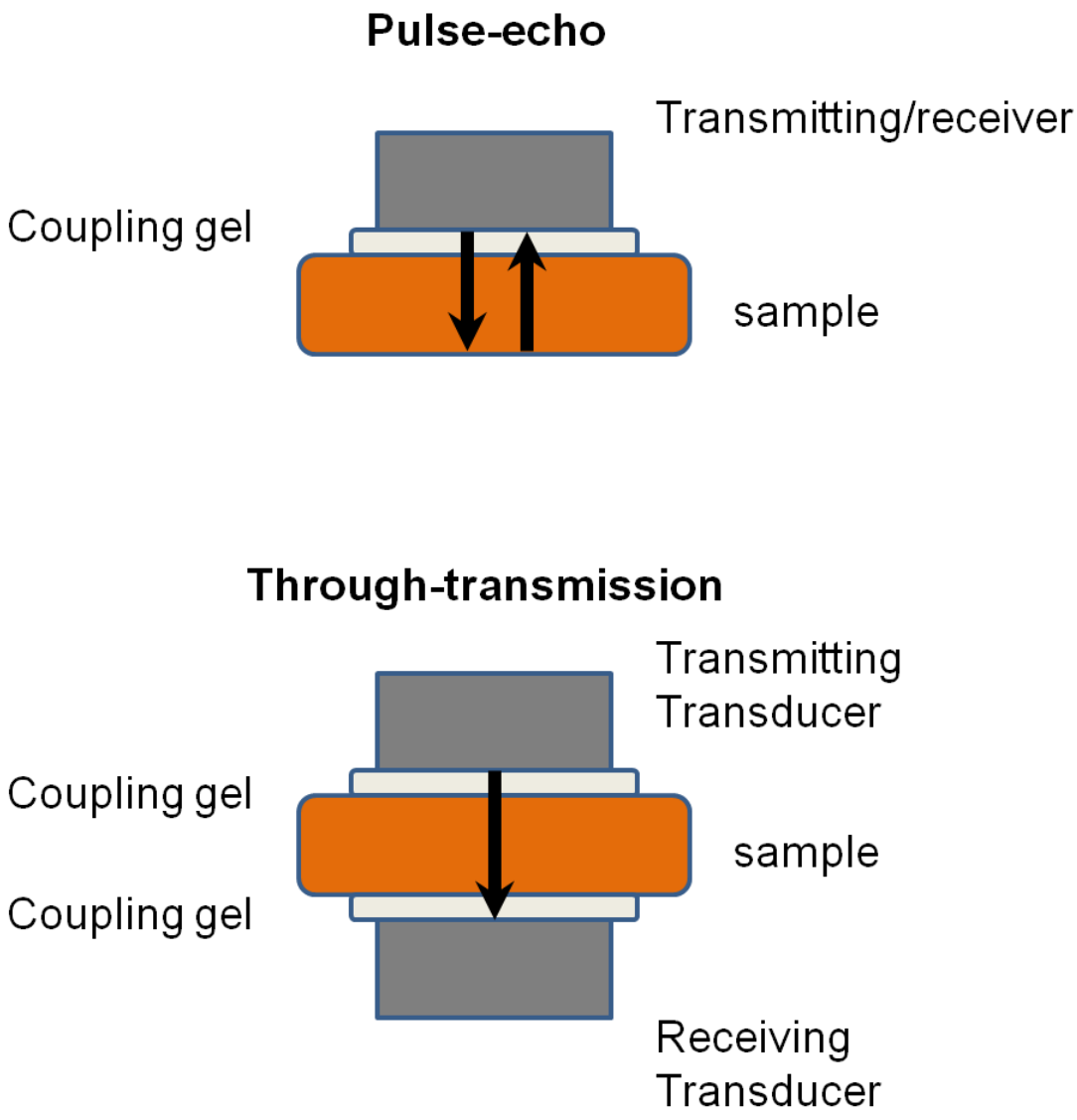

Figure 13. Diagram of the two standard transducer configurations.

A couplant is often used to maximize the sound propagation from the transducer face to the sample material. The couplant is a fluid which is used to ensure proper contact and displace any air which may attenuate the signal. Common techniques include immersing the sample and transducer in a liquid bath, usually consisting of water or oil. Specially formulated viscous gels may also be used which adhere to the surface of the material. The previous figure shows an

example of this type of couplant. Our laboratory uses a coupling gel similar to what can be found in hospitals (Sonotech Clear Image, Magnaflux INC, now NEXT Medical, Branchburg, NJ). It is also noted that while most applications do make use of fluid couplants, there exist several applications which utilize air-coupled ultrasound [98-100].

2.4 Experimental apparatus design and setup

The measurements we wished to perform used the through-transmission transducer configuration which presented some unique challenges. Several design requirements were taken into account. Over time the experimental design went through several iterations, and this section illustrates this process.

The most critical requirement was holding and aligning the two transducers. In order to obtain the best signal, the two transducers needed to be along the same vertical axis as closely as possible. In interest of taking multiple measurements on a single sample it was valuable to have the ability to reposition the sample or transducers. We also had transducers of different shapes and sizes, and an apparatus that could accommodate for this would be advantageous. Our initial measurements made use of larger, 0.5 MHz transducers (CMRF0.54, NDT Systems, Huntington Beach, CA). The original design consisted of a chemistry ring stand with clamps. The clamps were more than sufficient to grasp the transducers. The clamps could also be repositioned on the stand. This made it is possible to align the transducers. Multiple measurements were taken by cautiously moving the sample between the transducers while maintaining a sufficient amount of coupling gel in between. This was arduous, but good measurements were still possible with care. A photograph of this apparatus is shown in Figure 14.

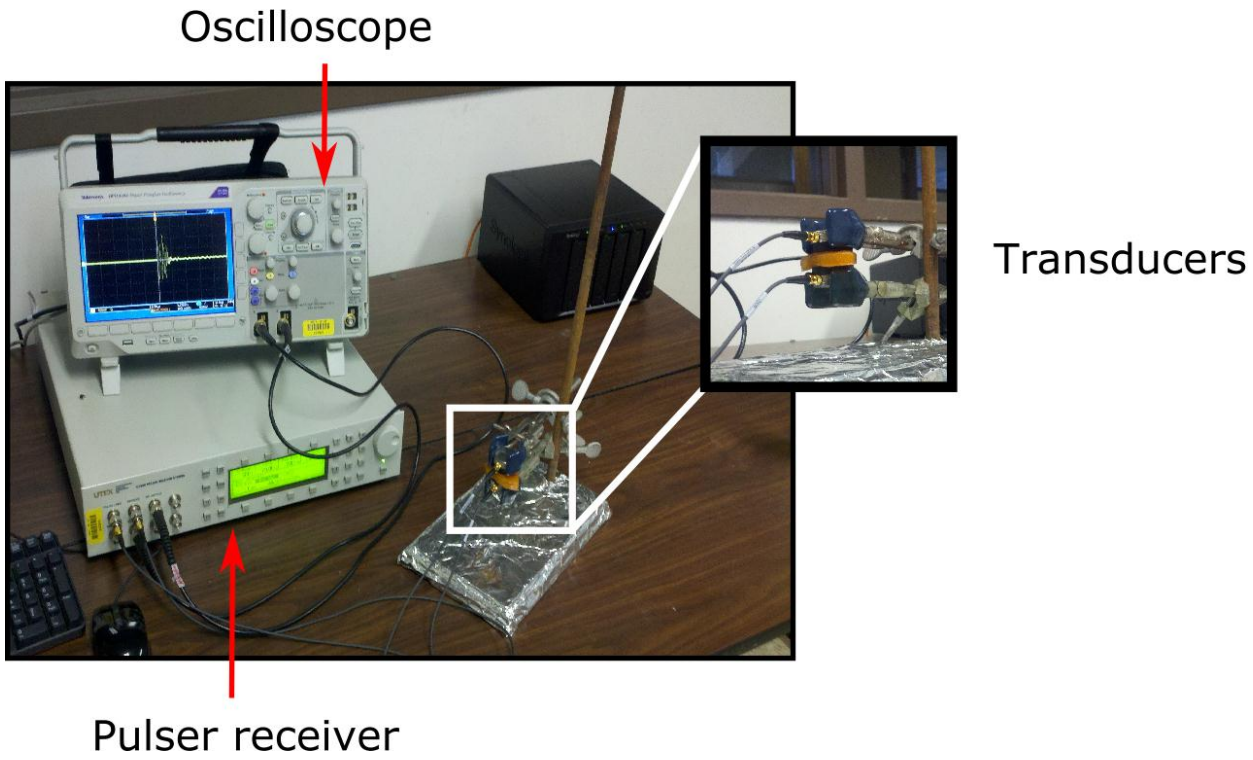

Figure 14. Photograph of the first iteration of the experimental setup.

While this first iteration was sufficient, it became obvious that the design could be improved. In addition to simplifying the measurement process, we also acquired new, small-scale, high-frequency transducers. These transducers were corneal pachymeters (are used by ophthalmologists to measure the thickness of the cornea) and come in a non-standard housing. A sketch of the pachymeter is shown in Figure 15.

Figure 15. SolidWorks drawing of the pachymeters.

Another measurement stage was then constructed to hold the pachymeters. The new setup held the transducers while better facilitating sample movement. It gave four axis control over the sample and transducers: x-y-z movement for the sample and z axis for one of the transducers. The micrometers provided increased precision and allowed for 0.01 inch increments. This made certain the sample was translated the proper distance for each measurement and streamlined the process for mapping measurements across the sample.

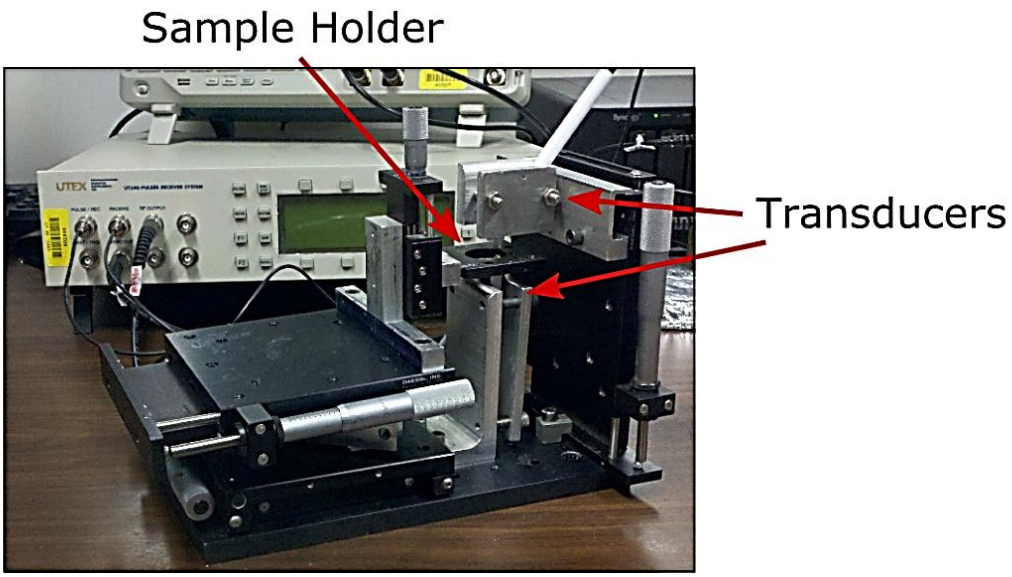

Figure 16. Photograph of the improved sample holder. This stage allowed from more rapid measurement and higher precision.

The second iteration of the sample stage proved to be more than capable of carrying out the required ultrasonic tests. However, the measurement process, while faster than the previous stage, was still time consuming. A small 1 cm x 1cm region consists of at least 100 separate measurements which could take multiple hours in all. In the interest of efficiency an automated stage was desired. The present version uses repurposed stepper motors to translate the sample and transducers. The stepper motors provide y-z axis control for the transducers and x axis control for the sample. The height of the sample stage is adjusted using set screws. A photograph of the automated stage is shown in Figure 17.

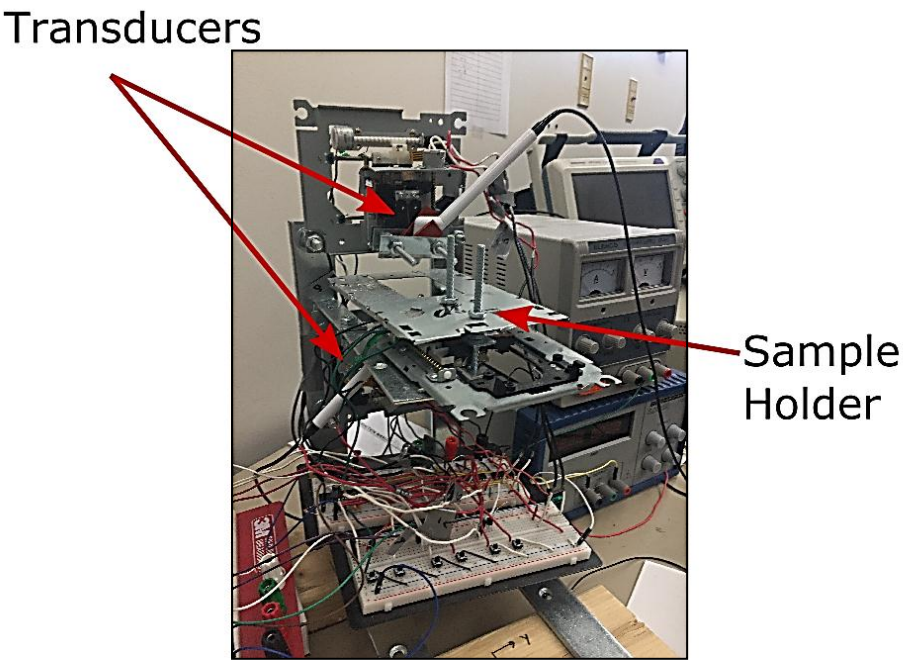

Figure 17. Final version of the sample stage. This device was integrated with LabView for full experimental automation.

The stepper motors can be controlled with two different interfaces. Push button control is provided through the use of an Arduino development board (Arduino, Italy). The stepper motors can also be commanded with LabView using the PC's serial port. This motor control VI is interfaced with the ultrasound generation and acquisition VI allowing fully automated, single click control over data acquisition.

Chapter 3.
Feasibility of peak density measurements and algorithm development

This section describes the initial ultrasound measurements performed. In particular, we examine the peak density method described by Doyle [78]. In their study this method was found to be reliant on the microstructure of the tissue examined. Owing to the limited studies of the parameter, we examined its potential for imaging soft materials at different frequency scales. We discuss the measurement and calculation of this parameter along with a spectral energy measurement. Two dimensional images are created for each parameter and are compared to more conventional amplitude techniques. The quality of the images is assessed for their ability to detect internal inclusions. The spectral based parameters were determined to locate inclusions just as well, if not better than the conventional method. The results of this chapter can also be found in [104].

3.1 Experimental procedure

3.1.1 Sample preparation

Tissue-mimicking phantoms were created using a mixture of Knox gelatine (Kraft Foods Global, Northfield, IL, USA) and psyllium fibre powder (Equate, Wal-Mart, Bentonville, AR, USA) [103]. Three phantoms were prepared with varying inclusions to test sensitivity to the size

of inclusions, resolution and variation due to sample thickness of different post processing techniques (amplitude, peak density and spectral energy). Phantom 1 was 2.15 cm thick and contained two pennies and two popcorn kernels. These were chosen as inclusions due to their availability and the significant difference in acoustic properties from the surrounding phantom. This choice of inclusions also helped minimize decomposition of the phantom. The second phantom had a thickness of 2.1 cm and contained an aluminium slab in addition to pennies and several popcorn kernels as inclusions. The aluminium slab spanned the height of the phantom with minimal phantom material above and below. This was done to insure that the signals would measure the properties of the slab and not the phantom-aluminium interface. The last phantom was created for use with higher frequency transducers. This phantom was thinner (2.1 mm) to account for the attenuation that occurs for high frequency ultrasound. This phantom also contained different inclusions using one hard pepper seed and two softer pepper flakes. These materials provided a contrast in stiffness and acoustic properties but are less extreme than the other inclusions used. An image of the surface of this phantom is shown in Figure 18.

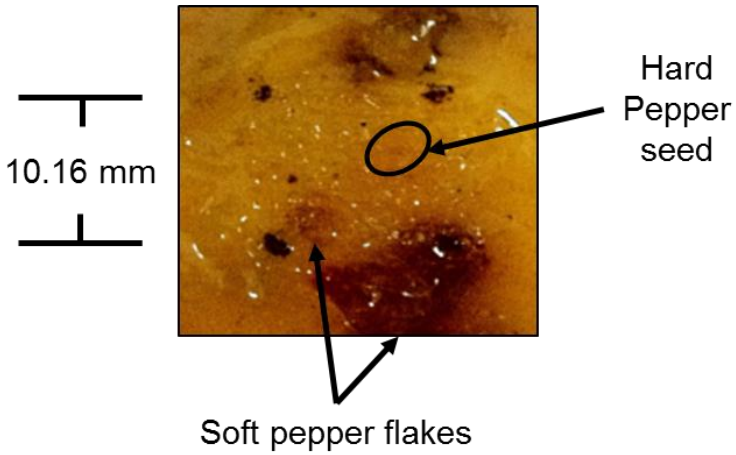

Figure 18. Photograph showing an example of a phantom used in this study. This was phantom 3 and was used for high frequency measurements. The black dots are ink and were used for alignment purposes.

3.1.2 Data acquisition

Ultrasound measurements were taken using two different pairs of ultrasonic transducers to allow for multiple frequencies. For low frequency measurements, two 0.5 MHz, 0.5 inch delay-line transducers (CMRF0.54, NDT Systems, Huntington Beach, CA, USA) were used. High frequency measurements were performed using two corneal pachymeters (25 MHz, 2mm diameter, TransducerWorks, Centre Hall, PA, USA) which were chosen for their increased resolution due to the small diameter and high frequency. Each transducer pair was operated in through-transmission mode and the signals were generated and received by a high frequency pulser-receiver (UT-340, UTEX Scientific Instruments Inc., Mississauga, Ontario, Canada). The transducers were coupled to the phantoms using Sonotech Clear Image scanning gel. Waveforms were digitized at 1.25 GS/s using a digital oscilloscope (DPO 3052, Tektronix, Inc., Beaverton, OR, USA) and to reduce noise the first 512 pulses were averaged. Signal generation and acquisition was automated with LabView (National Instruments). The transducers and samples were held on custom built mounts to facilitate imaging. Photographs of the equipment are

given in Fig. 2. The apparatus shown in Figure 14 was originally built for single measurements and was used for the low frequency measurements. However, this was found to be difficult to use for imaging and a second apparatus, shown in Figure 15(b), was later built. The high frequency measurements presented here were taken using this device. This design allows for transducers of varying diameters to be used and has a movable stage which can controlled in 0.01 inch (0.254 mm) increments. Also, through-transmission measurements were used in this study, but the apparatus allows for traditional pulse-echo measurements to be taken as well. Samples were scanned using a standard raster scan pattern with a step size that half the width of each transducer with 7 mm for low frequency and 1 mm for high frequency.

3.1.3 Image generation

Data analysis and image creation was performed in MATLAB (MathWorks) with the pixel size being half the transducer width. As in standard C-scan techniques, images based upon the amplitude of the received signal were made. The amplitudes were calculated by finding the maximum of the Hilbert transform of each waveform.

The waveforms each have the first 3 μs removed so the main bang, or the initial generating pulse, of the transducer is not read. Each signal had a mean that was slightly nonzero which corresponded to the DC offset. This value was removed so that the signal would be centred about zero and the amplitudes were measured accordingly. The amplitudes then correspond to each pixel. Contrary to standard imaging methods which often use more processing, including logarithmic compression of the waveforms and filtering of the final image, the images presented here are left unprocessed for use as a baseline of comparison.

The next technique uses the peak density as described by Doyle et al. (2011) for image reconstruction. This analysis is a measure of the number of peaks present in the resultant waveform's power spectrum. To generate the power spectrum, first a fast Fourier transform (FFT) was performed on each waveform. As done previously with the amplitude measurements, the first 3 μs were removed before transforming. The power spectrum is then the resulting magnitude of the FFT. From the power spectrum the number of peaks within a given frequency band can be calculated.

This work uses a different algorithm to count the peaks than in the work by Doyle et al [73]. In their work the peaks are counted within the 20-80 MHz band using a common technique where the number of times the derivative of the waveform crosses the zero axis is recorded. We found that this method was susceptible to noise and every extremum was counted. The algorithm used here detects peaks according to a user-defined threshold. Essentially, a peak is to be counted if it differs from the surrounding data by the value of the threshold. A flow chart of this algorithm is given in Figure 19. It is noted that while the algorithm finds the minima (valleys), we only count the maxima (peaks). We also did not limit the analysis to only the peaks in the 20-80 MHz band.

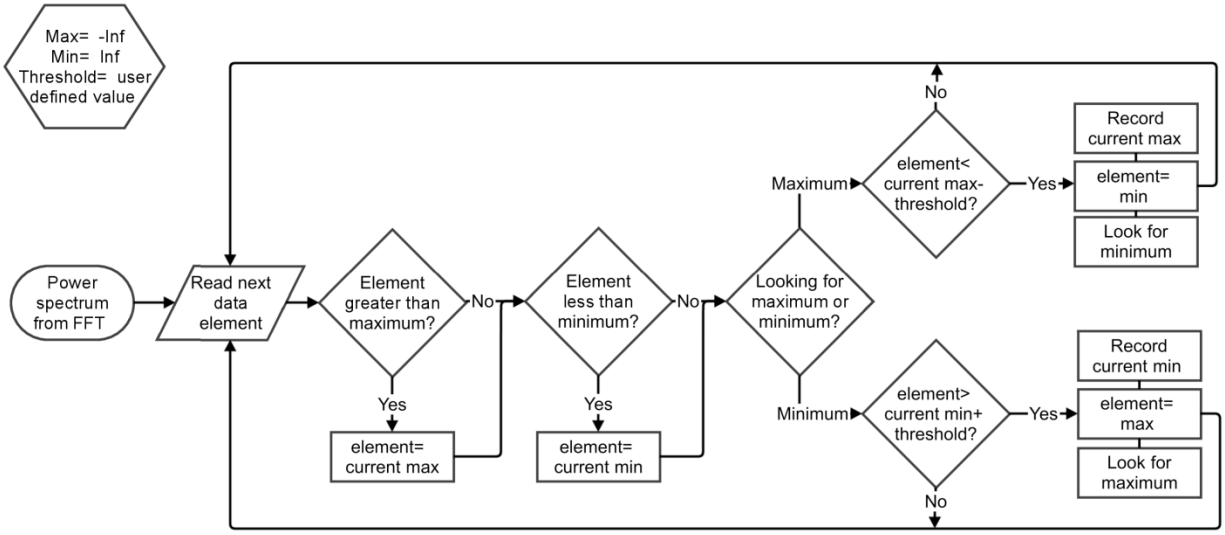

Figure 19. Flow chart representation of the peak counter used in our analysis

This threshold value allows the user to change which peaks are chosen according to their relative height. An example of how the threshold value changes which peaks are counted is shown in Figure 20. As the threshold value increases, only the larger peaks are counted. The threshold value is increased from 0.25×10^{-5} to 1.0×10^{-5} across the three graphs. This causes the number of peaks to decrease from 16 to 6.

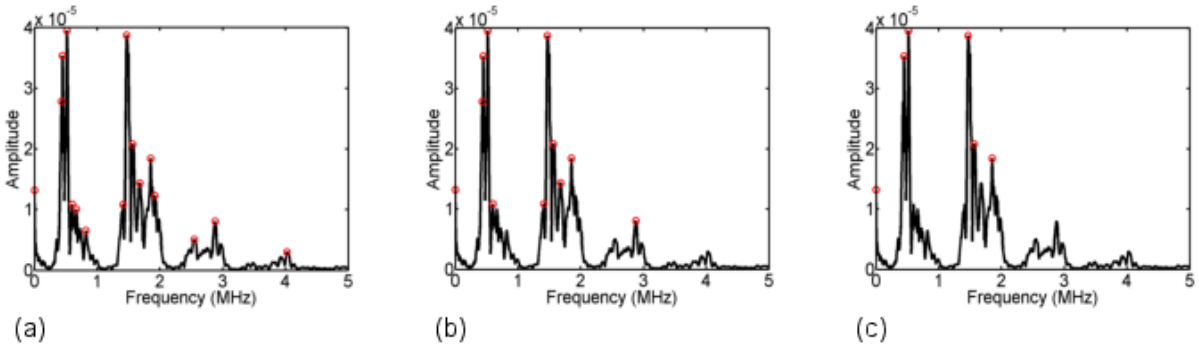

Figure 20. Power spectrum of sample measurement with 0.5 MHz transducers. The peaks are identified by circles and were calculated according to different threshold values: 2.5×10^{-6} (a), 5×10^{-6}(b), and 1×10^{-5}(c). The number of peaks changes with each threshold and are: 16 (a), 11 (b), and 6 (c).

Another parameter was also investigated in this study which was the energy of the waveform in the frequency domain. This parameter was calculated by finding the area under the power spectrum between two frequencies f_1 and f_2. For the low frequency transducers: f_1=0 MHz, f_2=5 MHz and for the high frequency transducers: f_1=0 MHz, f_2=80 MHz.

3.2 Results

Images were created based upon the methods previously described. Figure 21 shows the images for phantom 1. Amplitude images have dark regions where the transmitted waveform amplitude is low. The darker regions correspond to a lower number of peaks and lower calculated energy for the peak density and energy images respectively. Each image is normalized according to the maximum measured value of each parameter.

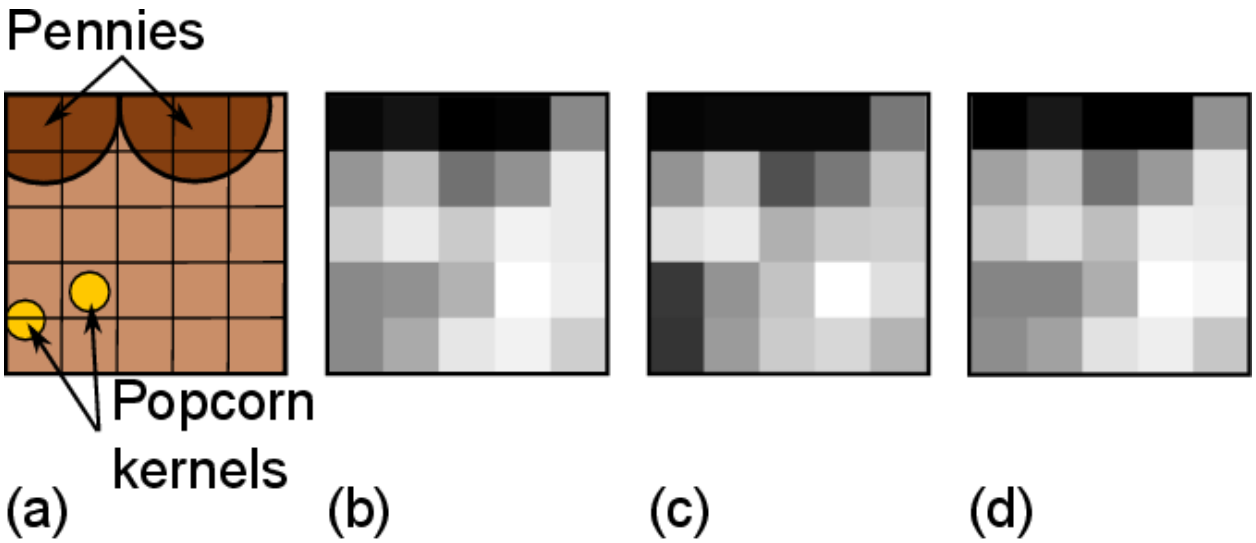

Figure 21. Reconstructed images for phantom 1: amplitude (b), peak density 0-5 MHz (c), energy 0-5 MHz (d). A schematic of the phantom's layout is given in (a).

Three images generated using each described technique are given in Figure 21. These images are small, containing 25 pixels and cover an area of 12.12 cm^2. It is seen that pennies are observable in each image, although the resolution is not high due to the size and frequency of the transducers used. The popcorn kernels are most visible in the peak density image.

The size of the images was expanded for phantom 2. An area of 24.5 cm^2 is shown by 50 pixels. These images are shown inFigure 22. The aluminium inclusion appears in each image, although the edge is not as clearly defined in the peak density image (c). The penny is also visible in each as well. It is noted that one of the small inclusions appears as a darker pixel in the peak density image than in the others.

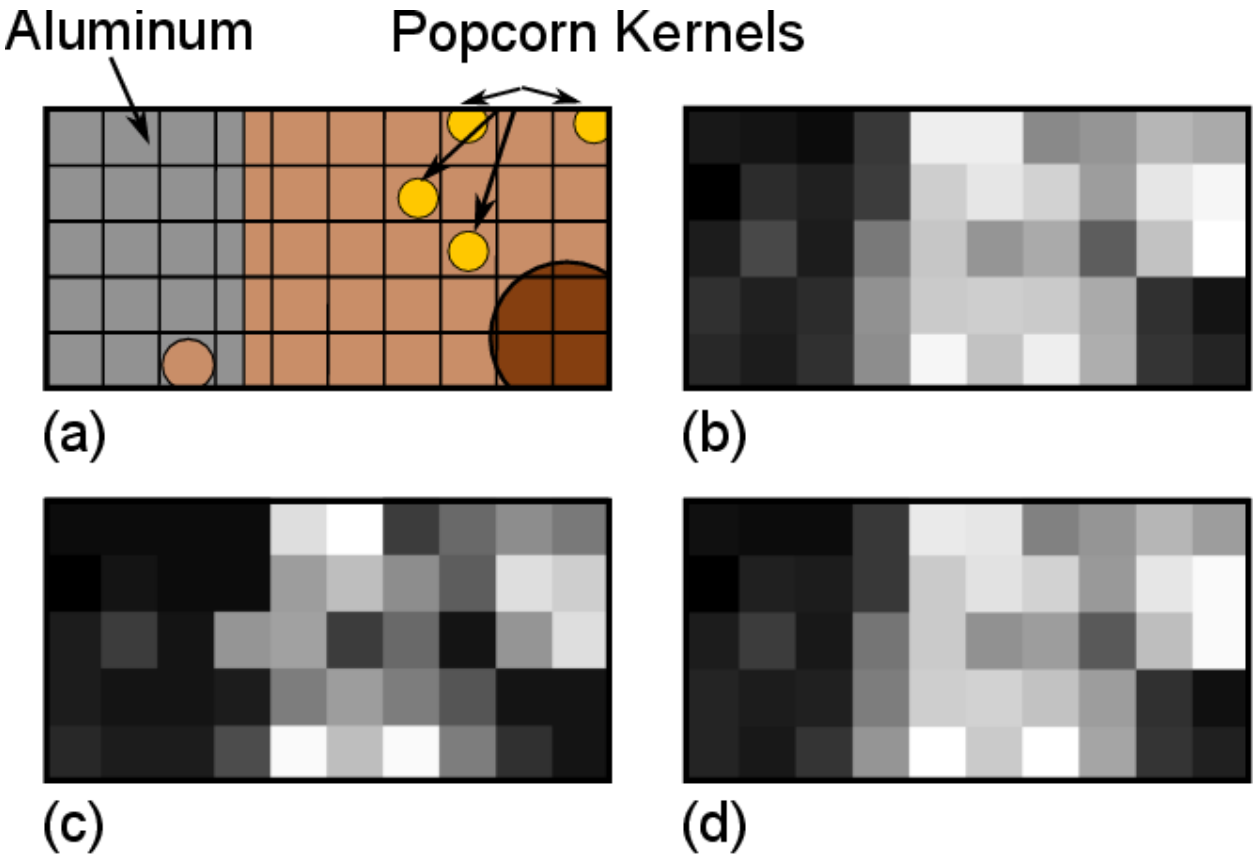

Figure 22. Images for phantom 2: amplitude (b), peak density 0-5 MHz (c), energy 0-80 MHz (d). The phantom's layout is described in (a).

Figure 23 shows the images constructed for phantom 3 using the high frequency transducers. The size of the high frequency transducers allowed for a smaller imaging area to be viewed by a larger number of pixels. Each image has 100 pixels covering a region of 1.03 cm^2. The increased resolution allows the small pepper seed to be discernible in each image. The peak density image shows the seed with the greatest contrast and with smaller size compared to the amplitude and energy images. A pepper flake is visible in the bottom left of each image. The pepper flake present in the bottom right corner of the phantom causes a slightly darker region in the amplitude and energy images. However, the prior knowledge of its location is what makes this inclusion visible.

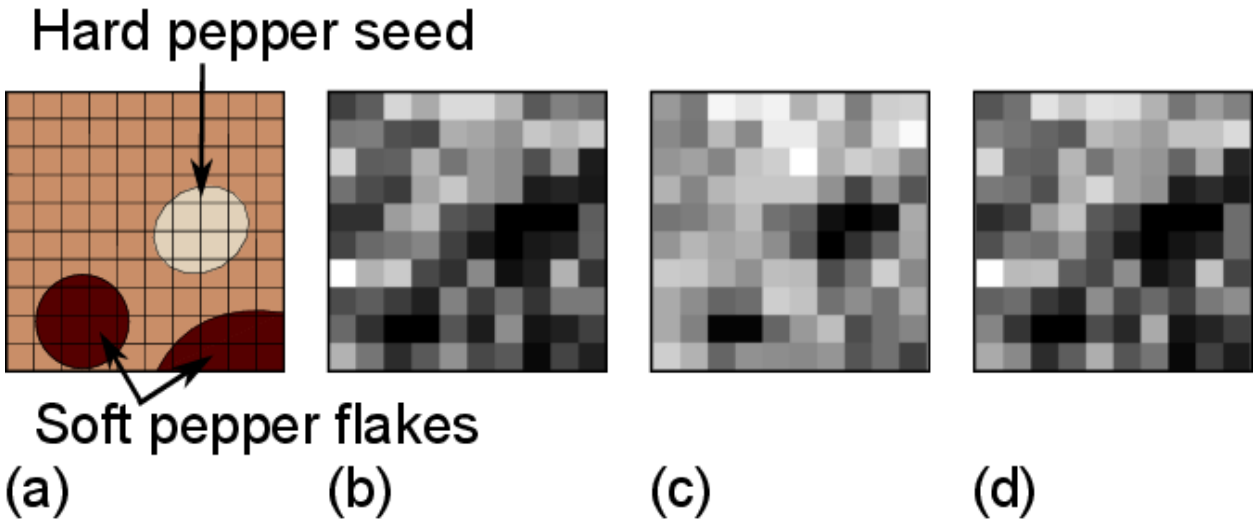

Figure 23. Images created for phantom 3: amplitude (b), peak density 0-80 MHz (c), energy 0-80 MHz (d). An image taken of the phantom is shown in (a).

3.3 Discussion

The images created with each technique display the major components in each phantom. As seen in Fig. 5, the pennies appear as a dark band in each image. Beneath the dark band, the

transducers overlapped both the pennies and the phantom. This illustrates the boundary, but due to the low resolution it is not shown in fine detail. The popcorn kernels are slightly visible in the amplitude and energy images but only with the foreknowledge of their location. The kernels are more apparent in the peak density image but do not accurately depict their size or exact location. Each kernel is approximately 5-7 mm in diameter which is smaller than the typical resolution for the transducers used. This likely explains why the kernels are not accurately portrayed in any of the reconstructed images.

The larger images created for phantom 2 are similar to those of phantom 1. As before, the penny is easily visible in each different imaging technique, and the contrast is best in the amplitude and energy images. A popcorn kernel is visible in the peak density image as a dark pixel, and appears darker in the other images as well. In each image, there are bands which look to be representative of the other popcorn kernels, although with low resolution. The aluminium slab is discernible in each image. It is seen that the peak density image shows the inclusions as well and perhaps slightly better than the amplitude image. The energy based approach looks to be nearly identical to the amplitude image.

The images created earlier served as a preliminary assessment whether other techniques are comparable to typical C-scan ultrasound. While they served to show that each method is comparable, the low resolution made assessing the quality difficult. This study aimed to evaluate high frequency ultrasound for its increased resolution in addition to sensitivity to microstructure [78]. The images shown in Figure 23 use the higher frequency transducers and examine a much smaller area.

The three inclusions in phantom 3 are seen in Figure 23(a). The pepper seed is approximately an ellipse with a major axis of 3.5 mm and minor axis of 3 mm and is set at an angle. The pepper seed is obvious in each image, but its size is overestimated in the amplitude and energy images. The seed should be approximately three pixels and is best represented in the peak density image. The soft flake in the bottom is evident, but its extent is not properly shown. The flake is not a hard scatterer and each imaging method has difficulty visualizing the edge. The peak density image gives the best contrast of the middle of the flake with the surrounding phantom.

The algorithm presented here regulates which peaks are counted according to a user-defined threshold. This value adjusts the number of peaks counted and changes the detail of the image. This is illustrated inFigure 24 and Figure 25. In Figure 24 peak density images are given for phantom 1 with varying threshold values. As the threshold value is increased fewer peaks are counted. Lower values give high contrast but do not detect edges and details. Higher thresholds give less contrast and capture more of the inclusions. Figure 24(c) most readily shows the inclusions, but due to the resolution it overemphasizes the extent. The small number of pixels makes this difficult to see, but this effect is more easily realized in Figure 25which shows images made using the 25 MHz transducers. By increasing the threshold, more of the soft flake in the lower left is visible than before.

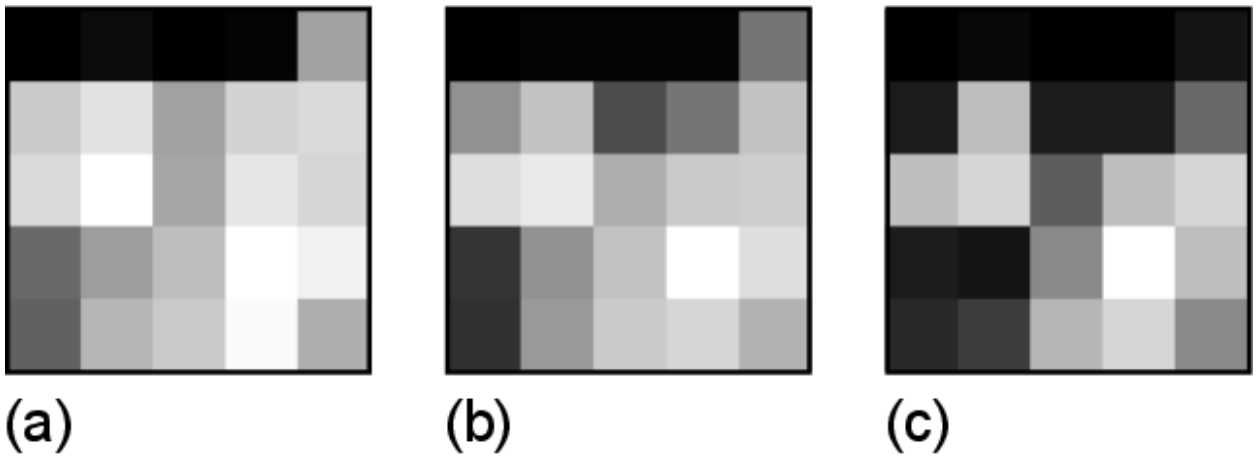

Figure 24. Images produced for phantom 1 using different thresholds for peak counting from 0-5 MHz: 5×10^{-6}(a), 1×10^{-5} (b), 2×10^{-5} (c).

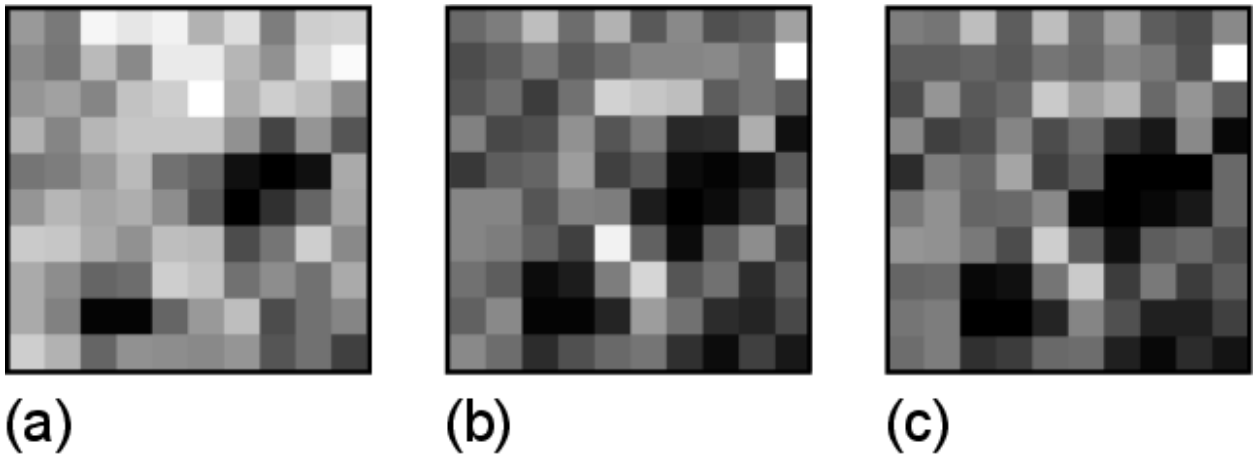

Figure 25. Images created of phantom 3 using different parameters for peak counting: threshold = $15 \times 10\text{\^{}} - 7$, 0-80 MHz (a); threshold = 50×10^{-7}, 0-80 MHz (b); threshold = 50×10^{-7}, 20-80 MHz (c).

Currently, there is no established optimal value for the peak counting threshold. This likely will change depending on the desired image outputs whether high contrast is desired or fine edges need to be viewed. Future embodiments could allow for the user to change the threshold value in real time similar to the signal gain in typical ultrasound devices.

Fig. 9 also shows how changing the frequency band affects imaging. This technique could possibly be extended to characterization based upon particular frequency bands. However, more work would be needed to establish these metrics.

Not surprisingly, the images based upon the energy are nearly identical to the amplitude images. This is likely due to the fact that the majority of the pulse strength was located between the frequencies used in the calculations. Thus, if the waveform had low amplitude in the time domain it directly related to low energy in the frequency band used. These computations may be more fruitful if a smaller frequency band could be found that correlated to pathology.

The images generated here were created without additional processing of the waveform data other than the calculation of the parameters. Typical ultrasound imaging methods utilize different algorithms to process the waveforms and improve the amplitude measurements. The images are often filtered as well to improve the quality. Similar processing procedures could likely be extended to peak density imaging as well.

In this research, the entire transmitted waveforms were analyzed, so the effect of the resulting echoes could be included. Rather than analyzing the longer-term response of the full waveform, further investigation could discover the effects of measuring the initial received pulse. The constructed motion stage also allows for standard pulse-echo measurements to be taken. Future work could possibly adapt these analyses to more traditional B-scan methods.

3.4 Conclusion

Ultimately, through the use of tissue-mimicking phantoms images were reconstructed based upon non-conventional parameters in addition to standard amplitude C-scan techniques. Images measuring the frequency dependent energy of the waveforms gave results analogous to amplitude-based images. Peak density images better indicated the presence of inclusions compared to amplitude based images in each phantom. The size of each inclusion was often more accurately represented as well. Spectral energy methods were found to show no improvement to amplitude measurements. This investigation demonstrates the potential of using peak density imaging as an additional tool for imaging materials and tissues.

Chapter 4.
Optimization and standardization of peak density measurements

The previous experiments conducted demonstrated the feasibility of the peak density measurement for material analysis and imaging. However, it was also found that the specific signal processing methods used greatly influenced the resulting value of peak density. Here we discuss the improvements that were made to the peak density measurement. This chapter gives an overview of the relevant signal processing methods including pulse width selection, window functions and spectral calibration. Additionally, these methods are applied to experimental data to optimize the acquisition of peak density parameter. The effects of the methods are discussed for individual spectra and are also assessed on a large scale by assessing the image quality of a test sample. Portions of this chapter were submitted to the journal of *Mechanical Systems and Signal Processing*.

4.1 Experimental setup

4.1.1 Sample preparation

In order to carry out ultrasonic measurements in soft materials, a phantom was made with properties similar to that of tissue. The phantom material was created using gelatin (Knox) and psyllium fiber powder (Equate) [103]. Inclusions were added to give contrast to adjacent measurements and included a hard pepper seed and soft pepper flakes. The addition of the

inclusions allowed a more intuitive evaluation of the signal processing techniques by visualizing our resulting two-dimensional mappings of the phantom.

4.1.2 Ultrasonic acquisition

Ultrasonic measurements were taken using two high frequency pachymeters (TransducerWorks) operated in through-transmission mode. The transducers are small in diameter (2 mm) and are centered at 25 MHz. A typical non-attenuated pulse is shown in Figure 26a). The transducers were excited with a 50ns, 100V square pulse using a UTEX UT340 pulser-receiver, and the received signals were amplified by 20 dB. The signals were digitized at 1.25 GS/s using a Tektronix DPO3052 oscilloscope. Waveform acquisition was automated through the use of LabView. To facilitate two-dimensional mapping, a micrometer stage was constructed to position the sample as shown in Figure 16. The measurements were taken in 1mm steps and were carried out in a standard raster pattern.

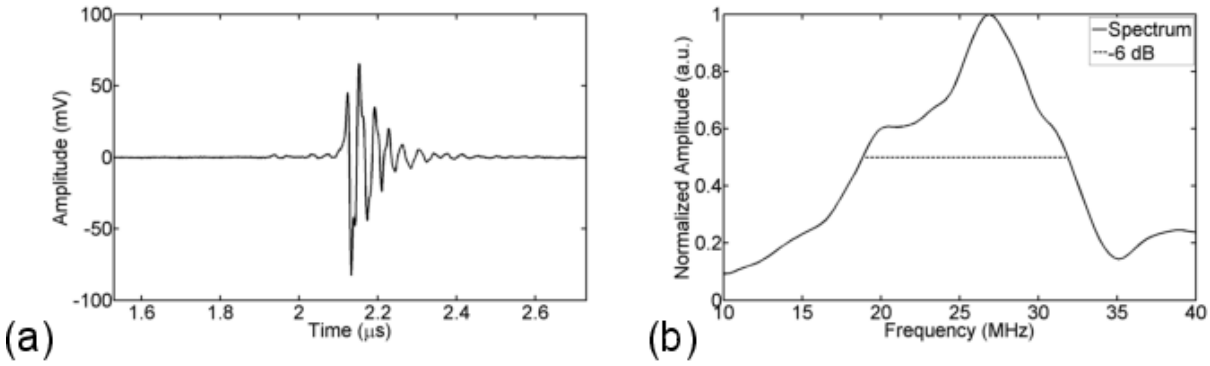

Figure 26. The ultrasonic pulse through a small amount of ultrasonic coupling gel in through-transmission mode (a). The normalized power spectrum for the received pulse (b). The standard -6 dB bandwidth is shown and corresponds to 18.6-32 MHz for a bandwidth of 52.5%.

4.2 Signal processing

4.2.1 Peak density

According to Doyle, the density of peaks or peak density, is defined as the number of resulting peaks and valleys in a waveform's power spectrum [78]. In their paper, the ultrasonic pulses were windowed, zero padded and then had a Fourier transform applied. The number of peaks and valleys was counted by determining the number of times the derivative of the power spectrum crossed the x axis within a given frequency band. Two separate bands were discussed which did not necessarily rely on the bandwidth of the transducer. Ultimately, a single band was chosen due to improved results.

In this paper, we follow a method similar to that of Doyle et al., and we examine several factors that could influence peak density measurements including the use of window functions, the selection of pulse width, and calibration. To obtain our measurements, the DC offset is removed, and the ultrasonic pulse is determined by selecting the portion of the waveform corresponding to a predetermined length centered about the maximum of the envelope found with a Hilbert transform. We investigated five different pulse widths: 0.4, 0.6 0.8, 1.0, and 1.2 μs. Once the pulse was found, it was multiplied by one of five different window functions. The waveforms were then zero padded to 4096 points to smooth the resulting spectra and improve computational efficiency. They then underwent a fast Fourier transform, and then the resulting power spectra were obtained. We limited our analysis of the peak density to within the -6 dB bandwidth of our transducer. Within this range, the peak density was found by counting the number of times the derivative of the frequency spectrum crosses the x axis.

4.2.2 Windowing

Fourier analysis often employs particular window functions to produce the desired frequency response according to the specific application. Certain windows improve amplitude measurement while others may improve frequency resolution between adjacent bins. A window function that allows for consistent peak counting would be ideal to maximize the quality of peak density assessment. We apply different window functions to our received waveforms to determine the effect on peak density measurement. In the following cases we treat the first received ultrasound pulse as the desired waveform. This region is selected, and the window functions are applied to this portion.

The most basic window function is the rectangular or boxcar window. A rectangular "window" is applied to the waveform over the desired region. This essentially selects out the chosen interval while leaving it unchanged. Zeroes are often appended to this section to increase computational speed and smooth the resulting spectrum. This interval along with the padded zeroes undergoes a Fourier transform to obtain the frequency response. The rectangular window is typically good at separating frequencies but may be inaccurate in determining their corresponding amplitudes. The resulting power spectrum with this window applied is shown in Figure 26(b).

Another common window used is the Hann window. It is defined as

$$w(n) = \frac{1}{2}\left(1 - cos\left(\frac{2\pi n}{N}\right)\right), 0 \leq n \leq N - 1. \quad (4.1)$$

The ultrasonic pulse is multiplied by this function. This serves to decrease the effects that can arise from non-periodicities toward the endpoints. The Hann function is one of the most used windows due to its versatility. The resulting windowed waveform is shown in Figure 27(a).

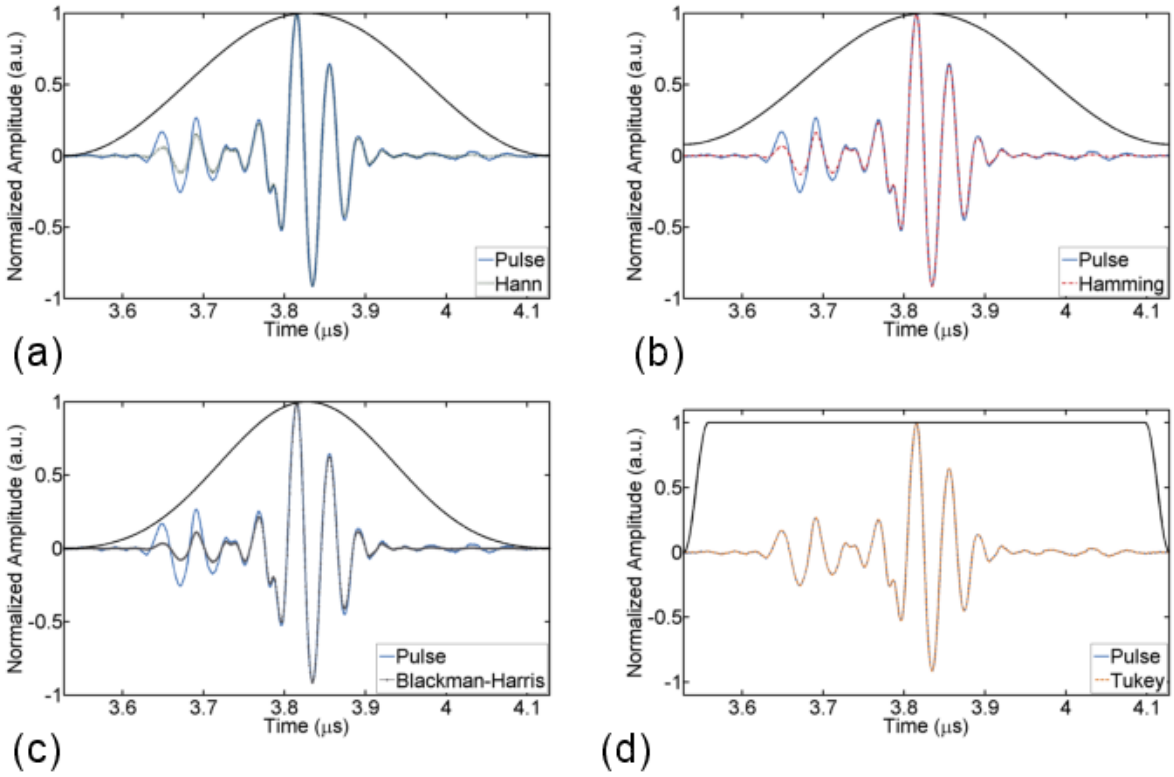

Figure 27. Representations of our windowed pulse for different window functions compared with the rectangular window: Hann (a), Hamming (b), Blackman-Harris (c), and Tukey (d). The corresponding window functions are shown as a solid, black curve above each pulse.

A window regularly used is the Hamming window. This function is similar to the Hann window except that it is nonzero at the endpoints. An example of this is shown in Figure 27(b), and the function is defined as

$$w(n) = 0.54 - 0.46\cos\left(\frac{2\pi n}{N}\right), 0 \leq n \leq N - 1. \quad (4.2)$$

The 4-term symmetric Blackman-Harris window is another general purpose window function. It is given as:

$$w(n) = a_0 - a_1 \cos\left(\frac{2\pi n}{N-1}\right) + a_2 \cos\left(\frac{4\pi n}{N-1}\right) - a_3 \cos\left(\frac{6\pi n}{N-1}\right), 0 \le n \le N-1 \quad (4.3)$$

where $a_0 = 0.35875, a_1 = 0.48829, a_2 = 0.14128$ and $a_3 = 0.01168$. This function is closely related to the Hamming window. The effects of applying this window are shown in Figure 27(c).

The last window we used is the Tukey window. It is less common than the previous windows, but it bridges the gap between the rectangular and Hann windows. This window has a flat top and unlike the previous window functions has an adjustable parameter, α. The Tukey window is

$$w(n) = \begin{cases} \frac{1}{2}\left[1 + \cos\left(\pi\left(\frac{2n}{\alpha(N-1)} - 1\right)\right)\right] & 0 \le n < \frac{\alpha(N-1)}{2} \\ 1 & \frac{\alpha(N-1)}{2} \le n < (N-1)\left(1 - \frac{\alpha}{2}\right) \\ \frac{1}{2}\left[1 + \cos\left(\pi\left(\frac{2n}{\alpha(N-1)} - \frac{2}{\alpha} + 1\right)\right)\right] & (N-1)\left(1 - \frac{\alpha}{2}\right) \le n \le (N-1) \end{cases} \quad (4.4)$$

By varying α this window shape and for particular values of α becomes the rectangular ($\alpha = 0$) and Hann ($\alpha = 1$) windows. In our work we use $\alpha = 0.1$, and Tukey windowing of our pulse is presented in Figure 27(d).

4.2.3 Calibration

Often in ultrasonic frequency-based measurements the power spectrum is calibrated by a reference spectrum to eliminate the systemic effects resulting from the transducers and equipment [35-38 45]. Since the majority of ultrasonic measurements are taken in pulse-echo mode, this reference spectrum is typically the pulse that is received from an echo off of a strong

reflector placed in the coupling medium. Our measurements are taken in through-transmission mode, and thus our reference spectrum is taken from the pulse transmitted through a small amount of acoustic coupling gel. This is the same spectrum as shown in Figure 26. The power spectrum is calibrated by dividing the measured spectrum by the reference spectrum point by point. In this work, we will also examine the consequences calibrating the spectrum has on determining peak density.

4.3 Results and discussion

4.3.1 Effects of windowing

Each window gives a different response in the frequency domain. The resulting power spectra for each are shown in Figure 28(a) for a strong signal that passed through a plain portion of a phantom. We see that for this waveform the application of different windows has minimal effect, and the peak density does not change. Windowing does begin affecting the frequency spectra for more moderate strength signals such as the pulse in Figure 28(b). In the power spectrum shown in Fig. 4(b) the Hann, Hamming and Blackman-Harris windows smooth the portion around 30 MHz. The peak densities in this case are: Rectangular 4, Tukey 3, Hann 2, Hamming 2, and Blackman-Harris 2.

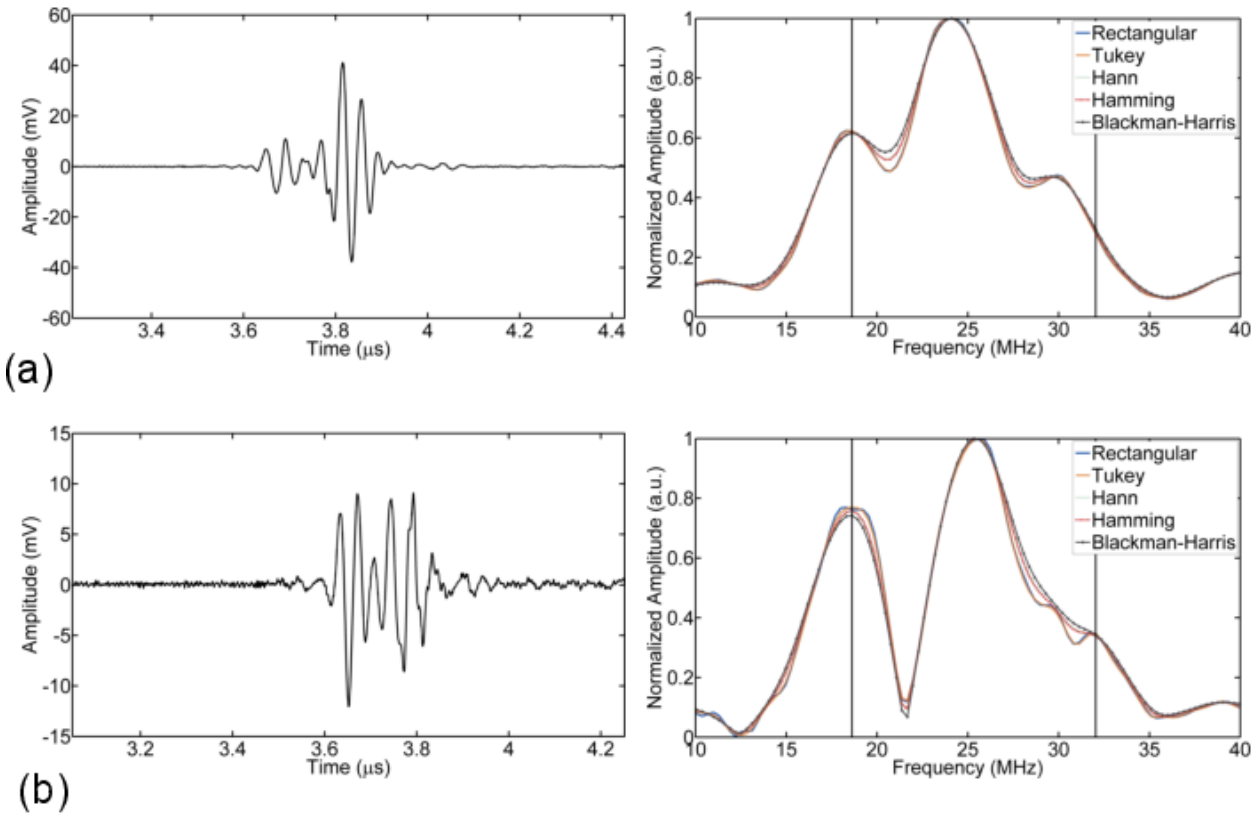

Figure 28. The normalized power spectra for each different window function for a strong pulse (a) and a moderate strength pulse (b). The vertical bars correspond to the bandwidth of the transducer and the range of frequencies of which the peak density was measured.

The image in Figure 29 shows the results for a weakly received signal. In this case, the ultrasound pulse was transmitted through our phantom material but encountered an inclusion, a hard pepper seed. This causes very little of the transmitted pulse to be received. For this measurement we see that the Hann, Hamming, and Blackman-Harris windows each preserve the greatest portion of the transmitting transducer's original frequency characteristics. Meanwhile, the rectangular and Tukey windows are much more scattered across the frequency bins. For this example, the peak density is: rectangular 16, Tukey 16, Hann 6, Hamming 6, and Blackman-Harris 6.

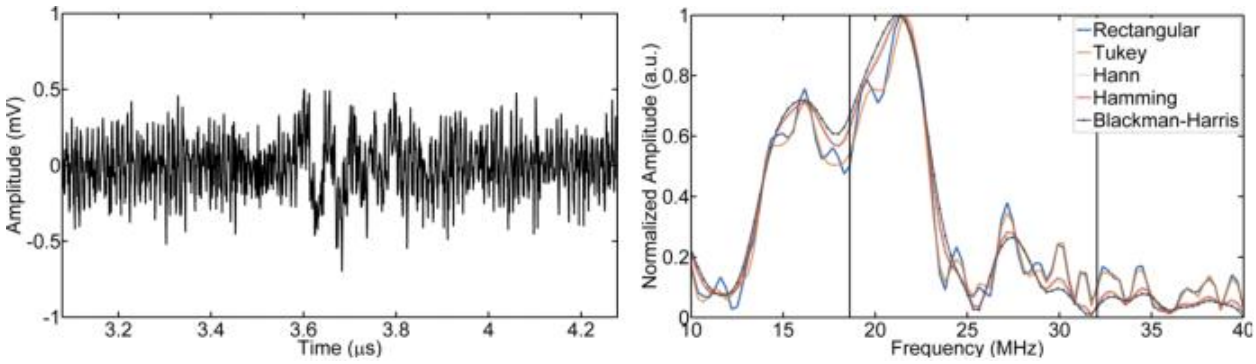

Figure 29. The normalized power spectra of a weak signal using each window function.

For peak density to be viable as an imaging and characterization method we would expect that that in the presence of an inclusion, the value would be significantly different than for ordinary phantom material. The Hann and Blackman-Harris windows peak density measurements for an inclusion are only different from clear phantom measurements by 2. This is hardly dissimilar enough to reasonably distinguish large differences in structure, let alone less significant changes. Overall, for our 100 hundred measurements the rectangular window had peak densities ranging from 2-19, the Tukey window ranged from 2-16, the Hann window gave 1-8, the Hamming window spanned 1-8, and the Blackman-Harris window had peak densities from 1-7. We have seen that the Hann, Hamming, and Blackman-Harris tend to smooth out the power spectra and capture the overall frequency distribution while ignoring small, abrupt changes. This suggests that these windows may not necessarily be suitable for peak density measurements.

4.3.2 Effects of pulse width

It was found that the length of the portion of the pulse selected from each waveform influenced peak density in about half of the measurements. To more closely examine the effect, several pulse widths were chosen. These were 0.4, 0.6, 0.8, 1.0, and 1.2 μs which correspond to 10, 15, 20, 25, and 30 wavelengths for 25 MHz transducer with a wave speed of approximately 1400 m/s. Figure 30 demonstrates the consequences of pulse width selection with rectangular windowing. An example of a scan unaffected by pulse width is shown in Figure 30(a) with four peaks found for each pulse width. For the A scan shown in Figure 30(b), lengthening the waveform changes the spectrum around 31 MHz and increases the peak density from two to three. A very weak signal is shown in Figure 30(c). Widening of the pulse causes a significantly larger number of peaks to be present. For the shortest pulse width only 4 peaks are counted and the peak density increases to 15 for the largest pulse width.

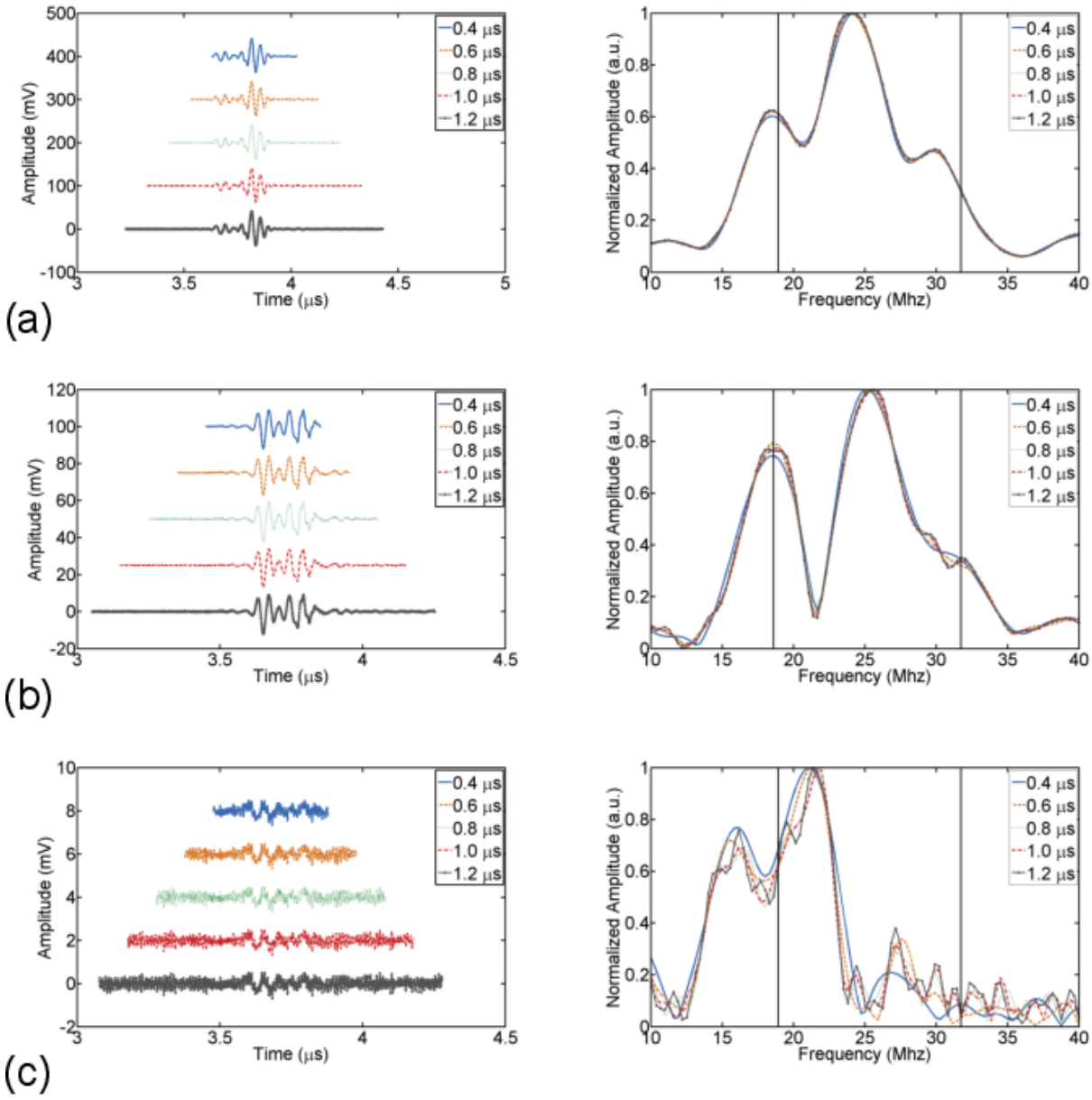

Figure 30. The resulting power spectra using different pulse widths and rectangular windowing.

For the 100 ultrasonic measurements it was seen that increasing the length of the selected pulse led to larger ranges for the peak density measurements. For the measurements with rectangular windowing, the shortest width of 0.4 μs had peak density range of 1-5. For the 0.6 μs width the peak density was 1-9, the 0.8 μs width ranged from 2-13, and the 1.0 μs gave 2-13 as

well. The longest pulse width of 1.2 μs had a range of peak densities from 2-18. Similar effects were also found for the other window functions for increased pulse widths. The larger range of peak densities found with longer pulse widths is more useful for detecting a greater span of material dissimilarities.

4.3.3 Effects of calibration

A few examples of the calibration spectra are shown in Figure 31for rectangular windowing of the 1.2 μs samples. For the 100 peak density measurements taken, 58 were left unchanged. For the rest of the measurements, the peak density typically differed by a value of one or two with only six measurements varying by more than two. The calibrated spectra for the same pulses as in Fig. 4 are shown in Figure 31(a) and (b) respectively. The peak density remains the same in Figure 31(a), and two additional peaks are gained with calibration in Figure 31(b). Figure 31(c) shows the most extreme instance where the calibration changes the value of the peak density. The spectrum is flattened considerably, and the peak density for the uncalibrated spectrum is 2 while the calibrated spectrum has a value of 6.

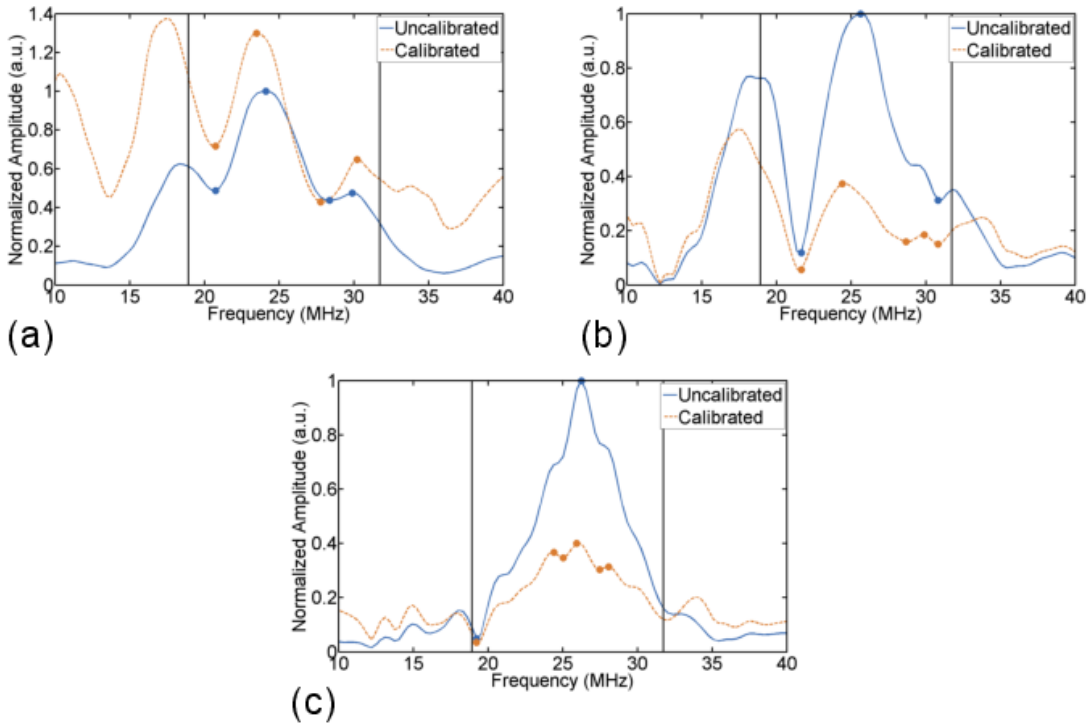

Figure 31. Comparison of calibrated and uncalibrated spectra for various ultrasonic measurements with rectangular windowing. The amplitude of the calibrated spectrum in (b) was increased by a factor of 20 for better visualization.

The peak densities found with calibrated spectra were largely comparable to that of the uncalibrated results. For the 1.2 μs pulse width and rectangular windowing the peak density spanned 3-18 while the uncalibrated peak densities ranged from 2-18. The results for the other windows and pulse lengths with calibration were analogous to their respective uncalibrated counterparts as well.

Figure 32 summarizes our results by presenting two dimensional images created for each measurement configuration. By inspecting the images, we easily see that peak density determinations are dependent upon the measurement procedure. For the shortest pulse width taken, the peak density value is unreliable; the pixel values are widely varied in these images,

and the internal structure is not apparent. As the pulse width increases, modest improvements are seen in the images. The use of different window functions has the largest impact on peak density. The Hann, Hamming, and Blackman-Harris windows cause the spectra to become too smooth and do not capture the small-scale frequency variations necessary to differentiate substantially dissimilar materials. However, at longer pulse widths these three windows do begin to suggest the presence of the inclusions. The rectangular and Tukey windows proved to be extremely similar. Apart from a few minor differences in certain individual pixels, the rectangular and Tukey windows give nearly identical images. The Tukey window may have an advantage over the rectangular window due to its adjustable parameter, α, but the effects of α were outside of the scope of this study. Calibrating the spectra had little impact on the resulting peak density images. A small increase in contrast between the inclusions and background were noticed, but the improvement was not necessarily significant.

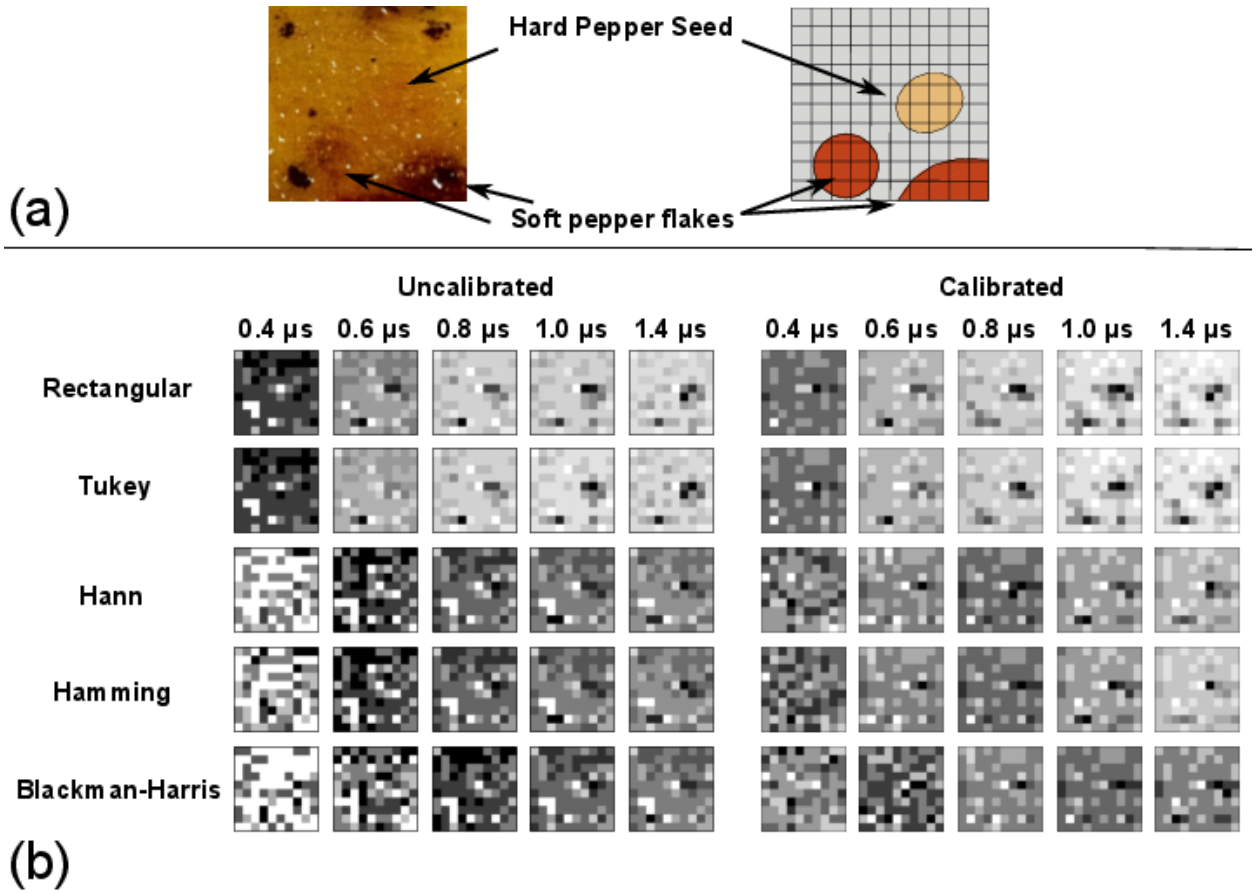

Figure 32. Photograph of the phantom and schematic of the internal structure (a). Two dimensional images for condition used in this study (b). Each picture is normalized by the maximum peak density for the appropriate sample set.

4.4 Conclusion

Peak density has previously been established as an ultrasonic measurement responsive to changes in tissue microstructure [73] Through the use of a tissue-like phantom material we investigated the outcomes of peak density measurements when commonly used signal processing techniques are considered and applied.

1. The selection of the pulse width plays a role in resulting peak density measurements. Small pulse widths of 10 wavelengths gave poor results while increasing pulse widths gave improved visualizations of the phantom material.
2. Windowing the pulses gave significantly different peak densities. Three windows, the Hann, Hamming, and Blackman-Harris did not give the appropriate frequency response necessary for counting peaks. The rectangular and Tukey windows were comparable with no large distinction between them. However, the rectangular window was found to produce a slightly larger range of peak density values.
3. Calibration of the waveforms demonstrated very little improvement in peak density measurements compared to the uncalibrated spectra. Calibration may prove useful for peak density measurements performed with different equipment, but that outcome was not studied here.

Chapter 5.
Development of systematic relationship between microstructure and measurement

The previously discussed work has demonstrated the feasibility peak density measurements by evaluating images of tissue-mimicking phantoms based on peak density. Peak density images have been shown to visualize internal structure at least as well as more conventional through-transmission techniques. The acquisition of peak density has also been optimized to give high quality, consistent measurements. However, these previous measurements have been largely concerned with larger-scale differences in the material structure. Ultimately, the goal of this dissertation is to relate the peak density measurement with microstructure and better understand the applicable physics. This chapter investigates the sensitivity of peak density to microstructure through systematic experimental and computational methods. The relevant theory is also discussed. A portion of the work in this chapter was submitted to the journal *Ultrasonics.*

5.1 Relevant scattering theory

As discussed in Chapter 2, for an elastic sphere we can express the scattered pressure in the far-field with wavenumber k and polar coordinates r and θ

$$p_{s,far} = \frac{e^{-ikr}}{r}\Phi(\theta), \tag{5.6}$$

$$\boldsymbol{\Phi(\theta) = \frac{-1}{k}\sum_{l=0}^{\infty}(2l + 1)(-i)^{l+1}\sin\eta_l\, e^{i\eta_l}\, P_l(\cos\theta)},\tag{5.7}$$

where the phase shift $\boldsymbol{\eta_l}$ is found from the application of the boundary conditions [89-93]. It was seen that the material properties of the scatterer affected the resulting field, and we plotted the angular distributions for various properties. From the angular distributions, it can be gleaned that the total magnitude of the scattered field changes as well. The amount of the total scattered field is known as the scattering cross-section, $\boldsymbol{\sigma_s}$. This value can be useful for different applications for when the amount of signal loss due to scattering is needed. It can be calculated as [89,105]

$$\sigma_s = 2\pi \int_0^{\pi} |\Phi(\theta)|^2 \sin d\theta.\tag{5.8}$$

We can then derive the scattering cross-section for the elastic sphere. First we consider the angular component from equation (5.7). We then have

$$\sigma_s = 2\pi \int_0^{\pi} \left|\frac{1}{k}\sum_{l=0}^{\infty}(2l+1)\,(-i)^{l+1}\sin\eta_l\, e^{i\eta_l}\, P_l(\cos\theta)\right|^2 \sin\theta d\theta,\tag{5.35}$$

$$\sigma_s = \frac{2\pi}{k^2} \int_0^{\pi} \sum_{l,m}(2l+1)\,(2\mathrm{m}+1)\sin\eta_l \sin\eta_m\, e^{i(\eta_l-\eta_m)}\, P_l(\cos\theta)\, P_m(\cos\theta)\sin\theta d\theta\tag{5.36}$$

$$\sigma_s = \frac{2\pi}{k^2}\sum_{l,m}(2l+1)\,(2\mathrm{m}+1)\sin\eta_l \sin\eta_m\, e^{i(\eta_l-\eta_m)} \int_0^{\pi} P_l(\cos\theta)P_m(\cos\theta)\sin\theta\, d\theta\tag{5.37}$$

We then use the orthogonality of the Legendre Polynomials 95

$$\int_0^{\pi} P_l(\cos\theta) P_m(\cos\theta) \sin\theta \, d\theta = \frac{2}{2l+1} \delta_{l,m} \tag{5.38}$$

where $\delta_{l,m}$ is the Dirac-delta function. This yields

$$\sigma_s = \frac{4\pi}{k^2} \sum_{l,m} (2m+1) \sin\eta_l \sin\eta_m e^{i(\eta_l - \eta_m)} \delta_{l,m} \tag{5.39}$$

This collapses the double summation, and we obtain

$$\sigma_s = \frac{4\pi}{k^2} \sum_{l=0}^{\infty} (2l+1) \sin^2\eta_l \tag{5.40}$$

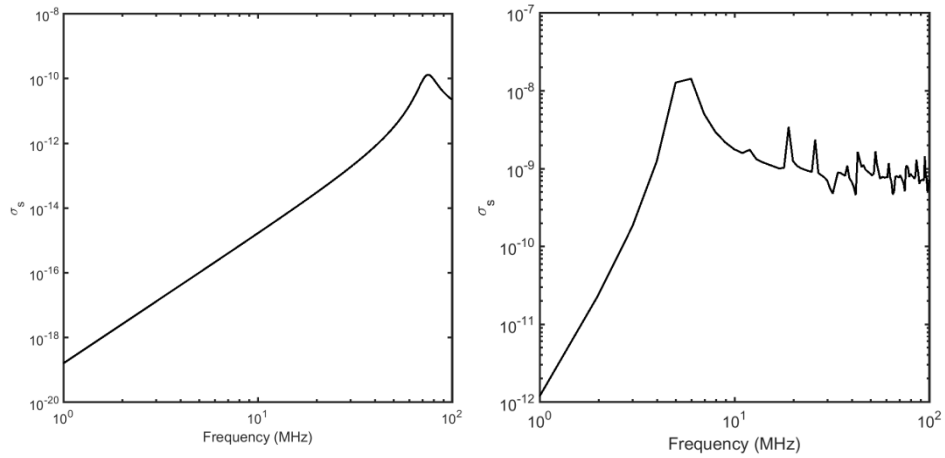

Figure 33. Scattering cross-sections for 5 µm and 69 µm diameter glass beads in water.

Figure 33 shows the scattering cross-sections for 5 µm and 69 µm diameter glass beads immersed in water. We see the Rayleigh regime as well as the transition to more complicated scattering. We see that the cross-section is reliant on the size of the scatterer since the plots are shifted due to the relation of the wavelength to scatterer size. Also noted is the presence of resonances due to the material properties of the scatterer.

Let us next consider N identical scatterers. Assuming no multiple scattering, it is reasonable to take the scattering cross-section of all of the scatterers to be

$$\sigma_{s,N} = N\sigma_s \tag{5.9}$$

For our peak density measurements, we conduct measurements over a frequency band. Let us now take into account the scattering cross-section across multiple frequencies. We define $\sigma_s(k) = \sigma_s$ at a given frequency. Then for a given scatterer, the total scattering cross-section across the frequency band is given by

$$\sigma_{sk} = \sum_k \sigma_s(k) \tag{5.10}$$

From (5.9) and (5.10) it follows that the total scattering cross-section for N identical spheres across a given frequency band is

$$\sigma_{s,total} = N \sum_k \sigma_s(k) = N\sigma_{sk} \tag{5.11}$$

Let us now look at what happens when we calculate $\sigma_{s,total}$ for various diameters and numbers of glass scatterers from the 1-200 MHz band. The calculated cross-sections are shown in Figure 34. We see that the cross-section is highly-dependent on both the diameter and the number of scatterers.

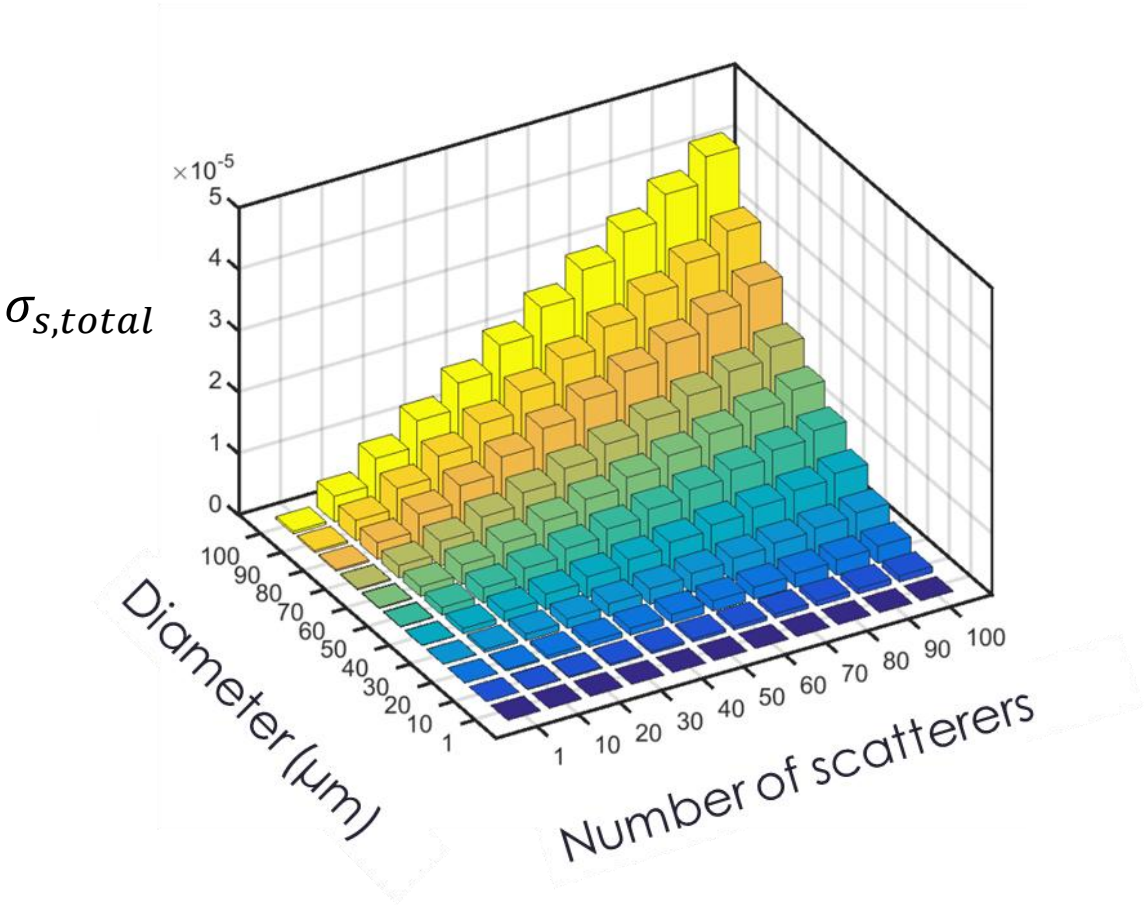

Figure 34. Bar plot of $\sigma_{s,total}$ for assorted numbers and diameters of glass beads.

Now that we have better understand of the total scattering present in a system of identical scatterers, we will next study the results of peak density measurements for glass bead scatterers of different diameters and number densities through experimental as well as computational means.

5.2 Experiment

5.2.1 Sample preparation

Ultrasonic measurements were carried out with the use of tissue-mimicking phantom with soda-lime glass microspheres acting as scatterers. The phantoms were prepared using water and gelatin in a manner similar to Bude [103]. However, in this study the psyllium fiber powder used in Bude was omitted. The base water-gelatin mixture was a 12.5:1 ratio of water to gelatin. Phantoms were formed into 3.2 mm tall and 40 mm wide cylinders. Glass microspheres of different nominal diameters were added to the gelatin mixture in varying concentrations and mixed. The mean sphere diameters used were 5, 9 34, 69 μm. Exact distributions of the spheres are shown in Table 2.

Table 2. Distributions of the glass microsspheres used in this study.

Mean Diameter (μm)	Lower limit (μm)	Upper limit (μm)	Product ID
5		8	P2011SL
9	4	15	P2015SL
34	20	55	P2050SL
69	48	83	P2075SL

Each phantom contained a different number density of microspheres. The five concentrations used in this study were: 1, 25, 50, 75, and 100 mm^{-3}. Through-transmission optical microscopy was used to image the phantoms to ensure the proper sizes and concentrations of the glass microspheres. An optical microscope along with a digital camera was used for the imaging. Images of select phantoms are shown in the following figure.

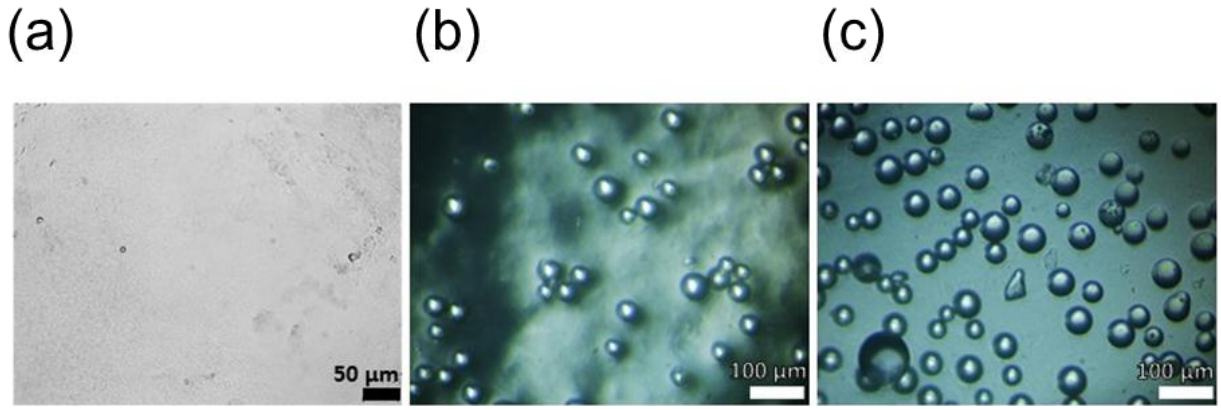

Figure 35. Photographs of phantoms used in this study: 9 µm size microspheres with 1 mm^{-3} density (a); 34 µm size microspheres with 25 mm^{-3} density (b); and 69 µm size microspheres with 50 mm^{-3} density (c).

5.2.2 Experimental Setup

The ultrasound setup in this study used two small-diameter, single-element, high-frequency transducers operated in a through-transmission configuration. Each transducer had a center frequency of 31.5 MHz. Figure 36 shows the through-transmission response of the transducers when separated by a small amount of coupling gel. The -6 dB bandwidth of the transducers is in the 22-41 MHz range.

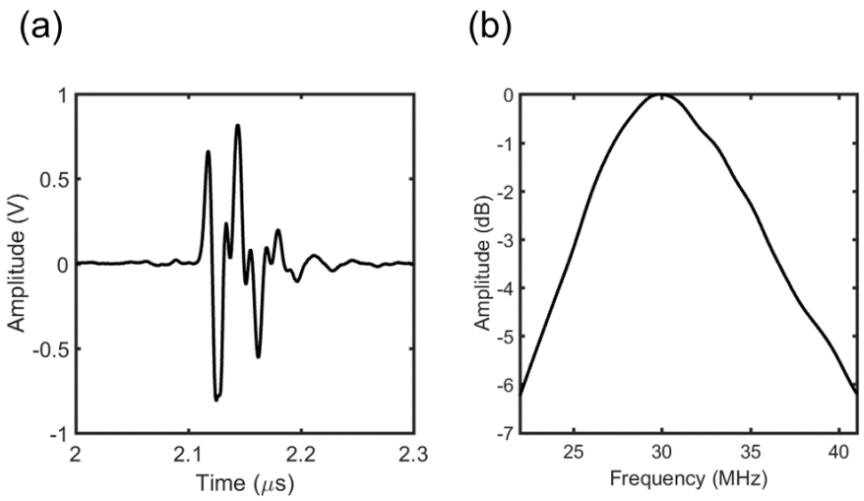

Figure 36. The pulse received through a small amount of coupling gel (a). The resulting frequency spectrum(b). This was the calibration spectrum used in our experiments. The bandwidth of the transducer is 22-41 MHz.

The transducers were excited by a 100 V, 5 ns square wave pulse by a high-frequency pulser-receiver. Received pulses were digitized at 1.25 GS/s using a digital storage oscilloscope. The transducers were mounted on a homemade, automated 3-axis control stage and interfaced with LabView. Measurements were taken at 1 mm steps, and the samples were scanned in a standard raster pattern for 100 steps. To ensure sufficient contact between the transducers and the sample, ultrasonic gel was amply used and carefully monitored.

5.2.3 Parameter calculation

Here we describe the calculation of the peak density parameter. In order to minimize local variations, each sample was scanned at 100 separate locations. The received waveforms were loaded into Matlab for analysis. Each pulse was windowed by selecting 1500 points about the maximum of the pulse which was found using a Hilbert transform. A Tukey window with an adjustment parameter $\alpha = 0.1$ was then applied to the pulse. This was performed to eliminate any

edge effects introduced by the finite windowing of the original rectangular window. The power spectrum for each pulse was then determined. To negate the specific frequency effects introduced by the experimental setup, the measured power spectrum was divided by a reference spectrum. The reference spectrum was found by measuring the signal received through a very small amount of coupling gel. This is the same spectrum as shown in Figure 36.

The peak density is defined as the number of local maxima and minima present in the spectrum. This value was determined by calculating the numerical derivative of the normalized spectrum. The number of times the derivative crosses the x axis then denotes the peak density. Process flow for this calculation can be found in Figure 37. The peak density was calculated for each individual scan point. The measured peak density for each phantom was then the average of the peak density of the individual scan lines.

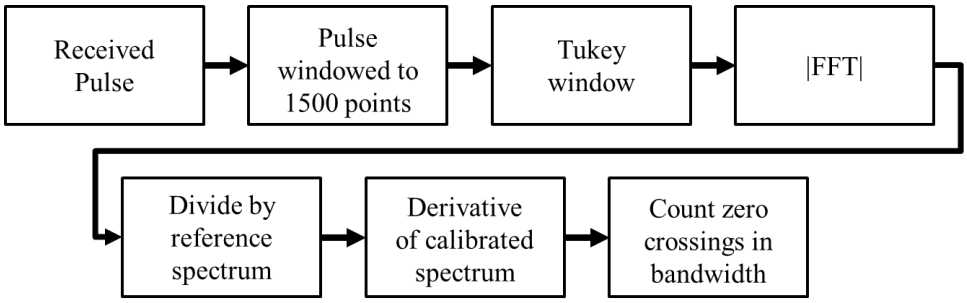

Figure 37. Flow chart for the experimental determination of peak density.

5.3. Finite element analysis (FEA) simulation

5.3.1 Theory

Comsol Multiphysics v5.1 software was used to carry out the finite element simulations in this study. This software was chosen due to its ability to couple various types of physical Partial

Differential Equations (PDEs), in this case, acoustics and solid mechanics. Moreover, while other numerical methods for studying acoustic systems may exist, commercial finite element analysis software was chosen for its robust computational ability and its reproducibility among different researchers.

In the fluid region, Comsol solves the 2D Helmholtz equation

$$\nabla \cdot \left(-\frac{1}{\rho_c}(\nabla p_t - \boldsymbol{q}_d) \right) - \frac{k_{eq}^2}{\rho_c} p_t = Q_m \tag{5.43}$$

where the equivalent wave number k_{eq} is defined for frequency f and the fluid sound speed c_c as

$$k_{eq}^2 = \frac{(2\pi f)^2}{c_c^2} - k_z^2 = k^2 - k_z^2. \tag{5.44}$$

The out-of-plane wave number k_z is set to zero in our models. Q_m and $\boldsymbol{q}_d$ correspond to monopole and dipole source terms. These terms are both zero in our system. The total pressure, p_t, is defined as the sum of the background pressure field and the scattered field: $p_t = p_b + p_s$. The background pressure field in our models is a plane wave propagating in the $\widehat{e_x}$ direction and is given by $p_b = p_0 e^{-kx}$. Compiling these simplifications and using a constant fluid density, ρ_c the equation becomes

$$\nabla^2 p_t + k^2 p_t = 0. \tag{5.45}$$

In order to fully capture the effects created by having elastic scatterers, the two-dimensional Navier's equation of motion is also solved for the solid scatterers. The microspheres are modeled as an isotropic, linear elastic material. The governing equation is then

$$-(2\pi f)^2 \rho_s \boldsymbol{u} = \nabla \cdot S + F e^{i\phi}, \tag{5.46}$$

where f is the frequency, ρ_s is the density of the solid, S is the Cauchy stress tensor, F is the force acting on the solid, and ϕ is the phase component of the force. The displacement field of the solid is given by $\boldsymbol{u}$.

At the boundary of the fluid and the solid interface, the PDEs for the fluid acoustics and solid mechanics are coupled with the following boundary conditions

$$\boldsymbol{n} \cdot \left(\frac{1}{\rho_c} \nabla p_t\right) = -\boldsymbol{n} \cdot \boldsymbol{u}_{tt}, \tag{5.47}$$

$$\boldsymbol{F_A} = p_t \boldsymbol{n} \tag{5.48}$$

where $\boldsymbol{n}$ denotes the unit vector normal to the boundary, $\boldsymbol{u_{tt}}$ is the structural acceleration, and $\boldsymbol{F_A}$is the load acting on the solid structure.

5.3.2 Model setup

The model is arranged into two simulation domains- fluid and solid. A schematic of the model geometry is shown in Figure 38. In addition, we make use of a perfectly matched layer (PML) surrounding the fluid domain. This layer mimics a non-reflecting boundary condition and allows any outgoing waves to leave the model domain without any reflection. A dense mesh was used to ensure proper resolution for the propagating waves, and the maximum element size was $\lambda/8$, where λ denotes the wavelength of the signal traveling through the medium.

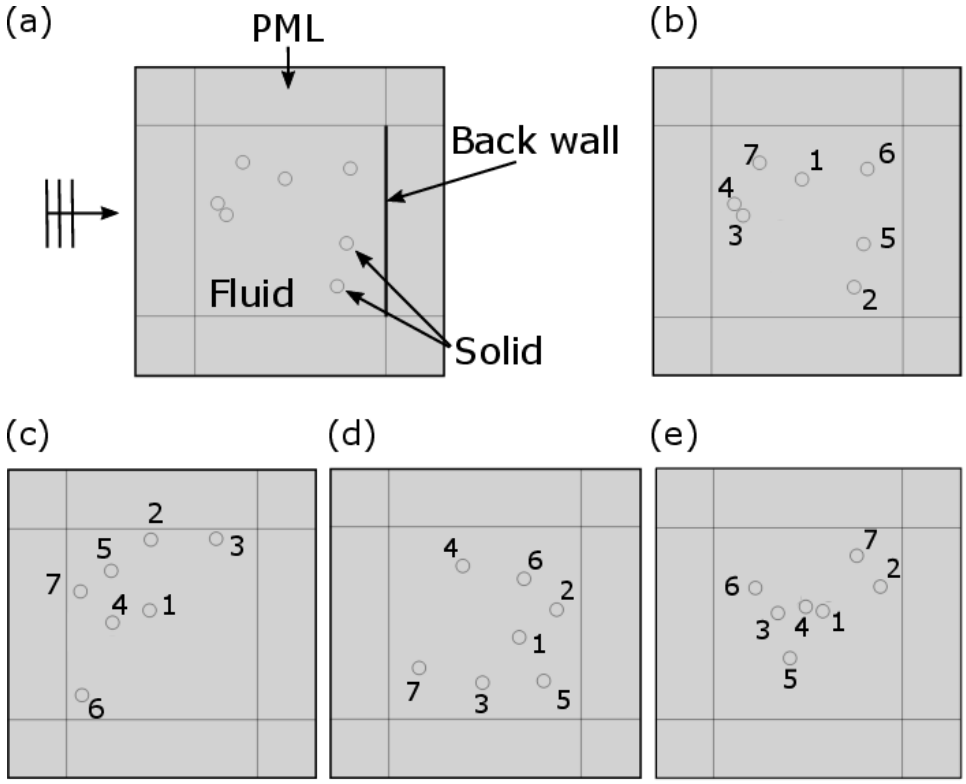

Figure 38. Geometry used in the finite element model. Modeling domains are shown in (a). The four sets of randomly distributed microspheres are given in (b)-(e). The number denoteswhen the scatterer was added to the modeling domain, i.e., scatter five was added for the five scatterer simulation and was used for the seven and 10 scatterer simulation as well.

In order to study the scattering due to different densities of scatterers the simulations are conducted with different numbers of randomly distributed scatterers using the same diameters as the microspheres in the experiment. The simulations are repeated for four different distributions. The positions of each scatterer were randomly generated and were repeated for each diameter. The number of scatters used in the simulation was determined by calculating the expected number of spheres present in a thin layer of the experimental phantom. A layer with an area of 1 mm^2 and a height of 69 μm was used as well as the experimental number densities. The resulting number of scatterers used was 1, 2, 3, 5, and 7.

Table 3. Input parameters for FEA simulation.

Model parameters fluid	Input value
Density ρ_c	1 g/cm^3
Sound speed c_c	1540 m/s
Model parameters solid	**Input value**
Density ρ_s	2.5 g/cm^3
Poisson ratio ν	0.22
Young's Modulus E_Y	68 GPa
Sound speed c_s	5570 m/s

5.3.3 Parameter estimation

To simulate the resulting experimental power spectra the simulation is repeated, and the Helmholtz equation is solved for each different k. In order to detect small changes in the resulting scattered pressure field for each frequency, the frequency was incremented in steps of 200 kHz and spanned the bandwidth of the transducer from 22-41 MHz. Since we are interested in all of the forward scattering, the scattered pressure field is determined on the back wall (Figure 38) of the fluid modeling domain to obtain the overall forward response. After the simulation has been conducted for each wavenumber the results are compiled into a model frequency spectrum. The derivative of the model spectrum is calculated, and the number of x axis zero crossings are counted to calculate the simulated peak density. The values are then averaged for each trial distribution. This process is illustrated in Figure 39.

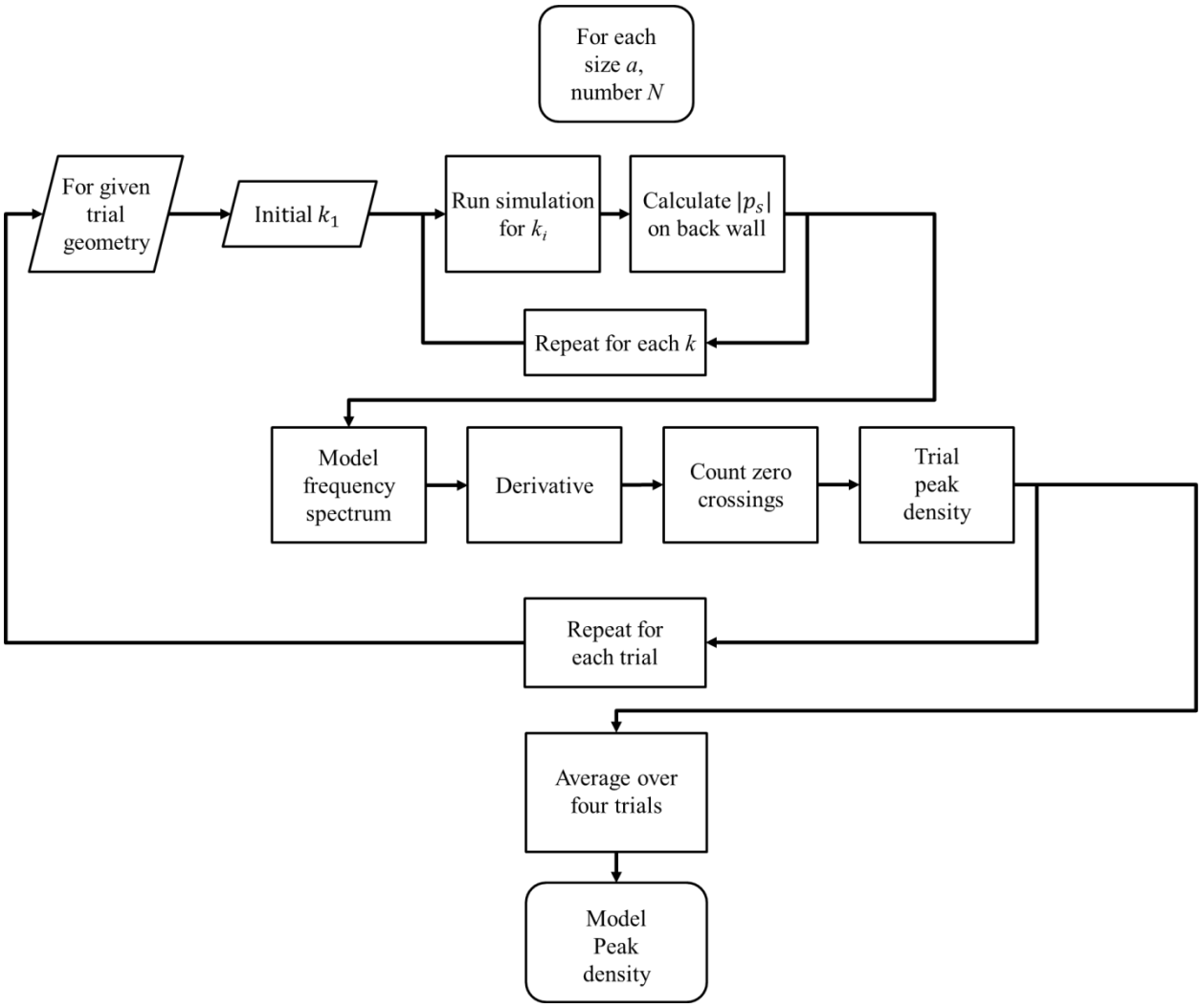

Figure 39. Flow chart for determination of simulated peak density.

5.4 Results and Discussion

The finite element model allows us to easily visualize the scattering caused by the different numbers of assorted sized scatterers. As postulated before, the total scattering tends to increase diameter and number. By inspecting Figure 42, which shows the magnitude of the scattered field for the two and five scatterer cases at the various sizes, we see that this is indeed is the case.

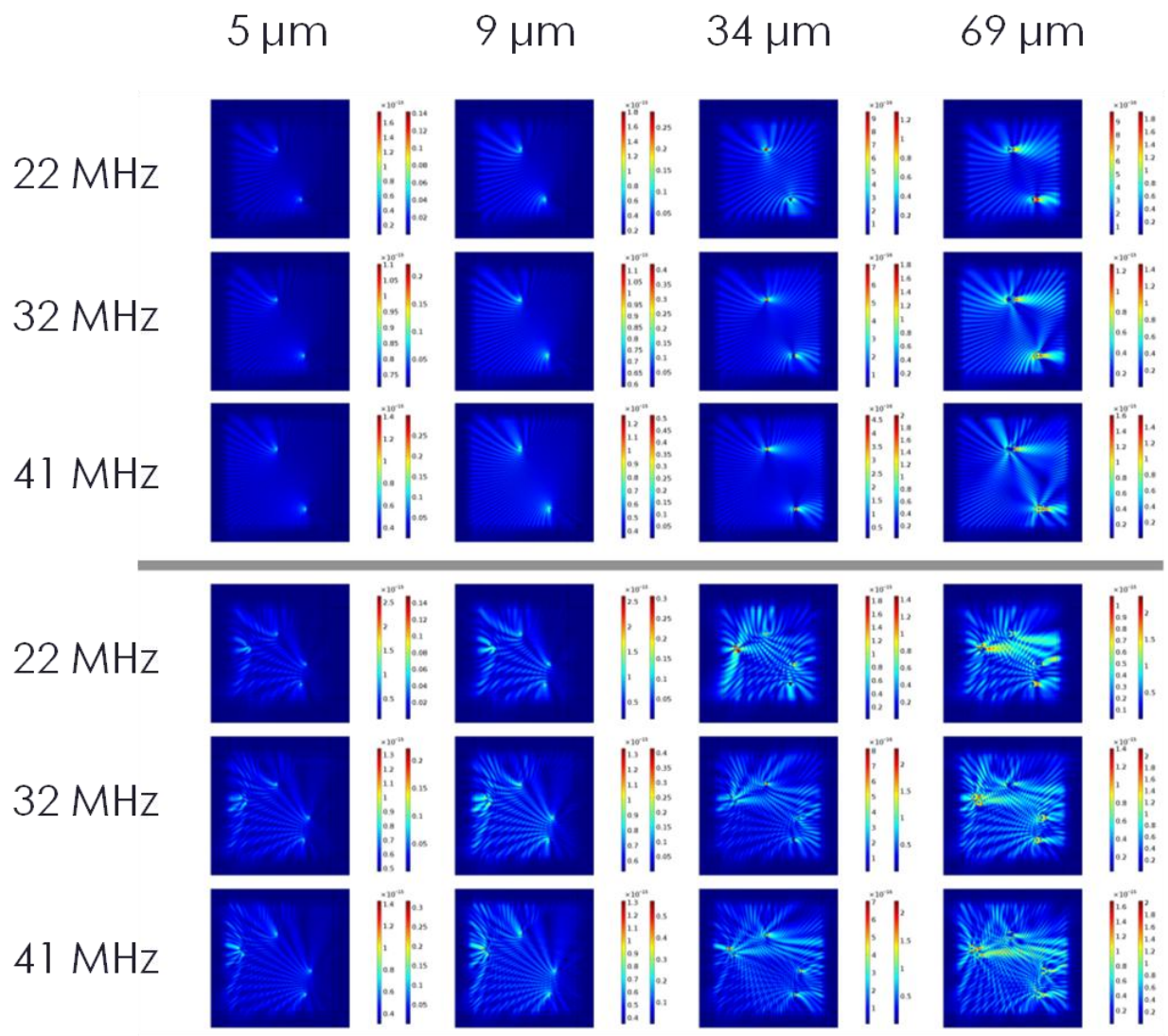

Figure 40. Magnitude of the scattered field for different scatterer diameters for the two and five bead configurations.

5.4.1 Experiment and simulation comparison

Simulated peak densities were calculated for each scatterer geometry as well as for each scatterer diameter. The peak density values were averaged for each diameter and configuration over the four trials. The peak densities for the experiment and model can be found in Figure 41(a) and (b) respectively. Upon inspecting the graphs we see the overall trend in which peak density tends to rise for increasing scatterer size as well as increasing numbers of scatterers.

Additionally, in the experimental data we see a certain threshold value for peak density. If there is not enough scattering, the peak density remains around the value of four. Once the scattering exceeds that threshold we start seeing more peaks. This is likely due to the fact that the glass beads are embedded in the gelatin medium, and the medium overshadows the small scattering contributions of these scatterers. We note that our model considers a fluid medium. This means the model captures the entire response of the scattered pressure and incorporates even minimal scattering contributions. Ultimately, by comparing the model with the experiment, they both show the same overall trend we are interested in.

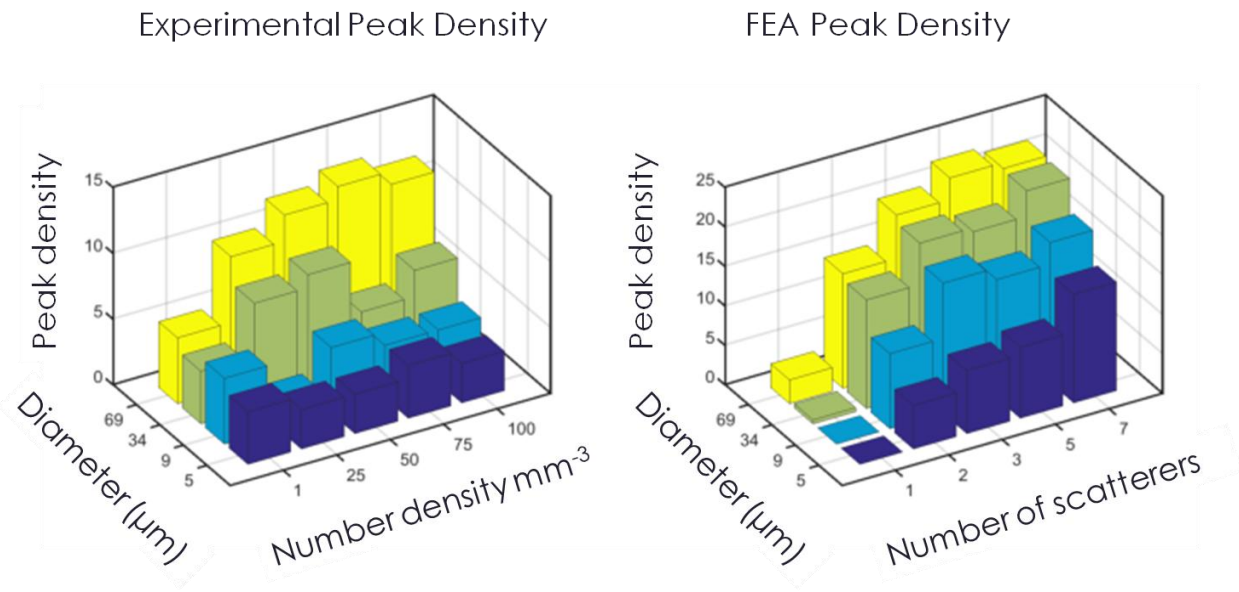

Figure 41. Bar graphs showing the measured peak densities for the experiment and finite element model.

In both the model and experiment it appears that the peak density may be beginning to level off at large scatter size and high numbers of scatterers and there seem to be local variations in the overarching trend. In order to explore this further, the simulations were repeated using both larger scatterers and higher numbers. These expanded simulations included scatterer diameters of 100 and 150 µm and also considered scatterer numbers of 10, 15, 20 and 25. The resulting simulated peak density values are shown in Figure 42.

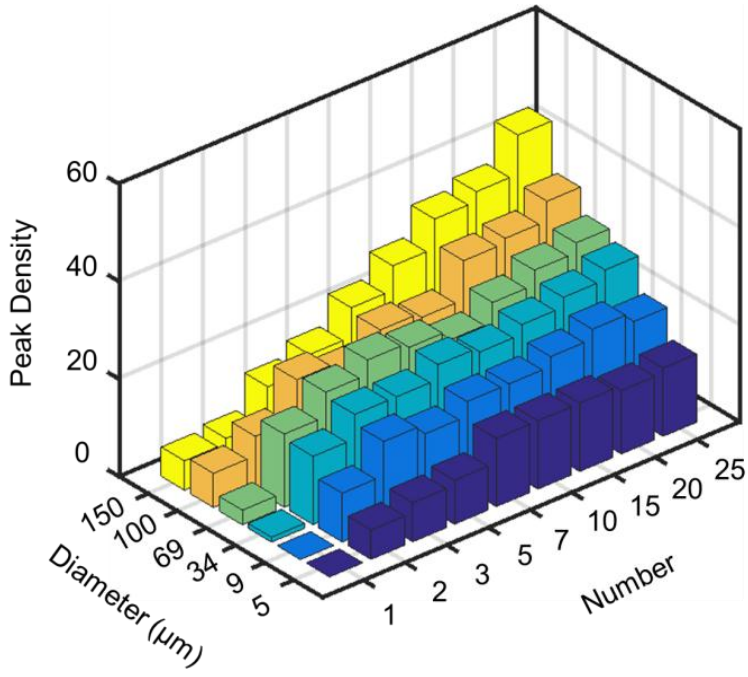

Figure 42. Peak densities for the expanded model including larger and additional scatterers added to the simulation domain.

From the additional simulations we see that the same general trend noted earlier still holds—peak density tends to increase with scatterer size and number. We do note however that this is not necessarily absolute and in a few cases we may see a small dip in the trend. In addition, it is seen at the edges of the data the trend begins to decay. The peak density does not continue to increase with diameter at low numbers of scatterers and the peak density flattens out for the smallest scatterer at high numbers.

Figure 43 gives a more in depth view of how the peak density varies with the scatterer size and number. Figure 43(a) shows the peak density as a function of scatterer number for each different diameter. At low numbers we see that the peak density is more variable and less apt at distinguishing among particle sizes. As the number of scatterers increase, the peak density values separate, and the size of the scatterers are identified in the correct order. The peak density is

plotted as a function of scatterer size in Figure 43(b). From this graph it is seen that low numbers of scatterers, regardless of size, give much lower peak densities. Additionally, very high numbers tend to give larger peak densities for each size. Lastly, as the size of the scatterers increases, the peak densities eventually separate according to the number of scatterers present.

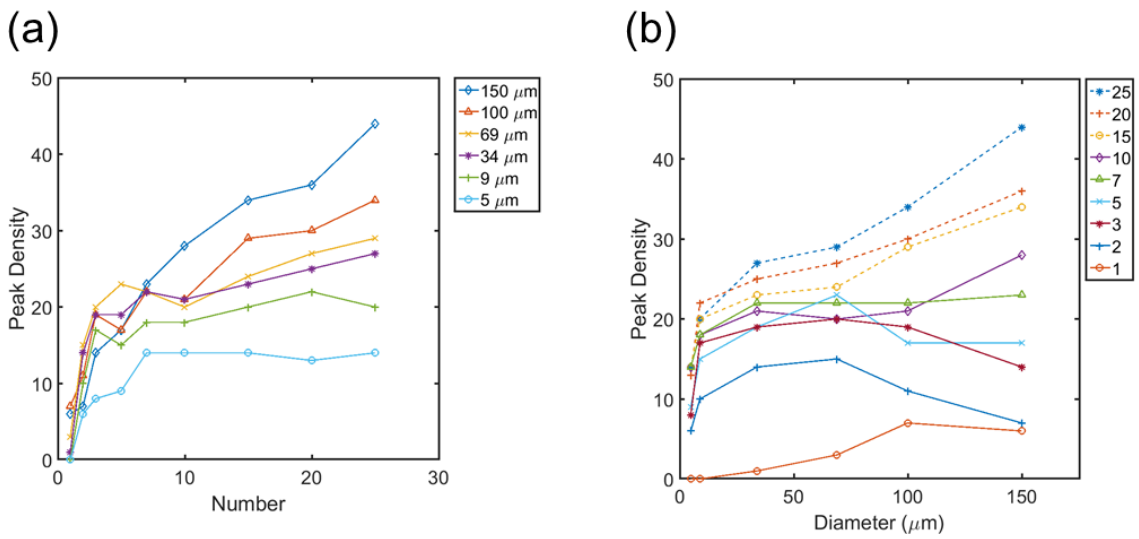

Figure 43. Simulated peak density values as a function of scatterer number (a) and scatterer size (b).

5.4.2 Comparison of peak density with traditional methods

In order to demonstrate the purposefulness of peak density measurement, we also compare the experimental peak density values gathered for the phantoms with more conventional through-transmission, amplitude-based measurements. The amplitude measurements were found by finding the maximum of the envelope of the pulse received through the phantom. The envelope was obtained through the Hilbert transform of the waveform. As with the previous peak density measurements, the amplitudes were determined for each individual scan line and then averaged. Figure 44 gives a side-by-side comparison of these results. From Figure 44(b) it is apparent that

the amplitude measurements do not really discriminate among the different phantoms, whereas peak density shows a much more drastic difference.

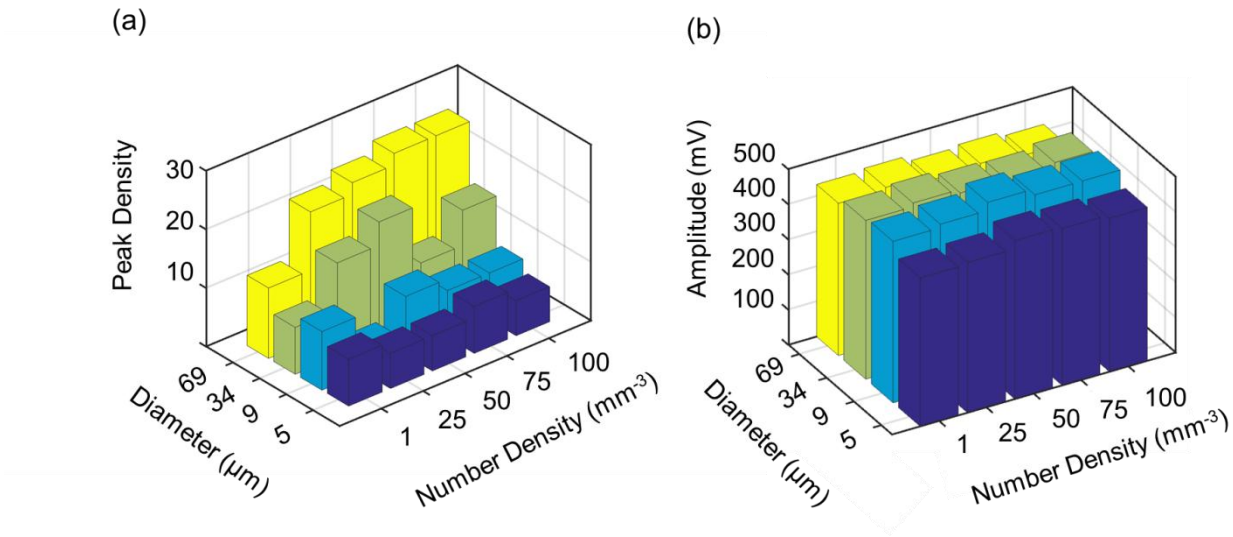

Figure 44. Comparison of measurements taken for experimental phantoms: peak density (a) and pulse amplitude (b).

5.4.3 Comparisons with scattering theory

Figure 45 shows this value for numbers and sizes of scatterers considered earlier. We see that these results suggest a similar general trend as shown by our model earlier. This implies that peak density, which is essentially a measure of the complexity present in the frequency spectrum, is influenced by the increase in the complexity of the scattered pressure field caused by increasing the total amount scattering present in the system. Obviously, at some point the number and size of scatterers becomes high enough that multiple scattering would become a factor. While this simple scattering representation may not incorporate multiple scattering, what it does show is that as multiple scattering becomes more likely, peak density increases.

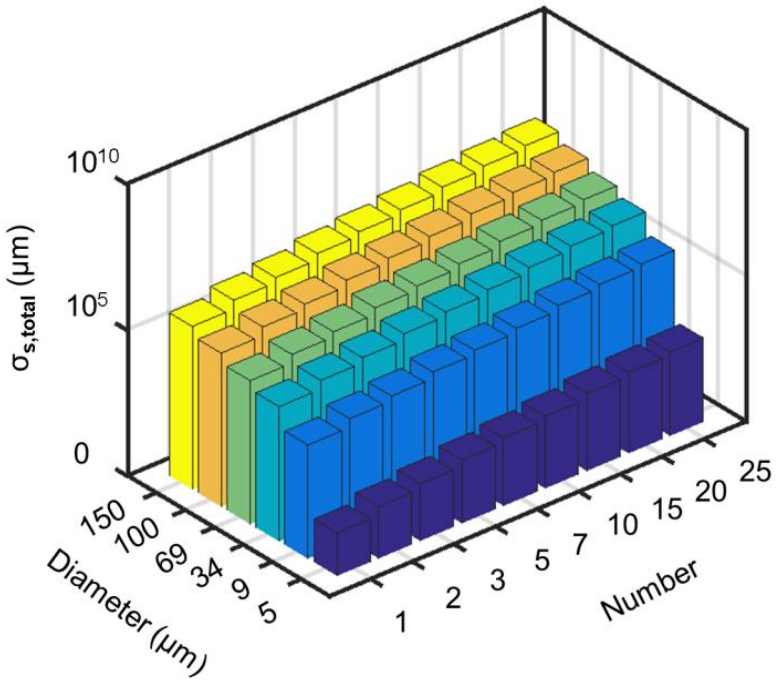

Figure 45. Calculation of the total scattering using analytical techniques. Note that z axis uses a logarithmic scale in order to show the full range of $\sigma_{s,total}$.

5.4.4 Application of peak density measurements for scatterers of different materials

To further examine the effect of the material properties of the scatterers on the total scattering within in the system as well as the peak density, we next present the results for another type of microsphere often used in experiment— polystyrene. The simulations were rerun in the same manner as done previously using the same sizes, numbers and configurations. The material properties used can be found in Table 4.

Table 4. Input parameters for polystyrene scatterers [38].

Model parameters fluid	Input value
Density ρ_c	1 g/cm^3
Sound speed c_c	1540 m/s
Model parameters solid	**Input value**
Density ρ_s	1.06 g/cm^3
Poisson ratio ν	0.35
Young's Modulus E_Y	5.85 GPa
Sound speed c_s	2350 m/s

We expect that the difference in the material properties of polystyrene should give rise to different amounts of total scattering and in turn different values of peak density. Figure 46 plots the peak density and $\sigma_{s,total}$ as a function of number for each different diameter. From these results we observe that glass scatterers only have higher amounts of scattering for the 5 and 9 μm cases. Incidentally, we also notice these are the only two times in which the peak density for glass is consistently greater than that of polystyrene. For the 34 μm scatterer, $\sigma_{s,total}$ for both materials begins to converge along with the peak density. For the next two sizes, it is seen that the peak density for both materials are extremely similar and does not follow the trend of $\sigma_{s,total}$. For the largest scatterer, where the scattering for the polystyrene is the highest, it is seen that the peak density is well above that of the glass. Ultimately, these results suggest that peak density may discern among scatterers based upon the size, number and material. It is also observed that total amount of scattering in the systems affects the resulting peak density values.

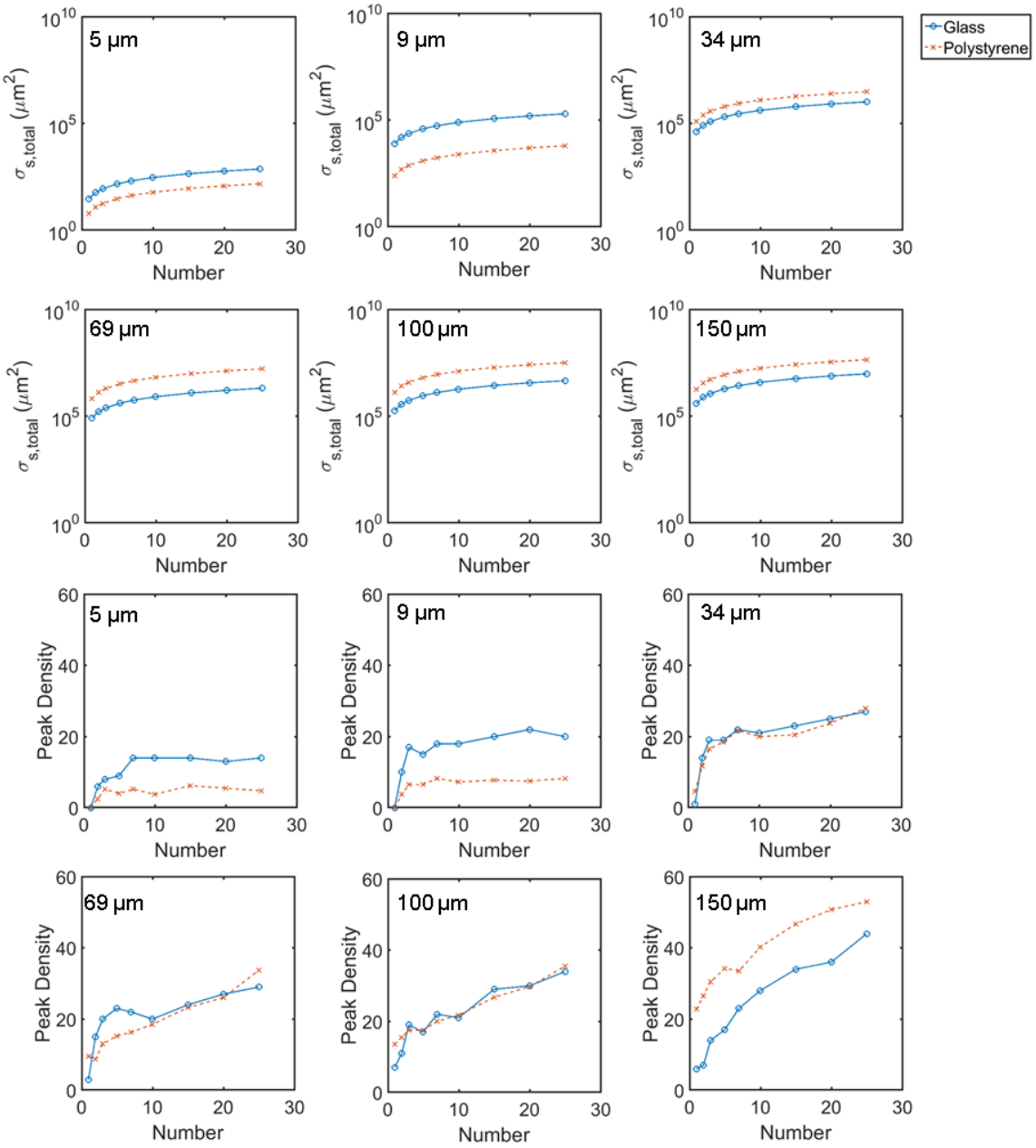

Figure 46. Comparison of $\sigma_{s,total}$ and peak density for glass and polystyrene scatterers. Note the logarithmic scale for $\sigma_{s,total}$.

5.5. Conclusion

The work presented here investigated the response of peak density to varied microstructure within tissue-mimicking phantoms. Experiments showed that peak density was most receptive to larger scatterer sizes and high number densities. Finite element simulations were also carried out and showed comparable trends to the experiment. To gain a deeper understanding of the peak density measurement, the simulations were extended to include additional scatterer sizes and numbers. These expanded simulations reinforced the trend noted earlier and showed that the peak density is capable of differentiating glass scatterers of different sizes for a given number of scatterers. We then briefly discussed the total amount of scattering present in the system through analytical techniques. We calculated $\sigma_{s,total}$ for our different configurations and noted the correlation between scattering strength and peak density. The analytical and finite element methods were then applied to systems of scatterers with different material properties. The results were compared for the scatterers, showed that $\sigma_{s,total}$ was dependent upon the material properties and that peak density tended to vary in a similar manner. Lastly, we also demonstrated the actual usefulness of peak density by showing that peak density showed higher sensitivity to the microstructure of the phantoms than amplitude-based measurements.

Chapter 6.
Conclusion

6.1 Summary of work

Motivated by the need for improved detection methods for surgical margins, this work focused on methods for study and evaluation of soft materials. In particular, due to its inherent advantages, ultrasound was selected as the means of measurement. According to literature there exist several key gaps, and while ultrasonic evaluation may be a mature field, ample opportunity to contribute meaningful research still exists. Conventional ultrasound techniques are useful for probing internal structure and the detection of flaws. However, these measurements do not necessarily detail the material characteristics of the sample. Extensive work has been done to obtain calculable and more absolute results and has led to the field of Quantitative Ultrasound. While useful, this work typically considers only a handful of parameters and has seen limited clinical use. This dissertation aims to further this field by exploring additional parameters for QUS. Chapter 1 provided a review of traditional ultrasound methods. In addition, the techniques developed and currently used in QUS were discussed. From the literature review it was found that a parameter responsive to tissue microstructure, peak density, was worthy of additional study [73].

Chapter 2 described the relevant procedures to carry out ultrasound measurements. These techniques were used throughout the dissertation work. Over time, these methods were refined, and ultimately a fully functional ultrasound measuring system was developed.

Due to the limited studies using peak density, Chapter 3 examines this parameter by investigating it using controlled phantoms. The parameter was studied at multiple frequency scales and two dimensional mappings of the phantoms were evaluated. These early results suggested that peak density was at least as capable of imaging materials as standard through-transmission, amplitude-based flaw detection methods. This showed the viability of peak density as a measurement and demonstrated that it warranted further research.

With further analysis, it was found that the calculation of peak density was highly dependent on the specific signal processing procedure. To improve this measurement, the evaluation of the parameter was systematically studied with the application of several standard signal processing methods. Optimal acquisition settings were established to achieve reliable and reproducible measurements. This process was described in detail in Chapter 4.

To better understand the underlying physics affecting peak density, this dissertation sought to develop relationships between the parameter and microstructure. Chapter 5 first explored the total scattered pressure from elastic spheres. Experiments calculating peak density for tissue-mimicking phantoms with controlled microstructure were carried out. A finite element model was developed to compare with the experiment. The results of the experiments and model both demonstrate that peak density is most susceptible to larger scatterers and higher number densities. These peak densities were found to trend with the scattering cross-section.

6.2 Future recommendations

Owing to the youth of the peak density measurement and the relatively low amount of high-frequency ultrasound studies, there exists abundant opportunities for further research. In particular there are several specific areas to be explored:

6.2.1 Ultrasound studies of tissue

Unfortunately, the research done in this dissertation was not able to encompass the analysis of tissue samples as well. Testing real tissues would serve to advance the understanding of the high-frequency Quantitative ultrasound. This would allow for more detailed correlations to be made between peak density and tissue microstructure. In addition, new parameters and measurements may be identified that show a dependence on the structure. These further studies could serve to address the problem of margin identification as was original inspiration.

6.2.2 Studies of hard materials

The techniques described here could also be applied to systems other than soft materials. Experiments conducted with materials more commonly found in industry could prove fruitful for those applications. For example, the peak density calculation could be applied to industrial nondestructive testing for the purpose of crack detection in aerospace composites, delamination in composites or electronic packaging as well as structural analysis.

6.2.3 Higher frequency studies

In this work, it was found that peak density was most sensitive to scatterers with a high ka value. This implies that with increasing frequencies the results should become more interesting. It is also possible that at higher frequency regimes new correlations may be identified. With transducer technology improving, this should be more practical.

6.2.4 Expanded modeling of high-frequency scattering

The simulations presented here do help relate peak density to the presence of multiple scattering. However, while the model suggests the underlying physics, it is not necessarily predictive largely due to the two dimensional configurations. At high frequencies, simulations of multiple scattering become computationally expensive and have problems with convergence. For example, the mesh element density for a finite element model needs to be fine enough to resolve the waves. Since the wavelength is inversely proportional to the frequency, at high frequencies the necessary mesh becomes extremely fine.

We also note that the model used in this work considers the scatterers to be immersed in a fluid. This is a commonly used assumption based on the extremely high water content of tissue, and it significantly reduces the complexity of the model. Since fluids do not support shear waves, shear wave propagation and other wave modes need not be considered, and the number of calculations needed are decreased. We recognize that by using fluid wave propagation the simulations do not take into account any resonances or relaxation effects that occur for a solid medium. This topic of multiple acoustic scattering due to objects in an elastic or viscoelastic medium is an intricate subject and an entire dissertation could be devoted to the subject. Much research is being done even at the time of this work to solve this problem [106,107].

As computing power continues to follow Moore's Law, three dimensional models of the acoustic scattering considering elastic and viscoelastic effects will become more practical and a full predictive model may be possible.

References

1. S. Litière, G. Werutsky, I.S. Fentiman, E. Rutgers, Breast conserving therapy versus mastectomy for stage I–II breast cancer: 20 year follow-up of the EORTC 10801 phase 3 randomised trial, The Lancet Oncology, 13 (2012) 412-419.
2. R. Siegel, J. Ma, Z. Zou, A. Jemal, Cancer statistics, 2014. CA Cancer J. Clin., 64 (2014) 9-29.
3. R.G. Pleijhuis, M. Graafland, J. de Vries, J. Bart, Obtaining adequate surgical margins in breast-conserving therapy for patients with early-stage breast cancer: current modalities and future directions. Ann. Surg. Oncol., 16 (2009) 2717-2730.
4. L. Jacobs, Positive margins: the challenge continues for breast surgeons. Ann. Surg. Oncol. 15 (2008) 1271–1272.
5. O. Olsha, D. Shemesh, M. Carmon, O. Sibirsky, R. Abu Dalo, L. Rivkin, I. Ashkenazi, Resection margins in ultrasound-guided breast-conserving surgery. Ann. Surg. Oncol., 18 (2011) 447–452.
6. S.E. Singletary, Surgical margins in patients with early-stage breast cancer treated with breast conservation therapy, Am. J. Surg., 184 (2002) 383–393.
7. A.L. Russo, N.D. Arvold, A. Niemierko, N. Wong , J.S. Wong, J.R. Bellon, R.S. Punglia, M. Golshan, S.L. Troyan, J.E. Brock, Margin status and the risk of local recurrence in patients with early-stage breast cancer treated with breast-conserving therapy,Breast Cancer Res. Treat., 140 (2013) 353–361.
8. S. Kennedy, J. Geradts, T. Bydlon, J. Brown, J. Gallagher, M. Junker, W. Barry, N. Ramanujam, L. Wilke, Optical breast cancer margin assessment: an observational study

of the effects of tissue heterogeneity on optical contrast, Breast Cancer Res., 12 (2010) R91.

9. K.E. Pengel, C.E.Loo, H.J. Teertstra, S.H. Muller, J. Wesseling, J.L. Peterse, H. Bartelink, E.J. Rutgers, K.G Gilhuijs, The impact of preoperative MRI on breast-conserving surgery of invasive cancer: a comparative cohort study. Breast Cancer Res. Treat., 116 (2009) 161–169.
10. D.R. Faverly, J.H. Hendriks, R. Holland, Breast carcinomas of limited extent: frequency, radiologic-pathologic characteristics, and surgical margin requirements, Cancer, 91 (2001) 647–659.
11. T.P. Olson, J. Harter, A. Muñoz, D.M. Mahvi, T. Breslin, Frozen section analysis for intraoperative margin assessment during breast-conserving surgery results in low rates of re-excision and local recurrence, Ann. Surg. Oncol., 14 (2007) 2953–2960.
12. M. Thill, K. Baumann, J. Abramoff, Intraoperative assessment of margins in breast conservative surgery—still in use? J. Surg. Oncol., 110 (2014) 15-20.
13. T. Karni, I. Pappo, J. Sandbank, O. Lavon, V. Kent, R. Spector, S. Morgenstern, S. Lelcuk, A device for real-time, intraoperative margin assessment in breast-conservation surgery, Am. J. Surg . 194 (2007) 467–473.
14. T. M. Allweis, Z. Kaufman, S. Lelcuk, I. Pappo, T. Karni, S. Schneebaum, R. Spector, A. Schindel, D. Hershko, M. Zilberman, A prospective, randomized, controlled, multicenter study of a real-time, intraoperative probe for positive margin detection in breast-conserving surgery, Am. J. Surg. 196 (2008) 483–489.

15. A.S. Haka, Z. Volynskaya, J.A. Gardecki, J. Nazemi, J. Lyons, D. Hicks, M. Fitzmaurice, R.R. Dasari, J.P. Crowe, M.S. Feld, In vivo margin assessment during partial mastectomy breast surgery using Raman spectroscopy, Cancer Res., 6 (2006) 3317–3322.
16. F. Nguyen, A. Zysk, E. Chaney, J. Kotynek, U. Oliphant, F. Bellafiore, K. Rowland, P. Johnson, S. Boppart, Intraoperative Evaluation of Breast Tumor Margins with Optical Coherence Tomography, Cancer Res., 69 (2009) 8790–8796.
17. S. Pani, E. Cook, J. Horrocks, J. Jones, R. Speller, Characterization of breast tissue using energy-dispersive X-ray diffraction computed tomography, Appl. Radiat. Isot., 68 (2010) 1980-1987.
18. P. J. Shull, Nondestructive Evaluation Theory, Techniques, and Applications, Marcel Dekker, New York, 2002.
19. J. Krautkrämer, H. Krautkrämer, Ultrasonic Testing of Materials, fourth ed., Springer-Verlag, Berlin, 1990.
20. Nishimura RA, Edwards WD, Warnes CA. Intravascular ultrasound imaging: in vitro validation and pathologic correlation. J Am Coll Cardiol. 1990 Jul;16(1):145-154.
21. Dimagno EP, Regan PT, Clain JE, James EM, and Buxton JL. Human endoscopic ultrasonography. Gastroenterology, 83(4):824–829, 1982.
22. G. Ter Haar, Ultrasonic imaging: safety considerations, Interface Focus. 1 (2011) 686-697.
23. T.L. Szabo, Diagnostic Ultrasound Imaging: Inside Out, Elsevier, Boston, 2004.
24. R.S. Gilmore, K.C. Tam, J.D. Young, D.R. Howard, Acoustic microscopy from 10-100 MHz for industrial applications, Phil. Trans. R. Soc. Lond. 320 (1986) 215-235.

25. G. Kossoff, E. Fry, J. Jellins, Average velocity of ultrasound in the human female breast, J. Acoust. Soc. Am. 53 (1973) 1730-1736.

26. C. Li, L. Huang, N. Duric, H. Zhang, C. Rowe, An improved automatic time-of-flight picker for medical ultrasound tomography, Ultrasonics. 49 (2009) 61–72.

27. J. Wiskin, D. Borup, S. Johnson, M. Berggren, Non-linear inverse scattering: high resolution quantitative breast tissue tomography. The Journal of the Acoustical Society of America. 131 (2012) 3802–13.

28. J.R. Jago, T.A. Whittingham, Experimental studies in transmission ultrasound computed tomography, Physics in Medicine and Biology. 11 (1991) 1515-1527.

29. J.F. Greenleaf, R.C. Bahn, Clinical imaging with transmissive ultrasonic computerized tomography, Biomedical Engineering. 28 (1981)177-185.

30. M.A. Rice, K.R. Waters, K.S. Anseth, Ultrasound monitoring of cartilaginous matrix evolution in degradable PEG hydrogels, Acta Biomateriala 5 (2009) 152-161.

31. K.A. Wear, A.P. Stuber, J.C. Reynolds, Relationships of ultrasonic backscatter with ultrasonic attenuation, sound speed and bone mineral density in human calcaneus, Ultrasound in Medicine & Biology. 26 (2000) 1311–1316.

32. F.T. D'Astous, F.S. Foster, Frequency dependence of ultrasound attenuation and backscatter in breast tissue, Ultrasound Med. Biol., 12 (1986) 795-808.

33. Y. Labyed, T.A. Bigelow, A theoretical comparison of attenuation from backscattered ultrasound echoes, J. Acoust. Soc. Am. 129 (2011) 2316-2324.

34. F.L. Lizzi, M. Greenebaum, E.J. Feleppa, M. Elbaum, Theoretical framework for spectrum analysis in ultrasonic tissue characterization, J. Acoust. Soc. Am. 73 (1983) 1366-1373.

35. F.L. Lizzi, Ostromogilsky, E.J. Feleppa, M.C. Rorke, M.M. Yaremko, Relationship of Ultrasonic Spectral Parameters to Features of Tissue Microstructure, IEEE Transactions on Ultrasonics, Ferroelectrics and Frequency Control. 34 (1987) 319–329.

36. E.J. Feleppa, F.L. Lizzi, D.J. Coleman, Diagnostic spectrum analysis in ophthalmology: a physical perspective, Ultrasound in Med. & Biol. 12 (1986) 623-631.

37. H. Tadayyon, A. Sadeghi-Naini, L. Wirtzfeld, F. Wright, G. Czarnota, Quantitative ultrasound characterization of locally advanced breast cancer by estimation of its scatterer properties., Medical Physics. 41 (2014) 012903.

38. M.F. Insana, R.F. Wagner, D.G. Brown, Describing small-scale structure in random media using pulse-echo ultrasound, J. Acoust. Soc. Am. 87 (1990) 179-192.

39. S. Brand, B. Solanki , D. Foster, G. Czarnota, M. Kolios, Monitoring of cell death in epithelial cells using high frequency ultrasound spectroscopy, Ultrasound Med. Biol., 35 (2009) 482–93.

40. J.C. Bamber, C.R. Hill, J.A. King, F. Dunn, Ultrasonic propagation through fixed and unfixed tissues, Ultrasound Med. Biol., 5 (1979) 159-165.

41. D. Nicholas, Evaluation of backscattering coefficients for excised human tissues, Results, Interpretation, and associated measurements, Ultrasound Med Biol, 8 (1982) 17-28.

42. M. Ueda, Y. Ozawa, Spectral analysis of echoes for backscattering coefficient measurements, J. Aousct. Soc. Am., 77 (1985) 38-47.

43. L.X. Yao, J.A. Zagzebski, E.L. Madsen, Backscatter coefficient measurements using a reference phantom to extract depth-dependent instrumentation factors, Ultrason. Imag., 12 (1990) 58-70.

44. X. Chen, D. Phillips, K.Q. Schwarz, J.G. Mottley, K.J. Parker, The measurement of backscatter coefficient from a broadband pulse-echo system: A new formation, IEEE Trans. Ultrason. Ferroelectr. Control, 44 (1997) 515-525.

45. M. O'Donnell, J.G. Miller, Quantitative broadband ultrasonic backscatter: An approach to nondestructive evaluation in acoustically inhomogeneous materials, J. Appl. Phys.52 (1981) 1056–1065.

46. T.A. Bigelow, W.D. O'Brien, Scatterer size estimation in pulse-echo ultrasound using focused sources: Theoretical approximation and simulation analysis, J. Acoust. Soc. Am., 116(2004) 578-593.

47. M.L. Oelze, J.F. Zachary, W.D. O'Brien Jr., Characterization of tissue microstructure using ultrasonic backscatter: Theory and technique for optimization using a Gaussian form factor, J. Acoust. Soc. Am. 112 (2002) 1202-1211.

48. M. Oelze, J. Zachary, Examination of cancer in mouse models using high-frequency quantitative ultrasound, Ultrasound Med. Biol., 32 (2006) 1639-1648.

49. A.V. Oppenheim, R.W. Schafer, From frequency to quefrency: A history of the cepstrum, IEEE Signal Processing Magazine, 21 (2004) 95-106.

50. L. Landini, L. Verrazzani, Spectral characterization of tissue microstructure by ultrasound: a stochastic approach, IEEE T. Ultrason. Ferr., 37 (1990) 448–456.

51. Y. Bige, Z. Hanfeng, W. Rong, Analysis of microstructural alterations of normal and pathological breast tissue in vivo using the AR cepstrum, Ultrasonics, 440(2006) 211-215.

52. L.L. Fellingham, F.G. Sommer, Ultrasonic characterization of tissue structure in the in vivo human liver and spleen, IEEE Transactions on Sonics and Ultrasonics, 3 (1984) 418-428.

53. T. Varghese, K.D. Donohue, Mean-scatterer spacing estimates with spectral correlation, J. Acoust. Soc. Am., 96 (1994) 3504-3515.

54. X. Tang, U. Abeyratne, Wavelet transforms in estimating scatterer spacing from ultrasound echoes, Ultrasonics 38 (2000) 688-692.

55. T.E. Doyle, J.B. Goodrich, B.J. Ambrose, H. Patel, S. Kwon, L.H. Pearson, Ultrasonic differentiation of normal versus malignant breast epithelial cells in monolayer cultures, J. Acoust. Soc. Am., 128 (2010) EL229-235.

56. Y. Guo, H.D. Cheng, J.i Tian, Y. Zhang, A novel approach to speckle reduction in ultrasound imaging, Ultrason.in Med. and, Biol., 35 (2009) 628–640

57. W.C. Yeh, S.W. Huang, P.C. Li, Liver fibrosis grade classification with B-mode imaging, Ultrason. Med. Biol. 29 (2003) 1229-1235.

58. D.R. Chen, R.F. Chang, W.J. Kuo, M.C. Chen, Y.L. Huang, Diagnosis of breast tumors with sonographic texture analysis using wavelet transform and neural networks, Ultrason. Med. Biol., 28 (2002) 1301-1301.

59. M. Levy, H.E. Bass, R.R. Stern, L. Furr, Handbook of elastic properties of solids, liquids, and gases, Vol. III, Academic Press, San Diego, CA, 2001.

60. J. Ophir, I. Cespedes, B. Garra, H. Ponnekanti, Y. Huang, N. Maklad, Elastography: ultrasonics imaging of tissue strain and elastic modulus in vivo, Eur. J. Ultrasound. 3 (1996) 49-70.

61. J. Ophir, S.K. Alam, B.S. Garra, F. Kallel, Elastography: imaging the elastic properties of soft tissues with ultrasound, J. Med. Ultrasonics, 29 (2002) 155-171.

62. K. Manickam, R.R. Machireddy, S. Seshadri, Study of ultrasound stiffness imaging methods using tissue mimicking phantoms, Ultrasonics, 54 (2014) 621-631.

63. E.J. Chen, J. Novakofski, W.K. Jenkins, Young's modulus measurements of soft tissues with application to elasticity imaging, IEEE Trans. Ultrason. Ferroelectr.Freq. Con., 43 (1996) 191-195.

64. C.J. Pavlin, et al. Clinical use of ultrasound biomicroscopy. Ophthalmology 98 (1991) 287–295.

65. D.Z. Reinstein, S Srivannaboon, M. Gobbe. Epithelial thickness profile changes induced by myopic LASIK as measured by Artemis very high-frequency digital ultrasound. Journal of Refractive Surgery 25 (2009) 444-450.

66. C. Passmann, H. Ermert. A 100-MHz ultrasound imaging system for dermatologic and ophthalmologic diagnostics. Ultrasonics 43 (1996) 545-552.

67. D. Turnbull, et al. A 40–100 MHz B-scan ultrasound backscatter microscope for skin imaging. Ultrasound Med. Biol. 21 (1995) 7988.

68. P. Patwari et al. Assessment of coronary plaque with optical coherence tomography and high-frequency ultrasound. Am. J. Cardiol. 85 (2000) 641-644.

69. B. Potkin, et al. Coronary artery imaging with intravascular high-frequency ultrasound. Circulation 81 (1990)1575-1585.

70. R.W. Martin, F.E. Silverstein, M.B. Kimmey, A 20-MHz ultrasound system for imaging the intestinal wall, Ultrasound Med. Biol., 15 (1989) 273-280.

71. A. Briggs, O. Kolosov. Acoustic microscopy. OUP Oxford, 2009.

72. R.A. Lemons, C.F. Quate. Acoustic microscope- scanning version. Applied Physics Letters 24 (1974).

73. L.W. Kessler, Acoustic microscopy, ASM Handbook. 17 (1989): 465-482.

74. Sonoscan, Inc. http://www.sonoscan.com/

75. T.M. Moore, C-mode acoustic microscopy applied to integrated circuit package inspection, Solid-state electronics 35 (1992) 411-421.

76. J. Bereiter-Hahn, L.Karl, H. Lüers, M. Vöth, Mechanical basis of cell shape: investigations with the scanning acoustic microscope, Biochemistry and Cell Biology, 73 (1995) 337-348.

77. J. A. Hildebrand, D.Rugar, R. N. Johnston, C. F. Quate, Acoustic microscopy of living cells, Proceeding of the National Academy of Sciences, 78 (1981) 1656-1660.

78. T.E. Doyle, R.E. Factor, C.L. Ellefson, K.M. Sorensen, B.J. Ambrose, J.B. Goodrich, et al., High-frequency ultrasound for intraoperative margin assessments in breast conservation surgery: a feasibility study., BMC Cancer. 11 (2011) 444.

79. S. Hirsekorn, P.W. van Andel, U. Netzelmann, Ultrasonic methods to detect and evaluate damage in steel, Nondestruct. Test. Eva. 15 (1998) 373-393.

80. H.J. Yim, H. Kwak, J.H. Kim, Wave attenuation measurement technique for nondestructive evaluation of concrete, Nondestruct. Test. and Eva. 27 (2012) 81-94.

81. I.M. Daniel, S.C. Wooh, I. Komsky, Quantitative porosity characterization of composite materials by means of ultrasonic attenuation measurements, J. Nondestruct. Eva., 11 (1992) 1-8.

82. F.C. Beall, Overview of the use of ultrasonic technologies in research on wood properties, Wood Sci. Technol. 36 (2002) 197-212.

83. R.B. Ashman, S.C. Cowin, W.C. Van Buskirk, J.C. Rice, A continuous wave technique for the measurement of the elastic poroperties of cortical bone, J. Biomechanics, 17 (1984) 349-361.

84. Z. Su, L. Ye, Y. Lu, Guided Lamb waves for identification of damage in composite structures: A review, J. Sound Vibration, 295 (2006) 753-780.

85. J.L. Rose, A baseline and vision of ultrasonic guided wave inspection potential, J. Pressure Vessel Technology, 124 (2002) 273-282.

86. M.H.S. Siqueira, C.E.N. Gatt, R.R. da Silva, J.M.A. Rebello, The use of ultrasonic guided waves and wavelets analysis in pipe inspection, Ultrasonics, *(*2004) 785-797

87. C.A. Bennett, Principles of Physical Optics, John Wiley & Sons, Hoboken, NJ, 2007.

88. J.Strutt, On the light from the sky, its polarization and colour, *Philosophical Magazine*, 41 (1871) 107-120, 274-279.

89. P.M. Morse, K.U. Ungard, Theoretical Acoustics, Princeton University Press, Princeton, NJ, 1968.

90. F.P. Mechel, Formulas of Acoustics, Springer-Verlag, Berlin, Germany, 2002.

91. M.J. Crocker, Handbook of Acoustics, John Wiley and Sons, New York, NY, 1998.

92. J.J. Faran, Sound Scattering by solid cylinders and spheres, Journal of the Acoustical Society of America, 23 (1951) 405-418.

93. R. Hicking, Analysis of echoes from a solid elastic sphere in water, Journal of the Acoustical Society of America, 34 (1962) 1582-1592.

94. L.A. Frizzell LA, E.L. Carstensen, Shear properties of mammalian tissues at low megahertz frequencies, J. Acoust. Soc. Am., 60 (1976) 1409–1411.

95. G. Arfken, H.J. Weber, Mathematical Methods for Physicists, sixth ed., Elsevier, Burlington, MA, 2005.

96. R.N. Bracewell, The Fourier Transform and its Applications, third ed., McGraw-Hill Book Company, New York, 1999.

97. J.W. Cooley, J.W. Tukey, An algorithm for the machine calculation of complex Fourier series, Mathematics of Computation. 19 (1965) 297-301.

98. M. Castaings, P. Cawley, R. Farlow, G. Hayward. Single sided inspection of composite materials using air coupled ultrasound, Journal of Nondestructive Evaluation, 17 (1998) 37-45.

99. D. W. Schindel, D. A. Hutchins, Through-thickness characterization of solids by wideband air-coupled ultrasound, Ultrasonics, 33 (1995) 11-17.

100. R. Stoessel, N. Krohn, K. Pfleiderer, G. Busse, Air-coupled ultrasound inspection of various materials, Ultrasonics, 40 (2002) 159-163.

101. Marple, S. L. "Computing the Discrete-Time Analytic Signal via FFT." IEEE Transactions on Signal Processing. Vol. 47, 1999, pp. 2600–2603.

102. 12 Things to Consider when choosing an oscilloscope. #48X-28633-0 . Tektronix, Inc. 2012.

103. R. Bude, R. Adler, An easily made, low-cost, tissue-like ultrasound phantom material, J. Clin. Ultrasound. 23 (1995) 271-273.

104. J. Stromer, L. Ladani, Investigating ultrasonic imaging in the frequency domain for tissue characterization, Nondestruct. Test. and Eva.

105. A. Ishimaru, Wave Propagation and Scattering in Random Media, Volume 1, Academic Press, New York, 1978.

106. A. Taheri, F. Honarvar, Multiple scattering of an acoustic wave from a network of cylindrical rods encased in a solid viscoelastic medium, Ultrasonics, 64 (2016) 69-76.

107. S. Khazaie, R. Cottereau, D. Clouteau, Influence of the spatial correlation structure of an elastic random medium on its scattering properties, J. Sound Vibration, 370 (2016) 132-148.

Appendix A. Matlab code

A.1 Peak counting

```
function [peaks, val,bins] = peakcounter(Y)
%peakcounter counts the number of peaks present in a waveform
% finds peaks by finding the local extrema in a waveform by counting the
% number of times the first derivative crosses the x axis
% variables:
% peaks: number of peaks
% val: values of the peaks
% bins: locations of each peak

dy = diff(Y);%find 1st derivative
peaks = 0; %initial number of peaks to 0
bins=zeros(1,length(Y)); %initialize bins

for i=2:length(dy) %start at second point
   if(dy(i) * dy(i-1) < 0) %determine if it crosses x axis by seeing if the product is negative
            peaks(1)=peaks+1; %add to peak
           bins(i)=i; %record bin
           val(i)=Y(i); %record  val
   else %not a peak
      bins(i)=0; %record 0 in bin
      val(i)=0; %record 0 in val
   end
end

bins(bins==0)=[]; %remove zeros
val(val==0)=[]; %remove zeros
```

A.3 Fourier Transform

```
function [freq,Y] = myfft(t,y,dt)
%myfft: Finds the fft given time and amplitude data
%   myfft(t,y,dt)
%   INPUTS:
%   t time vector
%   y amplitude vector
%
%   OUTPUTS
%   freq frequency vector cut off at nyquist frequency
%   Y power spectrum of frequency cut off at nyquist frequency
```

```
if nargin == 2
    dt = t(2)-t(1); %if dt is not input, calculate dt this way
end

nfft = 2^nextpow2(length(y));   %finds number of pts for computing fft... power of two
improves calculation
Fs = 1/dt;  %sampling frequency
F = fft(y,nfft);    %finds fft of input waveform
Y = 2*abs(F)/length(y);  %power spectrum. factor of two is from normalization and we
want single sided spectrum
%freq = (0:nfft-1)/(nfft*dt);    %finds frequency bins

nyq = Fs/2; %nyquist frequency. max value measureable doing fft

%nyq_bin = find(freq >= nyq,1,'first');  %finds freq. bin which contain nyquist frequency

%freq = freq(1:nyq_bin); %resizes to only show data up to nyquist freq.
freq=Fs/2*linspace(0,1,nfft/2+1);
%Y = Y(1:nyq_bin);
Y=Y(1:nfft/2+1);

end
```

Appendix B. Arduino Programs

B.1 Arduino stepper motor control

```
int p1 = 8;
int p2 = 9;
int p3 = 10;
int p4 = 11;
int butFx = 7;
int butBx = 6;
int but_stateFx=0;
int but_stateBx=0;
int butLy = 5;
int butRy = 4;
int but_stateLy=0;
int but_stateRy=0;
int butUz = 3;
int butDz = 2;
int but_stateUz = 0;
int but_stateDz = 0;
int xen = A0;//motor enable pin x direction
int yen = A2;//motor enable pin y direction
int zen = A3;//motor enable pin z direction

void setup(){
  pinMode(13,OUTPUT);//test LED
  for(int i =1;i<5;i++){
  digitalWrite(13,HIGH);//test LED
```

```
  delay(500);
  digitalWrite(13,LOW);
  delay(500);}
  digitalWrite(13,HIGH);

  pinMode(p1,OUTPUT);
  pinMode(p2,OUTPUT);
  pinMode(p3,OUTPUT);
  pinMode(p4,OUTPUT);
  pinMode(xen,OUTPUT);
  pinMode(yen,OUTPUT);
  pinMode(zen,OUTPUT);
  pinMode(butFx,INPUT);
  digitalWrite(butFx,HIGH);//pull up resistors
  pinMode(butBx,INPUT);
  digitalWrite(butBx,HIGH);
  pinMode(butLy,INPUT);
  digitalWrite(butLy,HIGH);
  pinMode(butRy,INPUT);
  digitalWrite(butRy,HIGH);
  pinMode(butUz,INPUT);
  digitalWrite(butUz,HIGH);
  pinMode(butDz,INPUT);
  digitalWrite(butDz,HIGH);
}
void loop(){
  but_stateLy=digitalRead(butLy);
```

```
but_stateRy=digitalRead(butRy);
but_stateFx=digitalRead(butFx);
but_stateBx=digitalRead(butBx);
but_stateUz=digitalRead(butUz);
but_stateDz=digitalRead(butDz);
digitalWrite(xen,HIGH);
digitalWrite(yen,HIGH);
digitalWrite(zen,HIGH);
if(but_stateLy==LOW){
  digitalWrite(yen,LOW);//turn motor enable pin on by setting transistor to low
  step1();
  step2();
  step3();
  step4();
  delay(100);
  delay(500);
  digitalWrite(yen,HIGH);//turn motor enable pin off
}
if(but_stateRy==LOW){
  digitalWrite(yen,LOW);
  step3();
  step2();
  step1();
  step4();
  delay(100);
  delay(500);
  digitalWrite(yen,HIGH);
```

```
}
if(but_stateFx==LOW){
  digitalWrite(xen,LOW);//turn motor enable pin on
  step1();
  step2();
  step3();
  step4();
  stopmotor();
  delay(100);
  digitalWrite(xen,HIGH);//turn motor enable pin off
}
if(but_stateBx==LOW){
  digitalWrite(xen,LOW);
  step3();
  step2();
  step1();
  step4();
  stopmotor();
  delay(100);
  digitalWrite(xen,HIGH);
}
if(but_stateUz==LOW){
  digitalWrite(zen,LOW);//turn motor enable pin on
  step1();
  step2();
  step3();
  step4();
```

```
    delay(600);
    digitalWrite(zen,HIGH);//turn motor enable pin off
   }
   if(but_stateDz==LOW){
    digitalWrite(zen,LOW);
    step3();
    step2();
    step1();
    step4();
    delay(600);
    digitalWrite(zen,HIGH);
   }
}

void step1(){
  digitalWrite(p1,HIGH);
  digitalWrite(p2,LOW);
  digitalWrite(p3,LOW);
  digitalWrite(p4,HIGH);
  delay(25);
}
void step2(){
  digitalWrite(p1,HIGH);
  digitalWrite(p2,LOW);
  digitalWrite(p3,HIGH);
  digitalWrite(p4,LOW);
  delay(25);
```

```
}
void step3(){
  digitalWrite(p1,LOW);
  digitalWrite(p2,HIGH);
  digitalWrite(p3,HIGH);
  digitalWrite(p4,LOW);
  delay(25);
}
void step4(){
  digitalWrite(p1,LOW);
  digitalWrite(p2,HIGH);
  digitalWrite(p3,LOW);
  digitalWrite(p4,HIGH);
  delay(25);
}
void stopmotor(){
  digitalWrite(p1,LOW);
  digitalWrite(p2,LOW);
  digitalWrite(p3,LOW);
  digitalWrite(p4,LOW);
}
```